27740

NATIONAL LIBRARY
OTTAWA

CANADA

BIBLIOTHÈQUE NATIONALE
OTTAWA

NAME OF AUTHOR....PAUL A. SPENCER.....

TITLE OF THESIS....^{23}Na....QUADRUPOLE...RELAXATION
MEASUREMENTS...BY...COMPUTER...CONTROLLED
NUCLEAR...MAGNETIC...DOUBLE...RESONANCE
SPECTROMETER.

UNIVERSITY.....ALBERTA.....

DEGREE FOR WHICH THESIS WAS PRESENTED....Ph.D.....

YEAR THIS DEGREE GRANTED.....1976.....

Permission is hereby granted to THE NATIONAL LIBRARY OF CANADA to microfilm this thesis and to lend or sell copies of the film.

The author reserves other publication rights, and neither the thesis nor extensive extracts from it may be printed or otherwise reproduced without the author's written permission.

(Signed).....P. S. Spencer.....

PERMANENT ADDRESS:

#5 10910 - 84 Ave.
EDMONTON, ALTA.
T6G 0V4

DATED..27 April.....19 76

NL-91 (10-68)

INFORMATION TO USERS

THIS DISSERTATION HAS BEEN
MICROFILMED EXACTLY AS RECEIVED

This copy was produced from a microfiche copy of the original document. The quality of the copy is heavily dependent upon the quality of the original thesis submitted for microfilming. Every effort has been made to ensure the highest quality of reproduction possible.

PLEASE NOTE: Some pages may have indistinct print. Filmed as received.

Canadian Theses Division
Cataloguing Branch
National Library of Canada
Ottawa, Canada K1A 0N4

AVIS AUX USAGERS

LA THESE A ETE MICROFILMEE
TELLE QUE NOUS L'AVONS RECUE

Cette copie a été faite à partir d'une microfiche du document original. La qualité de la copie dépend grandement de la qualité de la thèse soumise pour le microfimage. Nous avons tout fait pour assurer une qualité supérieure de reproduction.

NOTA BENE: La qualité d'impression de certaines pages peut laisser à désirer. Microfilmée telle que nous l'avons reçue.

Division des thèses canadiennes
Direction du catalogage
Bibliothèque nationale du Canada
Ottawa, Canada K1A 0N4

THE UNIVERSITY OF ALBERTA

^{23}Na QUADRUPOLE RELAXATION MEASUREMENTS BY COMPUTER-CONTROLLED NUCLEAR MAGNETIC DOUBLE RESONANCE SPECTROMETER

by

PAUL A. SPENCER (C)

A THESIS

SUBMITTED TO THE FACULTY OF GRADUATE STUDIES AND RESEARCH

IN PARTIAL FULFILLMENT OF THE REQUIREMENTS FOR THE DEGREE

OF DOCTOR OF PHILOSOPHY

DEPARTMENT OF PHYSICS

EDMONTON, ALBERTA

SPRING, 1976

THE UNIVERSITY OF ALBERTA

FACULTY OF GRADUATE STUDIES AND RESEARCH

The undersigned certify that they have read, and recommend to the Faculty of Graduate Studies and Research, for acceptance, a thesis entitled ^{23}Na QUADRUPOLE RELAXATION MEASUREMENTS BY COMPUTER-CONTROLLED NUCLEAR MAGNETIC DOUBLE RESONANCE SPECTROMETER, submitted by Paul A. Spencer, in partial fulfillment of the requirements for the degree of Doctor of Philosophy.

D. G. Hughes
.....
Supervisor

B. Karoyalen
.....

P. D. Ellis
.....

Robert E. Jordan
.....

S. Bywater
.....

R. L. Armstrong
.....
External Examiner

Date: 26 April 1976

ABSTRACT

This thesis describes the development of a minicomputer-controlled steady-state NMDR spectrometer system and its subsequent use to study the ^{23}Na quadrupole spin-lattice relaxation in monocrystalline $NaNO_3$.

The technique is an extension of that used by Pound (1950) and Hughes and Reed (1971), in which the change in amplitude of one component of a quadrupole-split NMR spectrum is measured when another component is severely saturated. Since the NMR signals are weak, we developed an efficient technique for measuring their amplitude, in which the first derivative of the absorption signal is utilized to "lock" the spectrometer frequency to the resonance center, while the second derivative signal is used as a measure of the NMR amplitude. To take full advantage of this novel technique, a minicomputer was used to control, in real time, many subsidiary experimental parameters, such as the magnetic field strength. The minicomputer was also used to collect and process the data. This enabled the relaxation data to be acquired on an around-the-clock basis. To obtain meaningful results from such a system, great attention was paid to the elimination of systematic errors; these are discussed in detail in this thesis.

Extensive tests have shown that the system is capable of measuring NMR amplitudes to an accuracy of about ±0.1%.

The equipment was used to measure the orientation dependence of W_2/W_1 of ^{23}Na in $NaNO_3$ at room temperature. The quantities W_1 and W_2, which are the probabilities of the $\Delta m = \pm 1$ and ± 2 nuclear magnetic transitions respectively, can be expressed as a linear combination of the components of a fourth-rank tensor, the so-called M-tensor.

Excellent agreement was obtained between the data and the theoretical form in which it was assumed that W_1 and W_2 are governed by the same M-tensor. This showed that the spin-lattice relaxation was caused by a multiphonon interaction. An upper limit of 3×10^{-4} s^{-1} was placed on the relaxation due to diffusing charges. The following M-component ratios were found: $M_{1313}/M_{1111} = 0.8025 \pm 0.0035$, $M_{3333}/M_{1111} = 0.7091 \pm 0.0083$, $M_{1113}/M_{1111} = -0.1001 \pm 0.0031$. Comparison of these ratios with the predictions of a point-charge model favours the harmonic rather than the anharmonic Raman process. Comparison with the previous room temperature study made by Reed (1970) revealed significant discrepancies. In particular, we found M_{1123} to be zero, in agreement with crystal symmetry considerations but in disagreement with

Reed's results. We present possible explanations for the discrepancies.

The time-dependent behaviour of the spin-system was experimentally studied, in order to derive the value of W_1 directly. From these results we found that $e^2Q^2M_{1313} = (4.819 \pm 0.050) \times 10^{-1}\ s^{-1}$. This value is compared with that obtained by Niemelä (1967) at 77 K.

ACKNOWLEDGEMENTS

In appreciation, I gratefully acknowledge the continued help and encouragement of my research supervisor, Dr. D.G. Hughes, during the course of this project.

The cooperative attitude of the technical staff of the Department has been a definite asset. I wish, in particular, to thank Mr. Bob Boyd, without whose technical expertise this project would have been infinitely more difficult.

The sincere expression of my gratitude goes to my wife, Judith, for her patience and understanding throughout the course of this lengthy research. I also wish to thank my parents for their encouragement throughout my educational endeavours.

It is a pleasure to acknowledge the University of Alberta for financial support in the form of Graduate Assistantships, and the National Research Council for largely funding the research.

Finally, I would to thank my typist, who, unwilling to submit herself to the arduous task of typing yet another thesis, wishes to remain anonymous.

TABLE OF CONTENTS

		Page
CHAPTER I	INTRODUCTION	1
CHAPTER II	THEORY	7
2.1	Basic theory of nuclear magnetic resonance.	7
2.2	Electric quadrupole moment of the nucleus.	13
2.3	Quadrupole split spectrum.	15
2.4	Modifications to the dipolar broadening.	17
2.5	Quadrupole spin-lattice relaxation.	20
2.6	Orientation dependence of the quadrupole relaxation.	22
2.7	Mechanisms for quadrupole relaxation.	24
CHAPTER III	THE ^{23}Na NMR IN SODIUM NITRATE	27
3.1	Crystallographic information on sodium nitrate.	27
3.2	The NMR spectrum in monocrystalline sodium nitrate.	30
3.3	Orientation dependence of W_1 and W_2.	35
3.4	Spin-lattice relaxation transitions.	39
CHAPTER IV	EXPERIMENTAL METHODS FOR STUDYING THE QUADRUPOLE SPIN LATTICE RELAXATION	44
4.1	Steady state double resonance method for measuring W_2/W_1.	44

		Page
CHAPTER IV	(cont'd)	
	4.2 Transient double resonance method for measuring W_1.	49
CHAPTER V	APPARATUS AND EXPERIMENTAL DETAILS	53
	5.1 Measurement of the NMR enhancement.	53
	5.2 Description of apparatus.	60
	5.2.1 Block diagram.	60
	5.2.2 Probe.	65
	5.2.3 Robinson spectrometer.	66
	5.2.4 Spectrometer level monitor.	72
	5.2.5 The rf power source.	73
	5.2.6 Balance network.	74
	5.2.7 Misbalance detector.	76
	5.2.8 Frequency converter.	78
	5.2.9 Frequency counter.	79
	5.2.10 Frequency adjustment circuitry.	79
	5.2.11 The ω_m and $2\omega_m$ lock-in detectors.	80
	5.2.12 Analogue multiplexer and A/D converter.	84
	5.2.13 Magnet and NMR field-lock.	85
	5.2.14 Manual operation console.	90
	5.2.15 Computer, interface and teletype.	92
	5.2.16 System monitors.	99
	5.2.17 Power supplies.	100

Page

CHAPTER V (cont'd)

5.3 User language computer programs. 101

5.3.1 General considerations. 101

5.3.2 The "Data collection" program. 120

5.3.3 The "Frequency counter interrupt" subroutine. 127

5.3.4 The "Resonance-lock" program. 130

5.3.5 The "Balance network" subroutine. 132

5.3.6 The "NMR field-lock interrupt" subroutine. 136

5.4 Elimination and reduction of systematic errors. 137

5.4.1 Classification of systematic errors. 137

5.4.2 NMR-related systematic errors. 138

5.4.3 Instrumentation-related systematic errors. 147

5.5 Reduction of the random error in the enhancement measurements. 156

5.5.1 Field modulation considerations. 156

5.5.2 Optimization of the data collection. 157

5.6 Experimental details of the transient experiment. 159

5.7 Crystal information. 160

5.8 Determination of the crystal orientation. 161

		Page
CHAPTER VI	RESULTS	163
6.1	Orientation dependence of the quadrupole splitting.	163
6.2	Orientation dependence of the NMR linewidth.	168
6.3	Orientation dependence of W_2/W_1.	174
6.4	Measurement of W_1 by the transient method.	190
CHAPTER VII	DISCUSSION OF THE RELAXATION MEASUREMENTS	200
7.1	Estimation of systematic errors in the relaxation data.	200
7.2	Comparison of the W_2/W_1 results with theoretical predictions.	204
7.3	Comparison with previous room temperature results.	219
7.4	Comparison with 77 K results.	229
CHAPTER VIII	CONCLUSION	236
REFERENCES		240
APPENDIX I	General orientation dependence of W_1 and W_2.	245
APPENDIX II	Calculation of $M_{\alpha\beta\alpha'\beta'}$ for sodium nitrate using a point charge model.	247
APPENDIX III	Selection of P_{obs} values and the optimum utilization of time in the NMR enhancement.	256

LIST OF TABLES

Table		Page
I	Enhancement measurement at $\theta = 180°$.	176
II	θ dependence of W_2/W_1 at $\phi = -3.5°$.	180
III	"First derivative" W_2/W_1 data at $\theta = 180°$.	185
IV	ϕ dependence of W_2/W_1 at $\theta = 120.1°$.	187
V	Enhancement data for second crystal at $\theta = 0°$.	191
VI	Decay constant λ as a function of P_{obs}.	195

LIST OF FIGURES

Figure		Page
3.1	Unit cell of sodium nitrate.	28
3.2	Nearest neighbour oxygen atoms.	31
3.3	Spin-lattice relaxation transitions.	41
5.1	Gaussian lineshape.	56
5.2	Data from one "saturation cycle".	59
5.3	Block diagram of system.	61
5.4	Wiring of probe and Balance network.,	67
5.5	Block diagram of Robinson spectrometer.	70
5.6	Block diagram of NMR field-lock.	87
5.7	Sample user language program.	98
5.8	Flow chart of the "Data collection program".	102
5.9	Flow chart of the "N2" subroutine.	104
5.10	Flow chart of the "156" subroutine.	106
5.11	Flow chart of the "Resonance lock" subroutine.	108
5.12	Flow chart of the "Frequency counter interrupt" subroutine.	110
5.13	Flow chart of the "NMR Field-lock interrupt" subroutine.	112
5.14	Flow chart of the "Balance network interrupt" subroutine.	114
5.15	Flow chart of the "Frequency sweep" program.	116
5.16	Flow chart of the "Transient experiment".	118
5.17	Sample data "printout".	125

Figure		Page
5.18	Block diagram of Robinson-spectrometer frequency-adjustment.	128
5.19	Balance network readjustment procedure.	134
5.20	Enhancement as a function of saturation power offset.	141
5.21	Enhancement of high frequency satellite as a function of P_{obs}.	145
6.1	Satellite splitting.	165
6.2	Linewidth of center line.	170
6.3	Linewidth of satellite line.	172
6.4	Sensitivity of W_2/W_1 to $M_{\alpha\beta\alpha'\beta'}$.	178
6.5	θ dependence of W_2/W_1	181
6.6	ϕ dependence of W_2/W_1	188
6.7	Typical transient experiment data.	193
6.8	λ as a function of P_{obs}.	197
7.1	M_{1313}/M_{1111} for "linear" process.	206
7.2	M_{3333}/M_{1111} for "linear" process.	208
7.3	M_{1113}/M_{1111} for "linear" process.	210
7.4	M_{1313}/M_{1111} for "quadratic" process.	213
7.5	M_{3333}/M_{1111} for "quadratic" process.	215
7.6	M_{1113}/M_{1111} for "quadratic" process.	217
7.7	Discrepancy in W_2/W_1 data.	222
7.8	Proposed baseline offset.	225
7.9	Reed's values of W_2/W_1 at $\phi = 86.5°$.	230
A2.1	Point charge configuration	248

CHAPTER I

INTRODUCTION

Nuclei with spin quantum number $I \geq 1$ can interact with their surroundings in two ways; a magnetic interaction involving the nuclear magnetic dipole moment and the magnetic field at the nuclear site, and an electrostatic interaction involving the nuclear electric quadrupole moment and the electric field gradient at the nuclear site. The time-averaged magnetic and electrostatic interactions determine the structure of the nuclear magnetic resonance (NMR) spectrum. The so-called high field case is where the sample is situated in a large magnetic field such that the Zeeman interaction is large compared with the static electric quadrupole interaction. For equivalent nuclei with spin number $I = 3/2$ situated in a solid at sites of lower than cubic symmetry, one obtains a three-line spectrum provided the sample is in the form of a single crystal.

The so-called spin-lattice interaction caused by time dependent magnetic fields and electric field gradients, results in a coupling between the nuclei and their surroundings (the lattice). The magnetic interaction can change the nuclear magnetic quantum number m by ± 1. In contrast, the electric quadrupole

interaction can change m by ±1 or ±2. The corresponding transition probabilities for the case I = 3/2 are denoted by W_1 and W_2 respectively.

Pound (1950) performed a steady-state double resonance experiment on ^{23}Na nuclei (for which I = 3/2) in sodium nitrate. By measuring the change in amplitude of one resonance when one of the others is severely saturated by a large rf field, he was able to demonstrate that the spin-lattice relaxation mechanism was quadrupolar rather than magnetic. Later, Abragam (1961) pointed out that it was possible to obtain values of W_2/W_1 from a double resonance experiment of the type used by Pound.

Using an extension of Pound's method, Reed (1970), in this laboratory, made a detailed study of the orientation dependence of W_2/W_1 for ^{23}Na in sodium nitrate at room temperature.

Pietilä (1968) and Snyder and Hughes (1971) showed that W_1 and W_2 are governed by a fourth-rank tensor, the so-called M-tensor. The sodium nuclei in sodium nitrate are situated at sites possessing $\bar{3}$ symmetry, and it can be shown that there are in this case only five independent M-tensor components. By fitting the orientation dependence of W_2/W_1 to the theoretical form, Reed obtained ratios of the M-tensor components. His work indicated that the same M-tensor

governs W_1 and W_2. This implies (Snyder and Hughes, 1971) that the spin-lattice interaction is a Raman-type multiphonon interaction (Van Kranendonk, 1954; Van Kranendonk and Walker, 1967, 1968). Reed found generally good agreement with the theoretical form, except that the M_{1123} component was non-zero, in disagreement with crystal symmetry considerations.

In the meantime, Niemelä (1967) measured the orientation dependence of W_1 and W_2 for the same nuclear spin system at 77 K. Niemelä obtained his values of W_1 and W_2 by studying the approach to equilibrium of the spin system. His measurement technique was different from Reed's in that the resonances were observed using a pulsed NMR technique (Hahn, 1950), rather than a steady-state method. Niemelä unfortunately misinterpreted his data. However, the M-tensor values were later derived from Niemelä's results by Hughes et al (1970) and were found to be rather similar to the room-temperature values obtained by Reed (1970). Niemelä's data did not allow the value of M_{1123} to be determined in his crystal.

The work described in this thesis was undertaken in order to investigate further why the M_{1123} component was non-zero in sodium nitrate. A steady-state technique was chosen in preference to a pulsed technique

since the ^{23}Na resonances are rather closely spaced and thus could not be selectively excited by the pulses. However, to obtain an accuracy of ∿1% in W_2/W_1, it is necessary to measure resonance amplitudes to an accuracy of ∿0.1% in the steady-state double resonance technique. To obtain such accuracy obviously requires a sophisticated detection system in which particular attention is paid to linearity for example. Moreover, the signal-to-noise ratio is such that several days of data collection are required at each crystal orientation. It was thus felt that a computer controlled data acquisition system operating twenty-four hours per day was required. Reed's method consisted of recording the complete resonances in first derivative form, and using the peak-to-peak amplitude as a measure of NMR signal amplitude. However, in this method, only a small fraction of the data collected is used. We therefore used a different method for measuring the NMR signal amplitude. In our technique which we believe to be novel, the first derivative signal is used to lock the spectrometer to the resonance center, and the second derivative signal is used as a measure of the NMR signal amplitude. However, to take full advantage of this more efficient technique, tighter control has to be exercised over several experimental parameters. It was decided that the only

practical way of controlling such a complex system was by means of a real-time minicomputer.

Considerable time was spent in designing and constructing the system. After the system was operational, it was discovered that the data obtained suffered from a number of systematic errors. The elimination of these errors proved to be difficult, although illuminating. However, the final configuration seems to be capable of measuring resonance amplitudes to an accuracy of about ±0.1%.

A detailed study of the orientation dependence of W_2/W_1 of ^{23}Na in sodium nitrate at room temperature was then performed. Significant discrepancies were found between our results and those of Reed, and we present possible explanations for these.

The steady-state double resonance technique does not give the magnitude of W_1 or W_2 but merely gives their ratio. It is useful, and especially so for comparing measurements at different temperatures, to measure these quantities separately. The flexibility afforded by the minicomputer enabled the approach to equilibrium of the spin system to be experimentally studied. From this so-called transient experiment, the value of W_1 was obtained.

The theory is presented in Chapter II and is applied to the specific case of ^{23}Na in sodium nitrate in Chapter III. The method of obtaining W_2/W_1 and W_1 from the experimental data is described in Chapter IV. The experimental details are presented in Chapter V, the results obtained are given in Chapter VI and are discussed in the following chapter.

CHAPTER II

THEORY

2.1 Basic theory of nuclear magnetic resonance

We shall consider a simple description of the phenomenon of nuclear magnetic resonance. If we have a nucleus with a magnetic moment $\underline{\mu}$ and colinear angular momentum $\hbar\underline{I}$ immersed in a magnetic field $\underline{H}_o$, then the Hamiltonian of the system is

$$\mathcal{H} = -\underline{\mu}\cdot\underline{H}_o = -\gamma\hbar\underline{H}_o\cdot\underline{I} = -\gamma\hbar H_o I_z \qquad (2.1)$$

where $\underline{H}_o$ is along the z axis, I_z is the z component of $\underline{I}$, and the gyromagnetic ratio γ is defined by

$$\gamma = \underline{\mu}/\underline{I}\hbar \quad . \qquad (2.2)$$

This is the well known Zeeman interaction, and the eigenvalues of $\mathcal{H}$ are given by

$$E_m = -\gamma\hbar H_o m \qquad (2.3)$$

where the magnetic quantum number m can take the values I,(I-1)....-I. The maximum component of $\underline{I}$ is equal to $I\hbar$ where the so-called nuclear spin quantum number I has either integral or half integral values.

To detect such a system of energy levels one needs a resonant interaction that can cause transitions between them. In order to cause transitions between the

m and m' energy levels, a radiation field of angular frequency ω must satisfy the condition

$$\hbar\omega = |E_m - E_{m'}| \quad . \tag{2.4}$$

An alternating magnetic field perpendicular to $\underline{H}_o$ will cause magnetic transitions between energy levels related by $m' = m \pm 1$. We therefore obtain the magnetic resonance condition

$$\omega = \gamma H_o \quad . \tag{2.5}$$

The frequency ω is also known as the Larmor frequency since it coincides with the classical precession frequency of a magnetic moment in a steady magnetic field. For fields of order 10^4 gauss, the resonant frequency for nuclei occurs within the radio frequency (rf) range 0.1 to 50 MHz.

According to first order perturbation theory, the probability of these magnetic transitions is given by (Bloembergen, Purcell and Pound, 1948; hereafter referred to as BPP)

$$P_{m\to m-1} = P_{m-1\to m} = (1/4)\gamma^2 H_1^2 g(\omega)(I + m)(I - m + 1) \quad . \tag{2.6}$$

Here, H_1 is the amplitude of the circularly polarized rf magnetic field and $g(\omega)$ is a normalized lineshape function which takes into account the finite width of the magnetic resonance signal. For an ensemble of

nuclei, in a solid for example, transitions with probability given by (2.6) will cause the energy levels to become equally populated. The spin system is then said to be completely saturated, and its temperature is infinite. In practice, the spin system is embedded in a "lattice" with which it interacts. However, essentially complete saturation can still be obtained provided this so-called spin-lattice interaction is weak compared with the interaction with the H_1 field. In the absence of a H_1 field, the spin system will come into equilibrium with the lattice, and the ratio of the populations of adjacent energy levels is given by the Boltzmann factor $\exp|\Delta E/kT_L|$, where ΔE is $E_m - E_{m-1}$ and T_L is the lattice temperature. Correspondingly, the ratio of the upward and downward spin-lattice transition probabilities is equal to the same Boltzmann factor. For nuclei at room temperature, ΔE is typically much less than kT_L and the exponent can be replaced by $1 + (\Delta E/kT_L)$.

If we now consider the case of $I = 1/2$, eg protons, then the lower of the two energy levels will be slightly more populated than the upper. Thus when H_1 is applied and the resonance condition is satisfied, there is a net absorption of energy from the radiation field. The magnetic resonance condition can therefore be detected by monitoring the radiation field. The field H_1 will tend to equalize the energy level populations, whereas

the spin-lattice interaction will tend to maintain the spin system in equilibrium with the lattice. From the principle of detailed balancing, we find that the difference N_o between the population of the two energy levels satisfies the expression

$$\dot{N}_o = 2W(n_o - N_o) - 2N_oP \qquad (2.7)$$

where from eq. (2.6),

$$P = (1/4)\gamma^2 H_1^2 g(\omega) \qquad (2.8)$$

and n_o is the equilibrium value of N_o in the absence of H_1. In eq. (2.7), W is the spin-lattice relaxation rate between the two energy levels. (Since the Boltzmann factor differs so little from unity, there is no need to distinguish here between the upward and downward transition rates.) In the absence of H_1, the solution of eq. (2.7) is

$$N_o = n_o[1 - C\exp(-2Wt)] \qquad (2.9)$$

where C is a constant determined by the initial conditions. The time constant of the decay $(2W)^{-1}$ is called the spin-lattice relaxation time T_1. Using eqs. (2.7) and (2.8), we find the steady state solution

$$N_o = \frac{n_o}{1 + (1/2)\gamma^2 H_1^2 g(\omega) T_1}, \qquad (2.10)$$

an expression first derived by BPP.

The width and shape of the NMR absorption signal is, in general, governed by several factors. Perhaps the most obvious is an inhomogeneity in H_o; however, this is an experimental detail rather than a fundamental effect. The finite lifetime of the energy levels leads, according to the uncertainty principle, to a linewidth of order $(T_1)^{-1}$ (expressed in frequency units). Another source of broadening is the magnetic dipolar coupling between nuclear spins. A typical nuclear magnetic dipole produces a field of order one gauss at a distance of three angstrom units. Thus in solids, the steady magnetic field will not be the same at each nucleus, but will vary by several gauss from one nucleus to another, thereby contributing to the linewidth. However, there is another contribution to the linewidth. One nucleus produces an alternating magnetic field at the site of another. If the nuclei are identical, the alternating field is at the Larmor precession frequency of the second nucleus, and as a result may induce a transition. This mutual interaction reduces the lifetime of the energy levels of these nuclei, thus producing a "lifetime broadening", which turns out to be comparable to the other effect. This mutual exchange does not occur for unlike nuclei, whereas the first effect is still present.

The calculation of the NMR lineshape caused by magnetic dipolar interactions is a formidable task. However, as was shown by Van Vleck (1948), the calculation of the moments of the NMR line is much more tractable. The moments are usually expressed in frequency units, and are defined by

$$M_n = \int (\omega - \omega_o)^n g(\omega) d\omega \qquad (2.11)$$

where ω_o is the resonance center frequency. In particular, Van Vleck found that the second moment of the resonance of a spin species with gyromagnetic ratio γ_I and spin I is given by

$$M_2 = \frac{3}{4} \frac{\gamma_I^4 \hbar^2 I(I+1)}{N} \sum_{j,k} \frac{(1 - 3\cos^2\theta_{jk})^2}{r_{jk}^6} + \frac{1}{3} \sum_S \left\{ \frac{\gamma_I^2 \gamma_S^2 \hbar^2 S(S+1)}{N} \sum_{j,\ell} \frac{(1 - 3\cos^2\theta_{j\ell,S})^2}{r_{j\ell,S}^6} \right\} \qquad (2.12)$$

where γ_S and S are the gyromagnetic ratio and spin of an unlike spin species, N is the number of I spins in the unit cell, θ_{jk} is the angle between $\underline{H}_o$ and the internuclear vector $\underline{r}_{jk}$, and $\theta_{j\ell,S}$ is the angle between $\underline{H}_o$ and $\underline{r}_{j\ell,S}$. The summation j is over all spins I in the unit cell, the summation k is over all the I spins in the solid, and the summation ℓ is over all the unlike spins S.

As indicated by BPP, another interaction between nuclei and the lattice is possible if $I \geq 1$. In this case, the nucleus may possess an electric quadrupole moment which can interact with electric field gradients at the nuclear site. This interaction has three main effects; if the time-averaged electric field gradient is nonzero then additional structure in the NMR spectrum can result; these changes in the spectrum require modifications to the Van Vleck (1948) theory of second moment; if the electric field gradient is fluctuating then an additional spin-lattice interaction is provided. These effeots will be discussed in the following sections of this chapter.

2.2 Electric quadrupole moment of the nucleus

The Hamiltonian for the electrostatic interaction of the nucleus with electric fields is given by

$$\mathcal{H} = \int \rho(r) V(r) dv \qquad (2.13)$$

where $\rho(r)$ is the charge density of the nucleus, $V(\underline{r})$ is the electric potential produced by charges external to the nucleus, and the integral is taken over the nuclear volume. If we expand $V(\underline{r})$ in a Taylor series about the nuclear center of mass, eq. (2.13) can be written in the following form

$$\mathcal{H} = ZeV_o + \sum_j P_j \left(\frac{\partial V}{\partial x_j}\right) + \frac{1}{2} \sum_{j,k} Q'_{jk} \left(\frac{\partial^2 V}{\partial x_j \partial x_k}\right) + \ldots \quad (2.14)$$

where

$$P_j = \int x_j \rho(\underline{r}) dv$$

and

$$Q'_{jk} = \int x_j x_k \rho(\underline{r}) dv \ .$$

The first term in the expansion represents the electrostatic energy of a point charge nucleus, and is thus independent of the nuclear shape or orientation. The second term is zero since the nuclear electric dipole moment P_j is identically zero when measured relative to the nuclear center of mass. The third term involves the nuclear electric quadrupole moment tensor Q'_{jk} and the electric field gradient tensor. The next term in the series involves the nuclear electric octopole moment. However, this is again identically zero. The following term involves the nuclear electric hexadecapole moment, which is also zero if $I < 2$ (Abragam,1961; Cohen and Reif, 1957). Thus, in our work where we study the ^{23}Na nucleus for which I is 3/2, we need only consider the electric quadrupole interaction. Since the nucleus is in a state of definite angular momentum, i.e. the charge has cylindrical symmetry on account of its rapid spin, it can be shown (Abragam, 1961) that the orientation dependent part of the nuclear electric quadrupole

interaction can be expressed in terms of a scalar quantity, the so-called electric quadrupole moment eQ which is defined by

$$eQ = \int (3z'^2 - r^2)\rho(\underline{r})dv \qquad (2.15)$$

where z' is the axis of spin of the nucleus.

2:3 Quadrupole split spectrum

The Hamiltonian of a nucleus with quadrupole moment eQ which is situated in a magnetic field $\underline{H}_o$ and in an electric field gradient can be written (Abragam, 1961)

$$\mathcal{H} = -\gamma\hbar\underline{H}_o \cdot \underline{I} + \frac{e^2qQ}{4I(2I-1)} [3I_z^2 - I(I+1) + \frac{1}{2}\eta(I_+^2 + I_-^2)] \qquad (2.16)$$

where $I_\pm = I_x \pm iI_y$. Here the x, y, z axes are the principal axes of the electric field gradient tensor, arranged such that

$$|V_{zz}| \geq |V_{xx}| \geq |V_{yy}| \qquad (2.17)$$

where $V_{\alpha\beta}$ is $\partial^2 V/\partial x_\alpha \partial x_\beta$. The electric field gradient eq and the asymmetry parameter η are then defined by the equations

$$eq = V_{zz} \qquad (2.18)$$

$$\eta = (V_{xx} - V_{yy})/V_{zz} \qquad (2.19)$$

(Since the electrostatic potential at the nuclear site satisfies Laplace equation $\nabla^2 V = 0$, there are only two independent components $V_{\alpha\alpha}$ in the principal coordinate system. The quantities eq and η therefore completely specify the field gradient tensor.)

If the site possesses spherical or cubic symmetry, then by Laplace equation eq is zero. If the site is situated on an n-fold axis of symmetry with $n \geq 3$, the asymmetry parameter is zero (Cohen and Reif, 1957); eq is of course in general nonzero. For lower symmetry both eq and η are in general nonzero.

The energy levels of the system can be readily found by a perturbation approach if the quadrupole interaction is either large (Das and Hahn, 1958) or small compared with the Zeeman interaction. In fields of order 10^4 gauss, the electric quadrupole interaction of ^{23}Na in solids falls into the latter category, the so-called high field case. According to first order perturbation theory (Abragam, 1961), the energy levels are given by

$$E_m = -h\nu_o m + (\tfrac{1}{4})h\nu_Q \cdot [3\cos^2\theta - 1 + \eta\sin^2\theta\cos 2\phi] \cdot \cdot [m^2 - (\tfrac{1}{3})I(I+1)] \qquad (2.20)$$

where the unperturbed frequency ν_o is equal to $\gamma H_o/2\pi$ and

$$\nu_Q = 3e^2qQ/[h2I(2I-1)] \; . \qquad (2.21)$$

The angles θ and ϕ are the polar and azimuthal angles of $\underline{H}_o$ relative to the principal axes of the electric field gradient. The second order perturbation term is in general quite complicated (Volkoff, 1953). Thus, we only present it for the special case of $\eta = 0$:

$$E_m^{(2)} = -h\left(\frac{\nu_Q^2}{12\nu_o}\right)m\left(\frac{3}{2}\cos^2\theta(1-\cos^2\theta)(8m^2+1-4I(I+1))\right.$$

$$\left. - \frac{3}{8}(1-\cos^2\theta)^2(2m^2+1-2I(I+1))\right). \qquad (2.22)$$

For the case $I = n + \frac{1}{2}$, it follows from eq. (2.20) that the first order NMR spectrum consists of an unperturbed center line corresponding to the $m = \frac{1}{2} \leftrightarrow -\frac{1}{2}$ transition, flanked by n pairs of satellite lines. Each member of a satellite pair is symmetrically disposed relative to the center line, and the maximum splitting is of order ν_Q. According to the second order perturbation theory, all the resonance lines are in general perturbed, the maximum shift being of order ν_Q^2/ν_o. However, this shift is the same for both the upper and lower members of a satellite pair, so that their separation is unaffected by second order quadrupole effects.

2.4 Modifications to the dipolar broadening

For the case of arbitrary spin and no quadrupole interaction, the resonance frequencies of the various magnetic transitions coincide. This degeneracy is

removed by the quadrupole shift in the resonance frequencies. Thus, the Van Vleck (1948) theory of dipolar broadening has to be modified in order to take into account the fact that not all nuclei now contribute to the broadening in the same way. The theory has been extended by Kambe and Ollom (1956) and Abragam (1961) for the center line resonance for half integer nuclear spin.

We now define "like" nuclei to be nuclei of the same species in equivalent sites having the same electric field gradient. Thus "like" nuclei have identical NMR spectra. The contribution M_2' of such nuclei to the second moment of the center line is (Abragam, 1961)

$$M_2' = \left\{ \frac{4I(I+1)}{27} + \frac{2I^2(I+1)^2 + 3I(I+1) + \frac{13}{8}}{18(2I+1)} \right\} \gamma_I^4 \hbar^2 \cdot \sum_{j,k} \frac{(1 - 3\cos^2\theta_{jk})^2}{r_{jk}^6} \qquad (2.23)$$

where the summation is over all "like" nuclei, and the remaining symbols have their usual meaning.

If we define "semi-like" nuclei to be nuclei of the same species but located at inequivalent sites in the unit cell, then, to first order, the center lines overlap and the satellite lines do not. The contribution M_2'' from "semi-like" nuclei to the second moment of the center line is (Abragam, 1961)

$$M_2'' = \frac{1}{9}\left(\frac{4I(I+1)}{3} + \frac{(2I+1)}{2} + \frac{(2I+1)^3}{32}\right)\gamma_I^4\hbar^2 \cdot \sum_{j,k} \frac{(1 - 3\cos^2\theta_{jk})^2}{r_{jk}^6} \quad (2.24)$$

For unlike nuclei, i.e. those of a different species, the second moment contribution is the same as that given by the Van Vleck formula (eq.(2.12)). Comparison of eqs.(2.23) and (2.24) with the Van Vleck formula shows that the center line is narrower than it is where there is no quadrupole splitting.

According to Betsuyaku (1969), the second moment of the $m \leftrightarrow m-1$ resonance for the case of "like" spins is given by

$$M_2' = \left(\frac{I(I+1)}{3} + \frac{1}{4(2I+1)}\{I^2(I+1)^2 - I(I+1)(2a-1) + a^2 + a - 1\}\right) \cdot \gamma_I^4\hbar^2 \sum_{j,k} \frac{(1 - 3\cos^2\theta_{jk})^2}{r_{jk}^6} \quad (2.25)$$

For example, it can be shown that for the case $I = 3/2$, the ratio of the second moment of a satellite to the second moment of the center line is 0.852 for the case of broadening by "like" spins.

2.5 Quadrupole spin-lattice relaxation

We shall now consider the effect of a fluctuating electric field gradient at the nuclear site. Using the notation of Pietilä (1968) and Snyder and Hughes (1971), the Hamiltonian of this interaction can be written in the form

$$\mathcal{H}_Q = \sum_{\mu=-2}^{+2} Q_\mu (B^\mu)^* \qquad (2.26)$$

where

$$B^0 = V_{zz}/2$$

$$B^{\pm 1} = (1/\sqrt{6})(V_{xz} \pm iV_{yz})$$

$$B^{\pm 2} = (1/\sqrt{6})(\tfrac{1}{2}(V_{xx}-V_{yy}) \pm iV_{xy})$$

$$Q^0 = k\{3I_z^2 - I(I+1)\}$$

$$Q^{\pm 1} = \pm k(\sqrt{6}/2)(I_z I_\pm + I_\pm I_z)$$

$$Q^{\pm 2} = k(\sqrt{6}/2) I_\pm^2$$

and

$$k = eQ/\{2I(2I-1)\} \ .$$

In a right handed coordinate system (x',y',z') in which $\underline{H}_o$ lies along the z' axis (the x',y' axes being arbitrary) the matrix elements of Q^μ are

$$Q_{\pm 1,m} = \langle m\pm 1|Q^{\pm 1}|m\rangle$$

$$= \pm(\sqrt{6}/2)k(2m\pm 1)\{(I\pm m+1)(I\mp m)\}^{1/2} \qquad (2.27)$$

$$Q_{\pm 2,m} = \langle m\pm 2|Q^{\pm 2}|m\rangle$$

$$= (\sqrt{6}/2)k\{(I\mp m)(I\mp m-1)(I\pm m+1)(I\pm m+2)\}^{1/2} \qquad (2.28)$$

provided the quadrupole interaction is small compared with the Zeeman interaction. It can be shown by a perturbation approach that the relaxation probabilities for transitions which change the magnetic quantum number by one and two respectively are (Hughes, 1973)

$$W_{m\to m+1} = \frac{2\pi\lambda_1^2}{\hbar} \cdot \frac{\sum_{nn'} \exp(-\beta E_n) |\langle n'|V_{x'z'} - iV_{y'z'}|n\rangle|^2}{\sum_{nn'} \exp(-\beta E_n)} \cdot$$

$$\cdot \delta(E_{n'} - E_n + E_{m+1} - E_m) \qquad (2.29)$$

$$W_{m\to m+2} = \frac{2\pi\lambda_2^2}{\hbar} \cdot \frac{\sum_{nn'} \exp(-\beta E_n) |\langle n'|(\tfrac{1}{2})(V_{x'x'} - V_{y'y'}) - iV_{x'y'}|n\rangle|^2}{\sum_{nn'} \exp(-\beta E_n)}$$

$$\cdot \delta(E_{n'} - E_n + E_{m+2} - E_m) \qquad (2.30)$$

where

$$\lambda_1 = (k/2)(2m+1)[(I-m)(I+m+1)]^{1/2}$$

$$\lambda_2 = (k/2)[(I-m)(I-m+1)(I+m+1)(I+m+2)]^{1/2} .$$

Here n and n' are initial and final lattice states, E_n is an eigenvalue of the lattice and β is $(kT_L)^{-1}$. The m dependence of the multiplicative factors is removed by defining W_1 and W_2 in the following way (Yosida and Moriya, 1956)

$$W_{m\to m+1} = \frac{W_1 (2m+1)^2 (I+m+1)(I-m)}{2I(2I-1)^2} \tag{2.31}$$

$$W_{m\to m+2} = \frac{W_2 (I-m)(I-m+1)(I+m+1)(I+m+2)}{2I(2I-1)^2} \tag{2.32}$$

Thus it follows that W_1 and W_2 can be written as

$$W_1 = \frac{\pi e^2 Q^2}{4I\hbar} \cdot \frac{\sum_{nn'} \exp(-\beta E_n) \left| \langle n' | V_{x'z'} - iV_{y'z'} | n \rangle \right|^2}{\sum \exp(-\beta E_n)} \cdot$$

$$\cdot \delta(E_{n'} - E_n + E_{m+1} - E_m) \tag{2.33}$$

$$W_2 = \frac{\pi e^2 Q^2}{4I\hbar} \cdot \frac{\sum_{nn'} \exp(-\beta E_n) \left| \langle n' | \left(\tfrac{1}{2}\right)(V_{x'x'} - V_{y'y'}) - iV_{x'y'} | n \rangle \right|^2}{\sum_{nn'} \exp(-\beta E_n)} \cdot$$

$$\cdot \delta(E_{n'} - E_n + E_{m+2} - E_m) \ . \tag{2.34}$$

The probabilities W_1 and W_2 govern the relaxation behaviour of the various resonances in the quadrupole split spectrum. Their magnitudes are in general different because they involve different field gradient components. However, they are expected to be of the same order of magnitude.

2.6 Orientation dependence of the quadrupole relaxation

In the high field case, the external magnetic field $\underline{H}_o$ determines the axis of quantization. We have seen in section 2.3 that the NMR spectrum changes when we rotate $\underline{H}_o$ relative to the crystallographic axes.

Similarly, the quadrupole relaxation probabilities vary with the orientation of $\underline{H}_o$ relative to the crystal.

To calculate the orientation dependence of W_1 and W_2 we transform equations (2.33) and (2.34) from the primed coordinate system to an unprimed (right handed) coordinate system fixed with respect to the crystal. The polar and azimuthal angles of $\underline{H}_o$ relative to the new coordinate system are denoted by θ and ϕ. The transition probabilities W_1 and W_2 can then be expressed as linear combinations of a fourth rank tensor (Nye, 1957; Pietilä, 1968)

$$L_{\alpha\beta\alpha'\beta'} = \frac{2\pi}{\hbar} \frac{\sum_{nn'} \exp(-\beta E_n) \langle n'|V_{\alpha\beta}|n\rangle^* \langle n'|V_{\alpha\beta}|n\rangle \delta(E_{n'}-E_n+E_{m+\mu}-E_m)}{\sum_{nn'} \mathrm{Exp}(-\beta E_n)} \tag{2.35}$$

where $\alpha,\beta,\alpha',\beta' = 1,2,3 \equiv x,y,z$ and $\mu = 1$ for W_1 and 2 for W_2. In general the $L_{\alpha\beta\alpha'\beta'}$ are complex and thus we write

$$L_{\alpha\beta\alpha'\beta'} = M_{\alpha\beta\alpha'\beta'} + iN_{\alpha\beta\alpha'\beta'} \tag{2.36}$$

from which it follows that

$$M_{\alpha\beta\alpha'\beta'} = M_{\alpha'\beta'\alpha\beta} \tag{2.37}$$

$$N_{\alpha\beta\alpha'\beta'} = -N_{\alpha'\beta'\alpha\beta} \tag{2.38}$$

Also, since $V_{\alpha\beta} = V_{\beta\alpha}$, and from Laplace equation $\sum_{\alpha} V_{\alpha\alpha} = 0$, there are only fifteen independent $M_{\alpha\beta\alpha'\beta'}$ components and ten independent $N_{\alpha\beta\alpha'\beta'}$ components.

If the lattice satisfies the principle of time reversal invariance (Goldberger and Watson, 1964) it can be shown (Hughes, 1973) that the quadrupole relaxation tensor is real. Even if time reversal invariance is not satisfied, then the $L_{\alpha\beta\alpha'\beta'}$ components are real provided the site possesses inversion symmetry (Hughes, 1973). We shall give the general orientation dependence of W_1 and W_2 for the case of a real relaxation tensor in appendix I, since these expressions are somewhat lengthy. Fortunately crystal symmetry will reduce the number of independent $M_{\alpha\beta\alpha'\beta'}$ components (Snyder and Hughes, 1971) except for the case of triclinic point group symmetry. In particular, for ^{23}Na in sodium nitrate where the point group symmetry is $\bar{3}$, there are only five independent $M_{\alpha\beta\alpha'\beta'}$ components.

2.7 Mechanisms for quadrupole relaxation

We now discuss various mechanisms which have been proposed for the quadrupolar interaction of the nuclei with the lattice phonons in a solid. The quantities B^{μ} which occur in eq. (2.26) contain the information regarding the lattice vibrations and hence the fluctuating field gradients. Expanding B^{μ} in a Taylor series

about the equilibrium position, we obtain

$$B^{\mu} = \left(B^{\mu}\right)_o + \sum_j \left(\frac{\partial B^{\mu}}{\partial x_j}\right)_o u_j + \frac{1}{2} \sum_{j,k} \left(\frac{\partial^2 B^{\mu}}{\partial x_j \partial x_k}\right)_o u_j u_k + \ldots \quad (2.39)$$

where the u_j are components of the relative displacements and $(\ )_o$ signifies that the quantity is evaluated at the equilibrium position. Spin-lattice mechanisms involving the term linear in the displacement or quadratic in the displacement have been proposed by Van Kranendonk (1954). An example of one involving the linear term is the so-called direct process in which a lattice phonon is either created or annihilated. These phonons have a frequency equal to the resonance frequency ($\simeq 10^7$ Hz) and, except at very low temperatures, constitute only a small fraction of the total phonon population. An example of an interaction involving the quadratic term is the indirect harmonic Raman process. Here, an incoming phonon interacts with the nuclear spin thereby producing a phonon of different energy, the energy difference being taken up by the nuclear spin. This interaction involves phonons from the whole phonon spectrum, and is therefore likely to be much more important than the direct process. Van Kranendonk and Walker (1967, 1968) have suggested a third possibility which they call the anharmonic Raman process. If the lattice potential energy is expanded in a Taylor series about the equilibrium configuration,

the quadratic term constitutes the harmonic description of the lattice whereas higher order terms give rise to anharmonic effects. The anharmonic Raman process involves the first (cubic) anharmonic term in conjunction with the linear term in eq. (2.39). This interaction is similar to the harmonic Raman process except that an additional virtual phonon is involved. Van Kranendonk and Walker (1967, 1968) have shown that for both Raman processes, the relaxation rates have the same temperature dependence, namely

$$\begin{aligned} W_1, W_2 &\propto T^{*7} && \text{for } T^* \lesssim 0.02 \\ &\propto T^{*2}(1 - kT^{*2}) && \text{for } T^* \gtrsim 0.5 \end{aligned} \qquad (2.40)$$

where T^* is the so-called reduced temperature T_L/θ_D, where θ_D is the Debye temperature. The constant k is very much less than unity. Pietilä (1968) has shown that for ^{23}Na in NaCl, the harmonic and anharmonic Raman mechanisms are almost the same strength at room temperature. Which mechanism, if either, proves to be dominant in a particular crystal is therefore still an open question.

CHAPTER III

THE ^{23}Na NMR IN SODIUM NITRATE

3.1 Crystallographic information on sodium nitrate

We need the structure of the crystal in order to predict the electrostatic and magnetic environment of the ^{23}Na sites. This explains the NMR of ^{23}Na in sodium nitrate.

Sodium nitrate belongs to the rhombohedral crystal system (space group $R\bar{3}c$, D^6_{3d}) and has two units of $NaNO_3$ per unit cell. As can be seen from Fig. 3.1, the nitrogen atoms are situated at the corners of the unit cell and also at 1/2, 1/2, 1/2, whereas the sodium atoms are at 1/4, 1/4, 1/4 and 3/4, 3/4, 3/4. The nitrate groups lie in a plane perpendicular to the three-fold axis, and consist of equilateral triangles of oxygen atoms with a nitrogen atom at the centroid of the triangle. The edges of the nitrate group triangles are parallel to the projection of the unit cell edges in a plane perpendicular to the three-fold axis. The orientation of the nitrate groups alternate by 180° along this axis. At room temperature, the length of the body diagonal is 16.82 A°, the length of the unit cell edge is 5.070 A°, and the nitrogen-oxygen bond length is 1.257 A° (Paul and Pryor, 1971). At room temperature, the motion of

Figure 3.1

The unit cell of sodium nitrate. For clarity only two groups of oxygen atoms are shown.

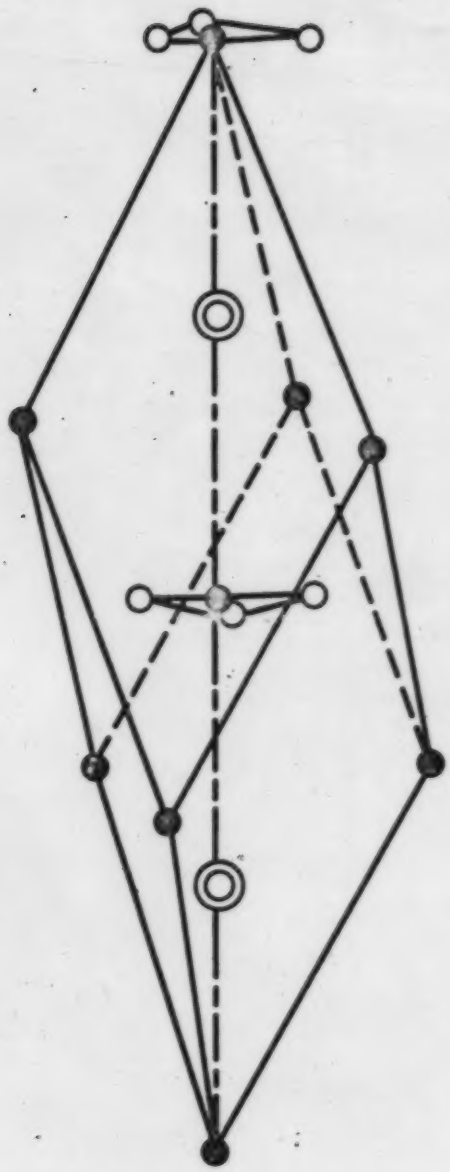

◎ Na

● N

○ O

the sodium nuclei is almost completely isotropic, whereas the motion of the oxygen atoms is somewhat anisotropic (Cherin et al, 1967; Paul and Pryor, 1971).

Near 276°C, the structure undergoes a second order phase transition. This is believed to be an order-disorder type of transition in which the orientation of the nitrate groups becomes disordered. Above the phase transition the nitrate groups are statistically distributed among the two allowable positions (D'Alesio and Scott, 1971 and references therein).

As there are two sodium atoms per unit cell in the room temperature phase, this means that their environments are not identical. Each site possesses $\bar{3}$ symmetry, the time-averaged field gradient component $\overline{V_{zz}}$ being the same at both sites. However, properties which involve a fourth-rank tensor are not necessarily identical at these sites. The difference between the environments of the two sites can be seen in Fig. 3.2. The environments are, in each case, similar but are differently oriented in space, being symmetrically disposed with respect to the three axial glide-planes of the crystal.

3.2 The NMR spectrum in monocrystalline sodium nitrate

Since each sodium nucleus in the unit cell has an identical static electric field gradient and since I is

Figure 3.2

The plan view of the nearest neighbour oxygen atoms for the A and B sodium sites. The chain lines represent the intersections of the glide planes with the x-y plane. The principal axes of the M-tensor for the two sites are shown as x_A, y_A and x_B, x_B. Also shown is the projection of the magnetic field $\underline{H}_o$ onto the x-y plane.

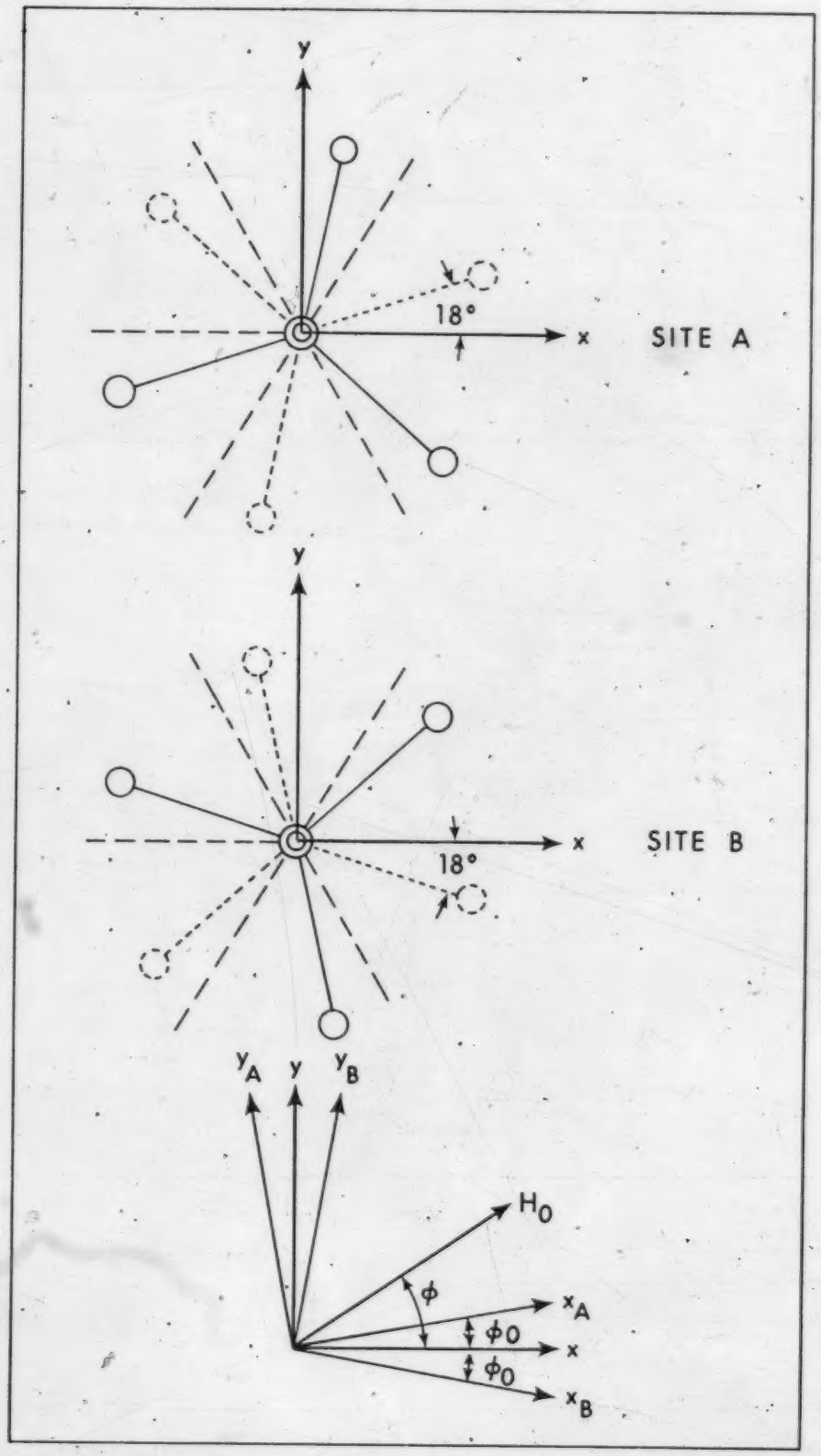
y
18°
x
SITE A
y
x
18°
SITE B
y_A
y
y_B
H_0
ϕ
x_A
ϕ_0
x
ϕ_0
x_B

equal to 3/2, the NMR spectrum consists of a center line and one pair of satellite lines. It follows from eqs. (2.20) and (2.22) that the resonance frequencies are given by

$$\nu_{\pm}/\nu_o = 1 \pm (\rho/4)(3\cos^2\theta - 1 + \eta \sin^2\theta \cos 2\phi) + (3/32)\rho^2 \sin^2 2\theta \qquad (3.1)$$

$$\nu_c/\nu_o = 1 - (3/64)\rho^2(9\cos^2\theta - 1)\sin^2\theta \qquad (3.2)$$

where $\nu_{\pm}$ is the frequency of the high or low frequency satellite, ν_c is the center line frequency and ρ is $e^2Qq/h\nu_o$. It is believed that the sodium nuclei are situated on a three-fold axis; the asymmetry parameter η in eq. (3.1) should therefore be zero. A measure of the static quadrupole interaction is e^2Qq/h, the so-called quadrupole coupling constant. At room temperature, this has a value of approximately 335 kHz and a temperature coefficient of -0.33 kHz/°C (Andrew et al, 1962). At a field of approximately 6700 gauss (the strength of our magnet), the unperturbed resonance frequency ν_o is 7.55 MHz. Thus, the second order quadrupole shifts are less than 2 kHz and any third order shifts (Bersohn, 1952) will be less than 10 Hz.

Inspection of eq. (3.1) indicates that the second order quadrupole shift is zero at $\theta = 0$ or 90°. Indeed, at all orientations, the separation between the two

satellite lines is unaffected by the second order shift.

The relative amplitude of the $m \longleftrightarrow m-1$ transition is given by (BPP)

$$I(I+1) - m(m-1) \quad . \tag{3.3}$$

Thus for the case of ^{23}Na, we obtain 3:4:3 for the relative amplitude of a satellite, center line, and the other satellite respectively.

We now consider the linewidth of the various resonances. The theoretical parameter is the second moment M_2, but there is no unique relationship between this parameter and the linewidth. However, for the lineshapes commonly encountered in solids, the following relationship is a good approximation (Abragam, 1961):

$$\text{Linewidth} = 3\sqrt{M_2} \tag{3.4}$$

where the linewidth is the peak to peak width of the resonance derivative. According to Andrew et al (1962), the second moment of the center line for ^{23}Na in sodium nitrate is:

$$M_2 = [29.57 - 2.97 \cos 2\theta - 9.14 \cos 4\theta + \\ + 6.04(2 \sin 2\theta - \sin 4\theta)\cos 3\phi]\ 10^4 Hz^2 \quad . \tag{3.5}$$

In this case approximately 95% of the second moment is from "like" spins; the remaining 5% is caused by the ^{14}N nuclei. Thus, using eq. (2.25), we would expect the

second moment of a satellite line to be approximately 0.859 of that of the center line.

3.3 Orientation dependence of W_1 and W_2

The orientation dependence of W_1 and W_2 for a system of identical nuclei at sites possessing $\bar{3}$ symmetry is given by (Snyder and Hughes, 1971):

$$W_1 = \frac{e^2Q^2}{48}\Big\{(4M_{1111}+4M_{1313}-M_{3333})-(12M_{1313}-9M_{3333})\cos^2\theta$$
$$-(4M_{1111}-16M_{1313}+8M_{3333})\cos^4\theta$$
$$-16(M^*_{1113}\cos 3\phi + M^*_{1123}\sin 3\phi)\sin^3\theta\cos\theta\Big\} \quad (3.6)$$

$$W_2 = \frac{e^2Q^2}{48}\Big\{(M_{1111}+4M_{1313}+2M_{3333})+(6M_{1111}-6M_{3333})\cos^2\theta$$
$$+(M_{1111}-4M_{1313}+2M_{3333})\cos^4\theta$$
$$+4(M^*_{1113}\cos 3\phi + M^*_{1123}\sin 3\phi)\sin^3\theta\cos\theta\Big\}. \quad (3.7)$$

where the z axis coincides with the three-fold axis and the x and y axes are arbitrary. If the x and y axes are rotated, the components M^*_{1113} and M^*_{1123} assume different values but the quantity $(M^*_{1113}\cos 3\phi + M^*_{1123}\sin 3\phi)$ remains unchanged. The other components M_{1111}, M_{1313} and M_{3333} are unchanged by this transformation. It is convenient to choose a coordinate system

in which M^*_{1123} is zero; this means that the x axis coincides with a principal axis of the M tensor. However, it is impossible to simultaneously satisfy this condition for ^{23}Na in $NaNO_3$ on account of the different environments at the A and B sites. The principal axes for these two sites are symmetrically disposed relative to the intersection of a glide plane with the x-y plane. This is illustrated in Fig. 3.2 which shows just the nearest neighbour oxygen atoms. If we suppose that these atoms vibrate isotropically, then from symmetry considerations one would expect x_A, y_A and x_B, y_B to be the x and y principal axes of the M tensor which characterizes each site. Taking into account more remote neighbours, x_A, y_A and x_B, y_B are no longer in general the principal axes. However, owing to the short range of the quadrupolar spin-lattice interaction (see, for example, Appendix II) the nearest neighbour model is likely to be a good approximation: for want of evidence to the contrary, we assume that the principal axes of the local M tensor do indeed coincide with x_A, y_A and x_B, y_B respectively. To make full use of the crystal symmetry, we choose the x axis of our coordinate system to coincide with the intersection of a glide plane with the x-y plane. Thus, referred to this coordinate system, the relaxation probabilities for site A will be given by eqs. (3.6) and (3.7) if we

make the substitution:

$$(M^*_{1113} \cos 3\phi + M^*_{1123} \sin 3\phi) \longrightarrow M^*_{1113} \cos 3(\phi-\phi_o) \tag{3.8}$$

where ϕ_o is the angle between the x_A and x axes as shown in Fig. 3.2. For site B, eqs. (3.6) and (3.7) are modified as follows:

$$(M^*_{1113} \cos 3\phi + M^*_{1123} \sin 3\phi) \longrightarrow M^*_{1113} \cos 3(\phi+\phi_o) \ . \tag{3.9}$$

The A and B nuclear spin systems will be strongly coupled by spin exchange interactions (Abragam and Proctor, 1958; Bloembergen et al, 1959; Andrew and Swanson, 1960) due to resonance overlap, since each spin system has the same static quadrupole splitting. Also, as the heat capacity of each system is identical, the observed relaxation probabilities will then be given by

$$W_1 = (W_{1A} + W_{1B})/2 \tag{3.10}$$

$$W_2 = (W_{2A} + W_{2B})/2 \ . \tag{3.11}$$

If we insert the individual relaxation probabilities into eqs. (3.10) and (3.11), we obtain

$$W_1 = \frac{e^2Q^2}{48}\Big\{(4M_{1111}+4M_{1313}-M_{3333}) - (12M_{1313}-9M_{3333})\cos^2\theta$$
$$- (4M_{1111}-16M_{1313}+8M_{3333})\cos^4\theta$$
$$- 16M_{1113} \cos 3\phi \sin^3\theta \cos\theta\Big\} \tag{3.12}$$

$$W_2 = \frac{e^2Q^2}{48}\Big\{(M_{1111}+4M_{1313}+2M_{3333}) - (6M_{1111}-6M_{3333})\cos^2\theta$$

$$+ (M_{1111}-4M_{1313}+2M_{3333})\cos^4\theta + 4M_{1113}\cos 3\phi \sin^3\theta\cos\theta\Big\} \tag{3.13}$$

where

$$M_{1113} = M^*_{1113}\cos 3\phi_o \,.$$

As discussed in section 2.5, the $M_{\alpha\beta\alpha'\beta'}$ in W_1 are identical to those in W_2 for multiphonon relaxation process. Thus the ratio W_2/W_1 can then be expressed as:

$$\frac{W_2}{W_1} = \frac{\left\{\begin{array}{l}(1+4M'_{1313}+2M'_{3333})+(6-6M'_{3333})\cos^2\theta \\ +(1-4M'_{1313}+2M'_{3333})\cos^4\theta+4M'_{1113}\cos 3\phi \sin^3\theta\cos\theta\end{array}\right\}}{\left\{\begin{array}{l}(4+4M'_{1313}-M'_{3333})-(12M'_{1313}-9M'_{3333})\cos^2\theta \\ -(4-16M'_{1313}+8M'_{3333})\cos^4\theta-16M'_{1113}\cos 3\phi \sin^3\theta\cos\theta\end{array}\right\}} \tag{3.15}$$

where

$$M'_{1313} = M_{1313}/M_{1111} \tag{3.16}$$

$$M'_{3333} = M_{3333}/M_{1111} \tag{3.17}$$

$$M'_{1113} = M_{1113}/M_{1111} \,. \tag{3.18}$$

If the quadrupole relaxation is caused by diffusing charges, for example, the $M_{\alpha\beta\alpha'\beta'}$ will not in general be equal in eqs. (3.12) and (3.13) (Snyder and Hughes, 1971). Thus, eq. (3.15) will not be valid in that case.

A numerical calculation of the normalized M tensor components M'_{1313}, M'_{3333} and M'_{1113} has been given by Reed (1970) and Hughes and Reed (1971) for a nearest neighbour point-charge model of sodium nitrate. The detailed expressions are somewhat lengthy and are therefore given in Appendix II.

3.4 Spin-lattice relaxation transitions

The ^{23}Na quadrupole coupling constant is sufficiently large that the three resonances are well resolved at most crystal orientations. For an accurate calculation of the relaxation behaviour of the ^{23}Na spin system, it is necessary to take into account the quadrupole shifts of the energy levels. However, for large magnetic fields, the second order quadrupole shifts are small compared with the first order shifts. Thus, we can write the resonance frequencies as

$$\nu_+ = \nu_o(1 + \delta) \tag{3.20}$$

$$\nu_c = \nu_o \tag{3.21}$$

$$\nu_- = \nu_o(1 - \delta) \quad . \tag{3.22}$$

Since $I = 3/2$ for ^{23}Na, the quadrupole relaxation probabilities are given by (see eqs. (2.31) and (2.32))

$$W_{\frac{3}{2}\rightarrow\frac{1}{2}} = W_{-\frac{1}{2}\rightarrow-\frac{3}{2}} = W_1 \tag{3.23}$$

$$W_{\frac{1}{2}\to-\frac{1}{2}} = 0 \qquad (3.24)$$

$$W_{\frac{3}{2}\to-\frac{1}{2}} = W_{\frac{1}{2}\to-\frac{3}{2}} = W_2 \ . \qquad (3.25)$$

However, for a population dynamics calculation, it is necessary to bear in mind that the upward and downward transition probabilities are not exactly equal, since they are related by the Boltzmann factor. We therefore choose to call the upward transition probabilities W_1 and W_2, and the corresponding downward probabilities $W_1(1 + \Delta \pm \delta)$ and $W_2(1+ 2\Delta \pm \delta)$ where

$$\Delta = h\nu_o/kT_L \ . \qquad (3.26)$$

These transitions are shown in Fig. 3.3.

In general, one may also expect some magnetic relaxation, due, for example, to paramagnetic impurities. The upward transition probability for this case is given by (Andrew and Swanson, 1960):

$$W_{m\to m-1} = W_3(I+m)(I-m+1) \qquad (3.27)$$

and the downward transition probability is obtained by multiplying eq. (3.27) by the appropriate Boltzmann factor. These transitions are also shown in Fig. 3.3.

If the resonances are not well resolved, additional transitions will occur due to the so-called spin-exchange interaction (Abragam and Proctor, 1958; Bloembergen et al, 1959; Andrew and Swanson, 1960).

Figure 3.3

The spin-lattice relaxation transitions for the case I = 3/2, where the quadrupole splitting is sufficient to prohibit spin-exchange transitions.

W_1
$W_1[1+\Delta(1+\beta)]$
W_2
$W_2[1+\Delta(2+\beta)]$
$3W_3$
$3W_3[1+\Delta(1+\beta)]$
$4W_3$
$4W_3(1+\Delta)$
W_1
$W_1[1+\Delta(1-\beta)]$
W_2
$W_2[1+\Delta(2-\beta)]$
$3W_3$
$3W_3[1+\Delta(1-\beta)]$

Since these transitions introduce an additional coupling between the energy levels, they make it more difficult to interpret spin-lattice relaxation measurements.

CHAPTER IV

EXPERIMENTAL METHODS FOR STUDYING THE QUADRUPOLE SPIN-LATTICE RELAXATION

4.1 Steady-state double resonance method for measuring W_2/W_1

It was first demonstrated by Pound (1950) that it is possible to distinguish between magnetic and quadrupole relaxation mechanisms by means of a double resonance experiment on a quadrupole-split spectrum. For the case I equals 3/2, Pound showed that if W_1 equals W_2, and W_3 equals zero, the population difference of a satellite (i.e. its amplitude) is increased by 50% when the center line is severely saturated. For the case where magnetic relaxation is dominant, Pound showed that saturating one resonance would cause no change in the others. Later, Abragam (1961) generalized the theory and showed that the satellite enhancement E is given by

$$E = (1 + 2x)/(1 + x) \qquad (4.1)$$

where x is W_2/W_1. Thus, a measurement of the satellite enhancement should provide a value of W_2/W_1. It is obviously essential that nuclei involved must be at sites of lower than cubic symmetry. It is also highly desirable that the sample should be a single crystal,

so as to prevent smearing of the satellites. Abragam showed that W_2/W_1 could also be obtained by severely saturating a satellite and measuring the amplitude of the center line or the other satellite, the enhancements being respectively equal to

$$E = (3 + 2x)/(2 + x) \tag{4.2}$$

and

$$E = 2/(2 + x) \ . \tag{4.3}$$

We now present a simple physical picture which the author has found useful in explaining the enhancement of the satellite when the center line is severely saturated. The spin-lattice relaxation transitions tend to keep the spin system at the lattice temperature, whereas an rf field applied on resonance tends to decrease the population difference of the two energy levels involved. When a large saturation field is applied to the center line, its population difference rapidly decays to a small value (zero in the case of complete saturation). It can be seen from Fig. 3.3 that the population difference of each satellite line must correspondingly increase rapidly to 1.5 n_o, where n_o is the equilibrium population difference in the absence of applied rf fields (in this discussion, we neglect the small correction factor δ). The W_1 mechanism will tend to reduce the satellite population

difference to n_o, whereas the W_2 mechanism will tend to increase it to $2n_o$. This last point can be seen by remembering that the W_2 mechanism couples levels separated by $\Delta m = \pm 2$ (see Fig. 3.3) and that the center line population difference is maintained at zero by the saturation field. Thus, the final equilibrium population difference of the satellite line depends upon the relative strength of W_2 and W_1. When W_2/W_1 is very much greater than unity, the population difference approaches $2n_o$, and if W_2/W_1 is very much less than unity the population difference approaches n_o; these values can be compared with the predictions of eq. (4.1).

To obtain accurate W_2/W_1 values from enhancement measurements, the observing power of the spectrometer must not significantly perturb the spin system. The effect of a finite observing power is to make W_1 "less effective". Thus, the measured enhancement will be larger than the true value. Theoretical expressions for the enhancement in terms of W_2/W_1 were obtained by Hughes (1966) who also showed that the perturbing effect of a small observing power could be allowed for by a simple linear extrapolation to zero observing power. Reed (1970) showed experimentally that the enhancement did, indeed, vary linearly with observing power over quite an extended range for the ^{23}Na spin system in sodium nitrate.

The method for calculating the enhancement (Pound, 1950; Abragam, 1961; Hughes, 1966; Reed, 1970) consists in applying the principle of detailed balancing to the spin system, in order to obtain rate equations for the energy level populations. We shall not give the details of the steps but instead quote the steady state enhancement expressions given by Reed (1970).

The first case (Case I) is where the high frequency satellite is observed with spectrometer power P_{obs} and the center line is completely saturated: the enhancement is given by

$$E_I = \frac{(1+2x)}{(1+x)}\left[1 - \frac{\delta x}{(1+2x)} - \frac{3xy}{(1+x)(1+2x)} + \frac{3x\,P_{obs}}{2(1+x)}\right] \qquad (4.4)$$

where y is W_3/W_1, the normalized magnetic spin-lattice transition probability.

Case II is where the low frequency satellite is observed and the center line is completely saturated. In this case, the enhancement is

$$E_{II} = \frac{(1+2x)}{(1+x)}\left[1 + \frac{\delta x}{(1+2x)} - \frac{3xy}{(1+x)(1+2x)} + \frac{3x\,P_{obs}}{2(1+x)}\right] . \qquad (4.5)$$

Case III is where the center line is observed and the high frequency satellite is completely saturated. It is found that:

$$E_{III} = \frac{(3+2x)}{(2+x)}\left[1 + \frac{\delta(1+x)}{(3+2x)} - \frac{y(4+8x+7x^2)}{x(2+x)(3+2x)} + \frac{2(1+x)P_{obs}}{(2+x)}\right] . \qquad (4.6)$$

Case IV is where the center line is observed and the low frequency satellite is completely saturated. Here one finds that:

$$E_{IV} = \frac{(3+2x)}{(2+x)}\left(1 - \frac{\delta(1+x)}{(3+2x)} - \frac{y(4+8x+7x^2)}{x(2+x)(3+2x)} + \frac{2(1+x)P_{obs}}{(2+x)}\right). \quad (4.7)$$

The expressions for E_I to E_{IV} are valid for any value of x, but y, δ and P_{obs} are small correction factors and, thus, must be much less than unity. These expressions also assume that the appropriate resonance is completely saturated. This obviously cannot be achieved with a finite saturation field. Thus, we should correct the enhancement values to take into account the incomplete saturation. When δ, P_{obs} and y are equal to zero, the enhancement as a function of saturation power P_{sat} is given by:

$$E_{I,II} = \frac{1 + 2P_{sat}[(1+2x)/x]}{1 + 2P_{sat}[(1+x)/x]} \quad (4.8)$$

for Cases I and II. The expression for Cases III and IV is similarly given by:

$$E_{III,IV} = \frac{1 + 2P_{sat}[(3+2x)/x]}{1 + 2P_{sat}[(2+x)/x]} \quad . \quad (4.9)$$

The validity of the equations (4.8) and (4.9) was confirmed by Reed (1970). Thus, they can be used to make small corrections to the enhancement for the fact that the saturation power is not infinite.

Since the expressions (4.4) to (4.7) contain two unknown quantities, x and y (δ can easily be obtained from the satellite splitting), it is necessary to make two independent enhancement measurements. From the form of the equations, it can be seen that one must be either Case I or II, whereas the other must be Case III or IV. It is indeed fortunate that y enters differently in eqs. (4.4) and (4.5) than it does in eqs. (4.6) and (4.7); it would otherwise be impossible to determine x and y separately.

4.2 Transient double resonance method for measuring W_1

The steady state enhancement experiment just described gives only the ratio W_2/W_1. However, it is also useful to know the magnitude of W_1 or W_2 separately. The theoretical expressions (eqs. (3.12) and (3.13)) give the orientation dependence of these quantities, and it is therefore only necessary to determine W_1 or W_2 at one crystal orientation.

In principle it is possible to obtain W_1 from a steady state progressive saturation experiment (Hughes, 1966). However, the accuracy of such an experiment is very limited and a direct measurement of the time dependence of the spin system is more fruitful. This may be achieved by producing a non-equilibrium state of the spin system and observing its recovery.

Expressions for the transient behaviour of the spin system have been given by Niemelä (1968) for the approximation $\delta, P_{obs} = 0$. The transients are in general multi-exponential functions of time, and the task of determining the individual decay constants from experimentally obtained data is one of considerable complexity (Smith and Cohn-Sfetcu, 1973). However, using the expressions given by Niemelä (1968), it can be shown that the recovery of a satellite line after removal of the saturation power from the center line should be of the form:

$$A + B \exp -\lambda t \quad . \tag{4.10}$$

We carried out a detailed calculation of this case, taking into account first order δ and P_{obs} corrections but assuming that y is negligible. The population difference n_+ corresponding to the high frequency satellite has the following time dependence:

$$\begin{aligned} n_+ = {} & n_o(1+\delta)\left(1 - \frac{3(2+x)P_{obs}}{2(1+x)}\right) \\ & + n_o\left(\frac{x}{(1+x)} - \frac{3(x^2+x-1)P_{obs}}{2(1+x)^2}\right)\exp\{-(2W_1+3P_{obs}W_1)t\} \\ & + n_o\left(\frac{3(2x+1)P_{obs}}{2(1+x)^2}\right)\exp\{-(2W_1+2W_2+3P_{obs}W_1)t\} \quad . \end{aligned} \tag{4.11}$$

We note that there are now two exponential terms rather than one. However, the amplitude of the second exponential is proportional to P_{obs} and is therefore small,

provided one uses a low observing power. We also note that the decay constant of the dominant exponential is a linear function of P_{obs}. Thus, by measuring the decay constant as a function of P_{obs}, one should be able to determine W_1 by use of a linear extrapolation to P_{obs} equals zero. The effect of magnetic relaxation was taken into account for the case $P_{obs} = 0$. It was found that the decay constant of the dominant exponential is equal to:

$$W_1\left(1+ x + 7y + \sqrt{(1-x+5y)^2 + 4y(x-1)}\right) \qquad (4.12)$$

rather than $2W_1$ as before.

Thus, we see that W_1 can be measured by monitoring the recovery of the satellite amplitude after removing the saturating power from the center line. The decay constant is then plotted as a function of spectrometer power and the intercept is equated to expression (4.12).

It might be thought that W_1 could also be obtained from the transient behaviour of a satellite when the center line is first saturated. We shall now describe why this is not practical. The satellite population difference has the following time dependence:

$$n_+ = n_o\left(\frac{1+2x}{1+x}\right) + n_o\left(\frac{1-x}{2(1+x)}\right)\exp\{-(2+x)W_1 t\}$$

$$- \frac{n_o}{2}\exp\{-6P_{sat}W_1 t\} \quad . \qquad (4.13)$$

The last term in eq. (4.13) represents the rapid rise to 1.5 n_o described in section 4.1. Observation of the time dependent behaviour corresponding to the second term would give the value of $(2+x)W_1$. However, the amplitude of this term will be small unless x is very different from unity.

CHAPTER V

APPARATUS AND EXPERIMENTAL DETAILS

5.1 Measurement of the NMR enhancement

The resonance enhancement E is determined by measuring, as a function of spectrometer observing power P_{obs}, the increase in amplitude of one component of the three-line spectrum when another component is severely saturated. The perturbing effect of the observing power is accounted for by a linear extrapolation procedure of the E-P_{obs} curve to $P_{obs} = 0$ (Hughes, 1966; Reed, 1970).

For a continuous wave experiment, the experimental constraints on the spectrometer are, firstly, it should be variable frequency-fixed field rather than vice versa, since a variable field implies that the saturation frequency would have to track the resonance frequency. Secondly, it should be a single coil type, because of the need for an orthogonal coil to provide the saturation field. Thirdly, the spectrometer should operate at low power levels such that the transition rate in the spin system caused by the spectrometer is small compared with the spin-lattice relaxation rate.

The first constraint implies that Rollin (1946) and bridge spectrometers (BPP) are unsuitable, while the second constraint rules out the crossed-coil variety

(Bloch, Hansen and Packard, 1946). The marginal (Watkins and Pound, 1951) and Robinson (1959) self-oscillating spectrometers satisfy the three constraints. The Robinson type was chosen on account of its stable and reliable operation at the low power levels required. Moreover, it responds essentially to only the absorption signal (Hughes and Smith, 1971).

Reed (1970) measured the peak-to-peak amplitude of the resonance derivative by conventional lock-in detection* and sinusoidal field modulation in conjunction with a linear frequency sweep through the resonance. Reed's method is inefficient, since only a small fraction of the time is spent near the resonance extrema. While this disadvantage may be overcome by measuring the resonance amplitude only at an extremum, there remains the problem of maintaining the appropriate spectrometer frequency.

An alternative method is to use two lock-in detectors, one operating at the modulation frequency ω_m to lock the spectrometer onto the resonance, the other operating at $2\omega_m$ to measure the resonance amplitude. To maintain the spectrometer frequency, the error signal should be zero at the desired locking point and should

---

* Lock-in detectors are also known as phase-sensitive detectors, correlators or synchronous demodulators.

also be an odd (preferably linear) function of frequency deviation. These conditions are fulfilled by the output of the ω_m lock-in detector at the center of symmetrical resonances, for all modulation amplitudes. For good signal-to-noise ratio, the spectrometer frequency should be chosen to give a maximum output from the $2\omega_m$ lock-in detector. This condition is again fulfilled at the resonance center. In fact, the resonance center is the only position having all the desired properties and still allowing freedom to optimize the modulation amplitude.

In the limit of small modulation amplitudes the ω_m and $2\omega_m$ lock-in detector signals are proportional to the first and second derivatives respectively of the lineshape (Wilson, 1963); these are shown for a Gaussian lineshape in Fig. 5.1.

Most of the resonance amplitude values reported in this thesis were obtained using this arrangement in which the $2\omega_m$ lock-in detector output was measured while the ω_m lock-in detector maintained the spectrometer frequency at the resonance center. The enhancement values are equal to the ratio of the resonance amplitudes in the presence and absence of the saturation power. The error due to any dc offset in the circuitry following the lock-in detector was eliminated by periodically reversing the phase of the $2\omega_m$ reference signal.

Figure 5.1

A - Gaussian lineshape.

B - First derivative of the Gaussian lineshape.

C - Second derivative of the Gaussian lineshape.

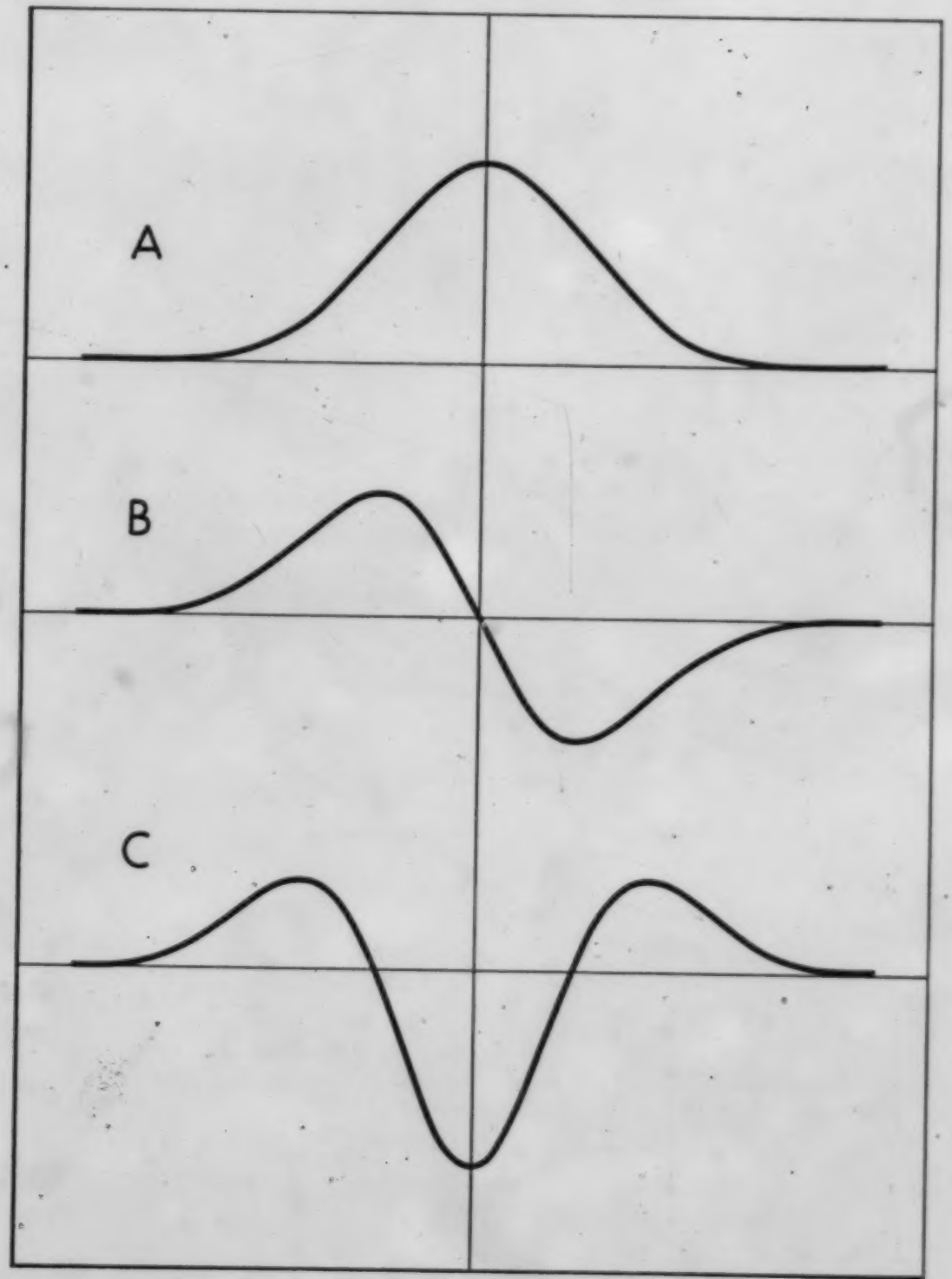
A
B
C

The measurement procedure is illustrated in Fig. 5.2. This ten-minute"saturation-cycle"was repeated until the desired precision in E was obtained. The enhancement was measured at a number of different values of P_{obs} so that the value of E at P_{obs} equals zero could be determined by the linear extrapolation procedure.

The small correction factor to take into account the non-infinite saturation power was determined by the following procedure. We measured the enhancement for three or four values of saturation power (at a low value of P_{obs}) and the value of E at infinite power was determined using equation (4.8). This value was typically 0.15% greater than the value obtained at the finite saturation power used in the previous measurements. We then used this to correct the extrapolated value of E at $P_{obs} = 0$.

For most of this work, the Robinson spectrometer was locked to the high frequency satellite and the saturation power was applied to the center line. Approximately forty-eight to sixty hours of data were collected at each crystal orientation in order to attain the desired precision in E. Thus, the advantage of a mini-computer controlled system operating twenty-four hours per day is obvious.

To obtain accurate and reliable values of the enhancement, we require the spectrometer frequency to

Figure 5.2

Output of the $2\omega_m$ lock-in detector for one complete "saturation cycle". The bandwidth of the low-pass filter is 1 Hz.

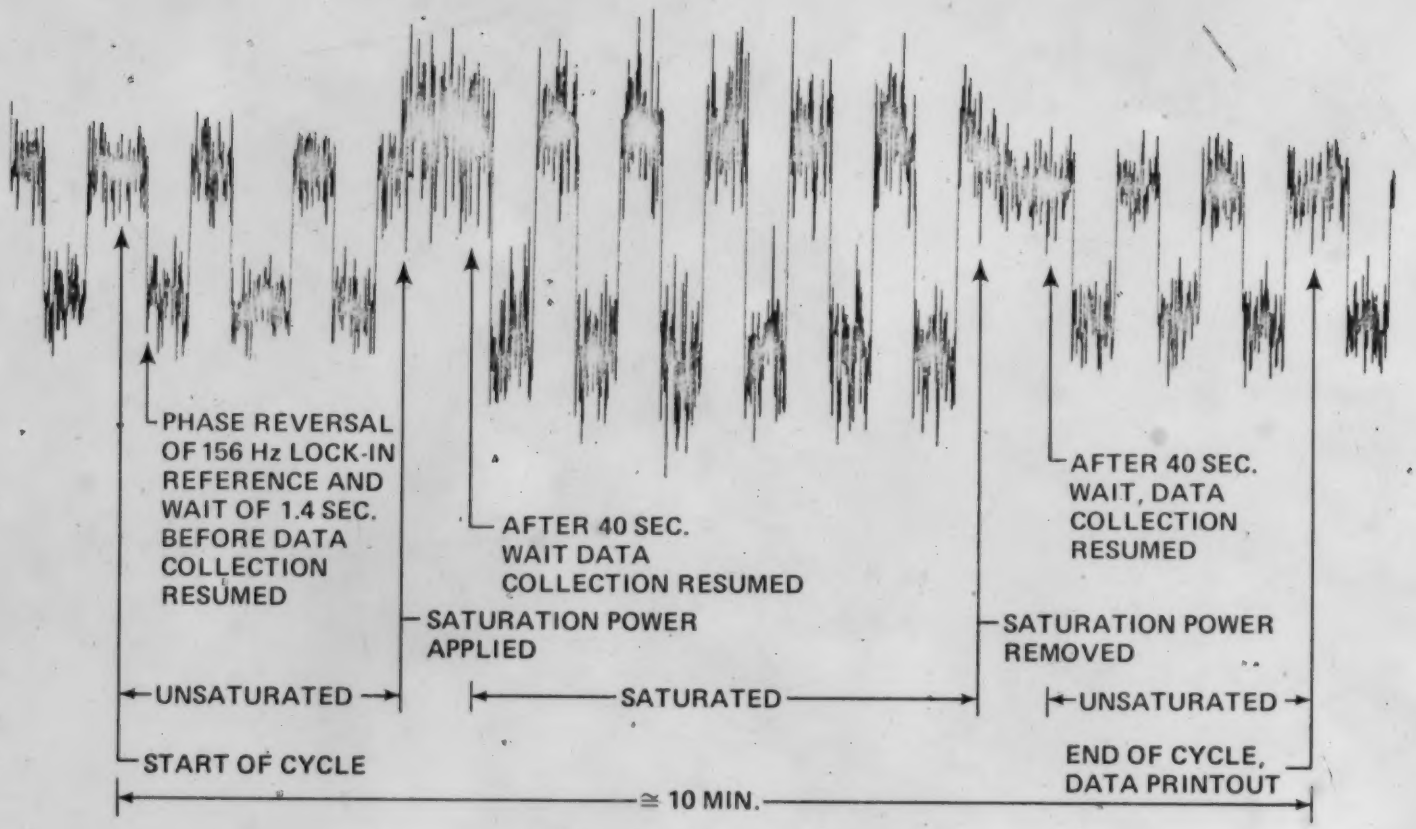
PHASE REVERSAL OF 156 Hz LOCK-IN REFERENCE AND WAIT OF 1.4 SEC. BEFORE DATA COLLECTION RESUMED
AFTER 40 SEC. WAIT DATA COLLECTION RESUMED
AFTER 40 SEC. WAIT, DATA COLLECTION RESUMED
SATURATION POWER APPLIED
SATURATION POWER REMOVED
UNSATURATED
SATURATED
UNSATURATED
START OF CYCLE
END OF CYCLE, DATA PRINTOUT
≅ 10 MIN.

be locked, the magnetic field to remain constant and the spectrometer sensitivity to NMR to be unchanged throughout the saturation cycle. A large amount of ancillary equipment was required to achieve these goals, as will be described in the sections that follow.

5.2 Description of the apparatus

5.2.1 Block diagram

The block diagram of the system is shown in Fig. 5.3. Excluding commercial equipment, the system contains approximately 600 integrated circuits, both digital and analogue, plus numerous discrete components, semiconductor devices and thermionic valves. The individual circuit diagrams of the blocks will therefore not be given. Instead, we shall describe their function, operation and important features.

Most of the digital and analogue circuitry was assembled on 4½" × 6½" circuit cards which are plugged into multiple-pin edge connectors, thereby assuring ease of access for maintenance. The construction and development of the system extended over a period in excess of three years and included a considerable amount of redesign to obtain the final working version.

The central feature of the system is the (System) Buss. Its function is to enable the various devices to

Figure 5.3

Block diagram of the minicomputer-controlled double resonance spectrometer system. The arrows indicate the direction of information or signal flow.

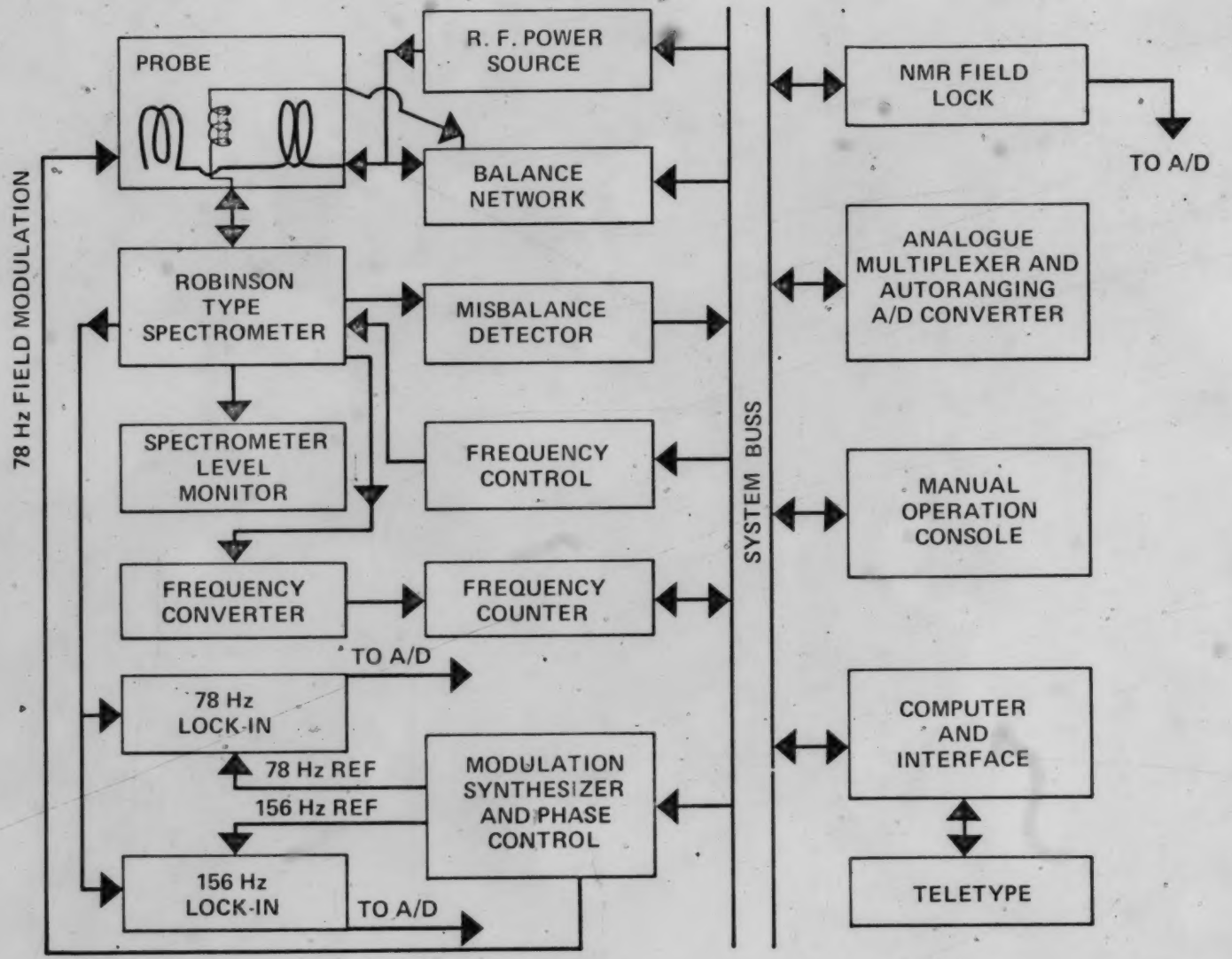
PROBE
R. F. POWER SOURCE
BALANCE NETWORK
ROBINSON TYPE SPECTROMETER
MISBALANCE DETECTOR
SPECTROMETER LEVEL MONITOR
FREQUENCY CONTROL
FREQUENCY CONVERTER
FREQUENCY COUNTER
TO A/D
78 Hz LOCK-IN
78 Hz REF
156 Hz REF
MODULATION SYNTHESIZER AND PHASE CONTROL
156 Hz LOCK-IN
TO A/D
78 Hz FIELD MODULATION
SYSTEM BUSS
NMR FIELD LOCK
TO A/D
ANALOGUE MULTIPLEXER AND AUTORANGING A/D CONVERTER
MANUAL OPERATION CONSOLE
COMPUTER AND INTERFACE
TELETYPE

communicate data and commands to each other. It consists of 16 data lines, 16 monitor lines, as well as several address and strobe lines. Each device is connected either directly or indirectly to the Buss. The interface is a bi-directional device enabling information to be transmitted between the Buss and the computer. As an example of the operation of the system, we shall consider one method of frequency counter control. The computer sends a command on the address and strobe lines to the frequency counter to start counting. One second later, when the frequency counter has completed its measurement, an interrupt signal is sent to the computer, which may or may not act upon it. If it does, it may command the frequency counter to transfer the digital representation of the measured frequency onto the monitor lines and thus into the computer.

The blocks are described in detail in sections 5.2.2 to 5.2.17. Meanwhile, we describe briefly their functional relationships.

The $NaNO_3$ sample is positioned within the spectrometer coil, which in turn is located in the aluminium probe. The ^{23}Na NMR signal is detected by the spectrometer in conjunction with the ω_m and $2\omega_m$ lock-in detectors. The "modulation synthesizer and phase control" provides the signal feeding the modulation coils, and

the reference signals for the lock-in detectors. The phase of the reference signals relative to the modulation signal can be controlled by the system or can be adjusted manually.

Each lock-in detector output is fed to the analogue multiplexer, and then digitized by the analogue to digital (A/D) converter before being coupled to the Buss.

The spectrometer frequency is controlled in the following way: the frequency converter and counter together provide a digital representation of the spectrometer frequency. This information is compared with the "correct frequency" stored in the computer, and any correction is fed to the frequency control D/A converter. The analogue output biases a variable capacitance diode in the oscillator tuned circuit.

The rf power source drives a pair of coils within the probe which provide the saturation field. Although these coils are nominally orthogonal to the spectrometer coil, some of the saturation signal unavoidably leaks into the spectrometer. We have shown theoretically (Hughes et al, 1973) that the sensitivity to NMR of a Robinson spectrometer should be unaffected by a small leakage. The sensitivity of our spectrometer, however, was found experimentally to vary quadratically with the injection voltage; this

is attributed to non-ideality of the spectrometer. In order to overcome this problem, the leakage is largely eliminated by the flux balance network, which is based on the design of Hughes and Reed (1970). The deviation from perfect balance is monitored by the misbalance detector which, on command, can inform the computer of its magnitude. This information is then used by the computer to readjust the balance network.

The NMR field-lock spectrometer maintains the magnetic field in the magnet gap at a predetermined value throughout the course of the experiment.

The manual operation console enables the operator to interact directly with the system, thus by-passing the computer, which is the real-time control center of the system. The teletype provides a means of entering programs into the computer as well as printing the experimental results.

5.2.2 Probe

This consists of an aluminium body with nylon inserts to provide mechanical support for the spectrometer and saturation coils. These were wound of silver wire rather than copper, since the ^{63}Cu NMR signal occurs close to the ^{23}Na resonance. To increase the "NMR filling factor" the spectrometer coil was glued

to the inside rather than the outside of a nylon holder. The position of the connecting leads was adjusted so as to minimize the net coupling with the saturation coils. The size and inductance of the latter were chosen to maximize the saturation field produced at the sample. The spectrometer, probe and balance network were interconnected by triaxial cable, as shown in Fig. 5.4, so that the rf return currents would not flow in the outer shield.

The modulation coils consisted of a hundred turns of copper wire, which were wound on nylon formers outside the aluminium probe. The leads to the modulation coils were also kept outside the probe body to minimize coupling with the sensitive rf circuitry.

The sample was mounted in a nylon holder which enabled the crystal to be rotated about two mutually perpendicular axes, as will be described in section 5.8.

5.2.3 Robinson spectrometer

A Robinson type NMR spectrometer (Robinson, 1959) consists of a high-Q parallel-tuned L-C circuit followed by a low-noise rf amplifier, limiter and feedback network to sustain oscillations. Changes in oscillation level caused by NMR absorption are monitored by a

Figure 5.4

Schematic diagram of the wiring associated with the NMR probe and the Balance Network.

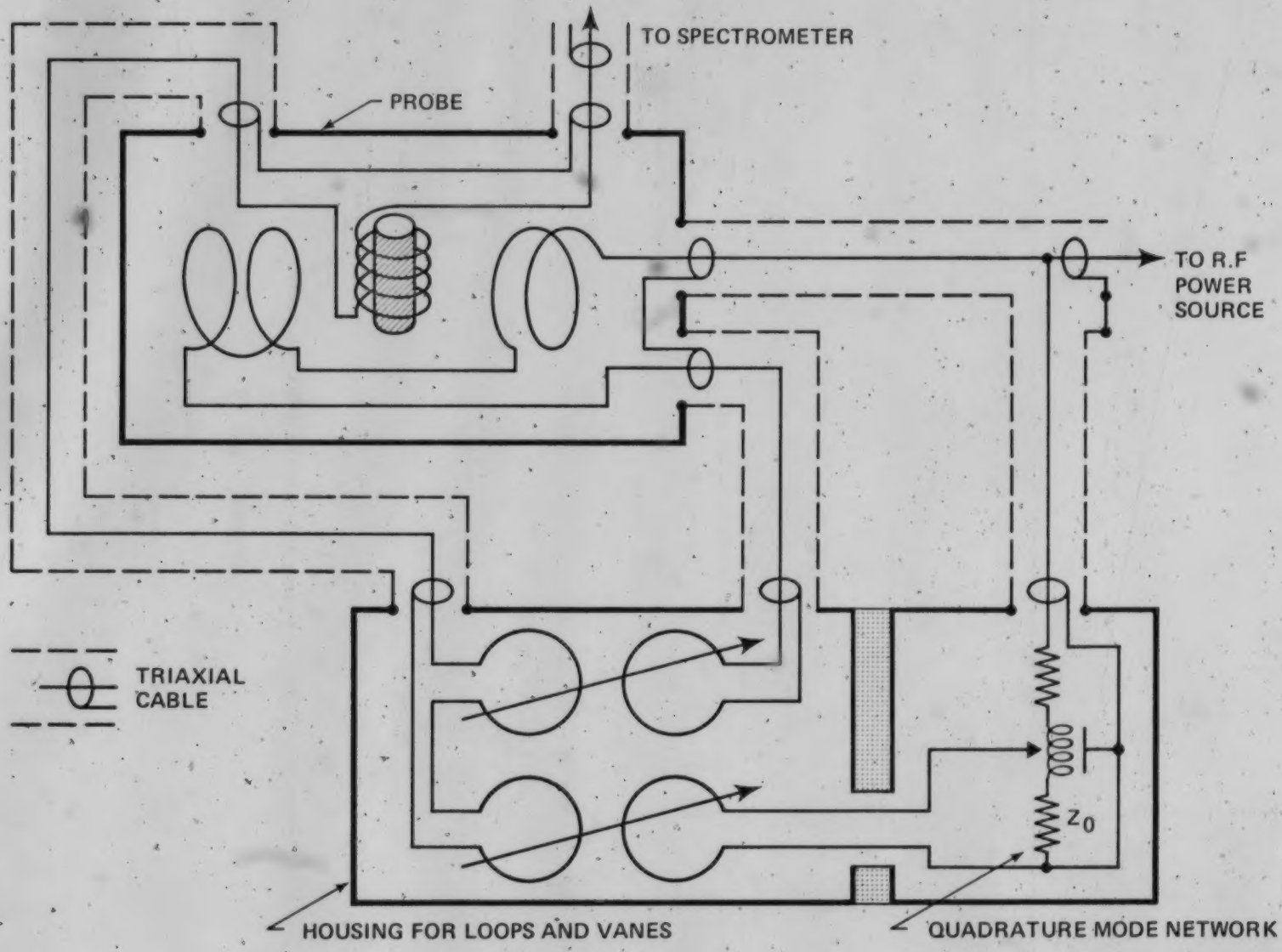
TO SPECTROMETER
PROBE
TO R.F
POWER
SOURCE
TRIAXIAL
CABLE
Z_0
HOUSING FOR LOOPS AND VANES
QUADRATURE MODE NETWORK

diode detector followed by a low noise audio frequency amplifier.

Our design is a modification of that given by Howling (1966) and the essential features are shown in Fig. 5.5. Limiting is achieved in two stages using Schottky diodes. These were used because of their low noise, low capacitance, and sharp "turn-on" characteristics. Five switchable resistive dividers enabled the oscillation level to be set over the range 5 to 50 mV RMS. The feedback network comprises ten 20 KΩ resistors connected in series and located in the center of a large metal box. This arrangement provides a low-loss feedback path which is essentially resistive.

Ground loops were avoided by having only one dc connection between the system and the spectrometer, this being the ground connection to the variable capacitance diode. Other dc connections were avoided by using transformer coupling for the audio output and optical couplers for the misbalance detector and frequency converter outputs.

A major problem was the spurious mixing of rf and audio frequencies. We note that if the oscillation signal is modulated at ω_m or $2\omega_m$, these will appear as fake outputs at the ω_m and $2\omega_m$ lock-in detectors. The latter is particularly troublesome,

Figure 5.5

Block diagram showing the essential features of the Robinson spectrometer used to measure NMR amplitudes. The sample is situated within the inductor in (1).

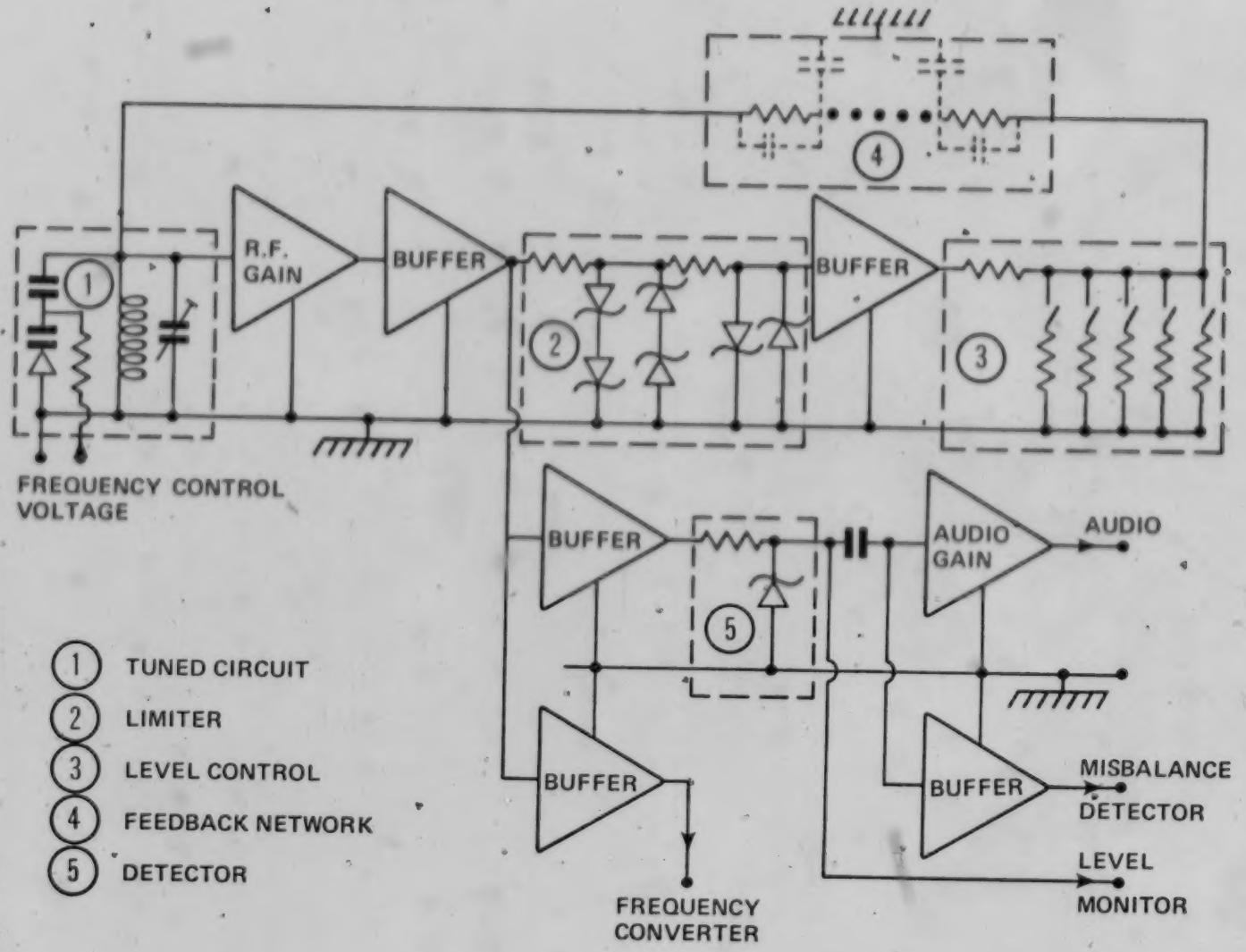
R.F. GAIN
BUFFER
BUFFER
BUFFER
BUFFER
BUFFER
AUDIO GAIN
AUDIO
MISBALANCE DETECTOR
LEVEL MONITOR
FREQUENCY CONTROL VOLTAGE
FREQUENCY CONVERTER
1 TUNED CIRCUIT
2 LIMITER
3 LEVEL CONTROL
4 FEEDBACK NETWORK
5 DETECTOR

since it introduces a systematic error in the determination of enhancement values, as discussed in section 5.4.3. These effects were ameliorated by extensive rf filtering and buffering of all connections to the spectrometer.

Some time was spent modifying the spectrometer so that adequate NMR signal-to-noise ratios were obtained. In particular, the gain of the rf amplifiers was made larger than one hundred so that noise originating in the detector and audio stages is unimportant. The signal-to-noise ratio is proportional to the square root of the in-situ Q factor of the sample tuned circuit. We found that this Q-factor can be significantly reduced by seemingly innocuous components such as the 50 Ω grid-stopper used by Howling (1966) in the input stage of his spectrometer. The effective NMR filling factor was improved by minimizing the inductance of the connection leads to the sample coil. The triaxial shielding arrangement mentioned in section 5.2.2 also served to reduce the sensitivity of the spectrometer to external interference.

5.2.4 Spectrometer level monitor

A "three-and-a-half-digit" dc voltmeter measures the spectrometer detector voltage, which in turn is related to the spectrometer level. This voltmeter was

calibrated in the following way: The Marconi oscillator (see section 5.2.5) was connected across the spectrometer tuned circuit and the voltmeter was read as a function of the Marconi oscillator output. Thus, the spectrometer level is the equivalent Marconi output which would give the observed detector level. Since the characteristics of the spectrometer may be frequency dependent, this calibration procedure was performed every time a new crystal orientation was selected.

The output attenuator of the Marconi oscillator was in turn calibrated by a "true RMS thermal converter" which measures rf voltages to better than 1%.

5.2.5 The rf power source

Preliminary measurements using a Takeda-Riken Model 2150 frequency synthesizer showed that it was too noisy to use as the source of the saturation signal; this was because the balance condition of the balance network was frequency dependent. Thus, even though there may be no coupling between the saturation and spectrometer coils at the saturation frequency, this is not the case at other frequencies. In particular, noise generated by the saturation signal source near the spectrometer frequency will be coupled to the spectrometer. A Marconi TF2002 L-C signal generator was found to be sufficiently noise-free. However, it

lacked the required frequency stability. A Marconi TF2170B digital synchronizer was therefore used to lock the signal generator, thereby achieving a frequency stability of ±1 Hz. The Marconi output is then fed, via the system-controlled co-axial on/off switch to an E.N.I. Model 310L ten watt rf power amplifier. To provide electrical isolation, the logic signal to the switch is passed through an optical coupler. The power amplifier output is then fed to the saturation coils and the balance network.

5.2.6 Balance Network

Although the connection leads of the spectrometer coil within the probe were adjusted to minimize the coupling with the saturation coils, a non-zero leakage remained. This was found to be approximately orthogonal to the saturation voltage; we attribute this to the eddy currents induced in the aluminium probe case.

The flux balance network is based on a design of Hughes and Reed (1970), and operates by synthesizing a cancelling leakage from in-phase and quadrature mode signals, each of adjustable amplitude. All the leakage signals are coherent, since they are derived from the same rf power source. As shown in Fig. 5.4, injection signals are coupled to loops in the spectrometer circuit.

Reversible synchronous motors and a series of reduction gears rotate grounded aluminium vanes between the loops, thereby adjusting the amplitude of the couplings. The two modes were set precisely orthogonal to one another by adjustment of a variable delay line in the orthogonal mode circuitry. This arrangement gave two orthogonal modes with little interaction between them, thereby enabling the balance condition to be reached in a small number of steps.

Because of the imperfections in the spectrometer, mentioned in section 5.2.3, a net leakage of less than 1 part in 10^7 of the saturation voltage was required. This placed great demands on the stability of the balance network. Consequently, all loops, vanes and wiring were rigidly constructed to minimize microphonics. One major source of instability was Joule heating of the delay line. This was largely overcome by optimizing the coupling, thereby reducing the current flow through the delay line.

A 1 part in 10^7 correction to a mode corresponds to a vane rotation of only three minutes of arc. High quality bearings and anti-backlash gears were therefore used to ensure smooth and reliable rotation. Even so, backlash still remained a problem, but was solved at the software rather than the hardware level.

The sense and the duration of the rotation of each motor was controlled by a bank of relays, which in turn were activated by the system. Optical couplers between the system and the relays provided electrical isolation,and minimized interference effects.

5.2.7 Misbalance detector

Any residual saturation signal entering the spectrometer will be mixed with the spectrometer signals by the nonlinear elements, thus producing sum and difference frequencies. The latter component, which is less than 170 kHz in our experiment, is amplified, filtered, rectified and smoothed in the misbalance detector unit. To avoid the dc loop created by connecting the output of the misbalance detector directly to the analogue multiplexer, we used an ac method of coupling into the system. The slowly varying dc voltage modulates the pulse width of a 100 Hz square wave carrier, which is then passed to an optical coupler and hence to the system. This pulse train is used to gate a 10 kHz clock pulse. By counting the number of clock pulses per carrier cycle, we obtain a binary number representing the original dc voltage to an accuracy of 1%. An interrupt signal is sent to the computer whenever this number is greater than a predetermined reference number.

Previous work in this laboratory has shown (Hughes et al, 1973) that the precise relationship between the injection voltage and the change in spectrometer NMR sensitivity is a complicated function of spectrometer circuit parameters and the difference frequency. The misbalance detector was, therefore, calibrated by the following procedure. The balance network was misbalanced by trial and error until the NMR spectrometer sensitivity changed by 1%. Then, assuming a quadratic dependence of NMR sensitivity change on the injection voltage as found by Hughes et al (1973), the injection voltage was reduced to the level which would give a sensitivity change of 0.05%. The 1% sensitivity change was chosen to ensure the validity of the extrapolation. The output of the misbalance detector was noted and the experiment repeated as a function of difference frequency and spectrometer level, thus enabling the interrupt level to be set to a level such that the change in the NMR sensitivity is no more than 0.05%. The good signal-to-noise ratio of the ^{23}Na resonance from a sample of metallic sodium facilitated the calibration procedure. The computer program, written for the enhancement experiment on $NaNO_3$, was used without modification for the measurement of the change of NMR sensitivity.

5.2.8 Frequency converter

The frequency counter described in the next section consists of a series of divide-by-two stages. The outputs of these stages will therefore, in general, have a component at the spectrometer frequency. Moreover, the amplitude of this component depends on whether or not the frequency counter is actually counting. Any radiation from the frequency counter entering the spectrometer will therefore appear as an additional and variable feedback path.

To avoid this problem, the spectrometer frequency was heterodyned with a crystal-controlled oscillator, whose frequency was 9.76 MHz. This local oscillator frequency was selected to ensure that no harmonic of the intermediate frequency (approximately 2.2 MHz) could ever coincide with the spectrometer frequency over its operating range. The output of the frequency converter was fed to the frequency counter via an optical coupler providing electrical isolation.

To reduce radiation at the spectrometer frequency, the frequency converter was mounted in a steel box near the spectrometer, so reducing lead lengths; this unit also had multistage rf filtering on the dc supply lines and in the ac power line to it.

5.2.9 Frequency counter

The system-controlled frequency counter has a resolution of 1 Hz and a count time of one second derived from a stable 1 MHz crystal oscillator ($\sqrt{RMS}$ Model M76BR). After the counter has completed its measurement, it may be restarted within 1 millisecond, unlike most commercial counters in which a wait of one second would be required. The count number is in binary format since this is a convenient representation for the computer to manipulate. (The binary coded decimal B.C.D. format is convenient for a visual display but not so convenient for computer manipulation.) The 22 bit binary equivalent of the intermediate frequency is too long to be handled by the computer software, therefore only the least significant 12 bits are used. The resulting ambiguity in frequency is not a problem provided the spectrometer frequency changes are less than 11 bits/sec (2048 Hz/sec). In practice this condition is easily satisfied since the spectrometer instability is seldom in excess of 10 Hz/sec.

5.2.10 Frequency adjustment circuitry

In a semiconductor diode, the width of the depletion layer, and hence the capacitance, is a function of the bias; this property is utilized in variable

capacitance diodes. If such a device forms part of the spectrometer input tuned circuit, it provides an electrical means of frequency control. For this particular application, the output of a 12 bit D/A converter reverse biases the diode. The bit size corresponds to a frequency change of 2 Hz, giving a total range of just over 8 kHz. Since noise voltages applied to the variable capacitance diode frequency modulate the spectrometer, the control voltage was passed through a multistage 10 Hz low-pass filter, thereby reducing any spurious frequency modulation, at ω_m and $2\omega_m$ in particular.

Data from the computer is fed into the frequency control device via the data lines, and then stored in 12 data latches. Their outputs are connected to the D/A converter and their contents may be ascertained by the monitor lines.

5.2.11 The ω_m and $2\omega_m$ lock-in detectors

Lock-in detectors are commonly used in various branches of spectroscopy where the phenomenon under investigation can be modulated by a periodic signal. In general, the spectrometer output can then be written as

$$V_s = \sum_n A_n \cos(n\omega t + \phi_n) \qquad (5.1)$$

where ω is the modulation frequency. If V_s is multiplied by a reference signal

$$V_r = \sum_n B_n \cos(n\omega t + \psi_n) \qquad (5.2)$$

of the same periodicity, the dc component of the resulting signal is

$$\frac{1}{2} \sum_n A_n B_n \cos(\phi_n - \psi_n) \qquad (5.3)$$

This process is essentially the determination of the cross-correlation coefficient of V_s and V_r. If all components of V_s except the m'th are rejected by suitable filtering before the multiplication stage, the dc component is

$$\frac{1}{2} A_m B_m \cos(\phi_m - \psi_m) \qquad (5.4)$$

This has a maximum when $\phi_m - \psi_m = 0$ or 180°. Moreover, if B_m is constant, this output is a measure of the amplitude of the m'th harmonic of V_s. We note that for the latter case, the shape of the reference signal is unimportant, as long as the amplitude of the m'th harmonic remains constant.

Our lock-in detectors operate on this principle, and the design has been described in some detail by Boyd (1975). Each detector consists of an input stage, a band-pass filter and amplifier, a correlator and a

CANADIAN THESES ON MICROFICHE

27740

THÈSES CANADIENNES SUR MICROFICHE

AUTHOR/AUTEUR

SPENCER, P.A.

TITLE/TITRE

^{23}Na QUADRUPOLE RELAXATION MEASUREMENTS...

post-correlator low-pass filter.

The choice of modulation frequency was governed by the following constraints. It should be high enough to avoid the "flicker noise" or 1/f noise region. However, it should be small compared with the NMR linewidth expressed in frequency units (Haworth and Richards, 1972). Also, frequencies near 60 Hz and 120 Hz should be avoided. Indeed, it is desirable that harmonics of the modulation frequency should not coincide with harmonics of the 60 Hz line voltage. For reasons of stability, the modulation and reference signals were derived from a (3 MHz) crystal oscillator. The precise modulation frequency was 78.125 Hz, this being obtained by digital frequency division of the 3 MHz signal.

The input stage is common to both lock-in detectors. The secondary of the input transformer provides a balanced output which is connected to a differential-input amplifier. This arrangement provides isolation and common mode rejection. The 78 Hz (ω_m) and 156 Hz ($2\omega_m$) signals are amplified and passed through a band pass filter, before being fed to the separate channels.

In order to avoid overloading the later stages of the lock-in detectors with wide-band noise plus 60 Hz or 120 Hz interference signals, each channel is

equipped with a band pass filter of bandwidth 10 Hz centered about 78 or 156 Hz. A fairly close approximation to a rectangular response in the frequency domain was obtained using multistage stagger-tuned active filters. Provision is made for the system to control the gain of the amplifiers.

In our correlators, the incoming signal is multiplied by a square wave at the reference frequency of 78 or 156 Hz. This is achieved by means of a digitally programmable amplifier the gain of which is plus one for the first half of the reference cycle and minus one for the second half.

Two-pole Tchebyscheff low-pass filters, the cut-off frequency of which can be controlled by the system, remove high frequency noise components from the correlator output; the output of the filter is then fed to the analogue multiplexer.

Diode shaping networks and band pass filters are used to convert the modulation signal to a sine wave. This is then applied to the modulation coils via an ac coupled current source. The ac coupling ensures that no dc currents bias the steady magnetic field, while the use of a current source rather than a voltage source provides a more stable field modulation amplitude and phase.

The phase of each reference signal relative to the modulation, is manually adjustable over a range of 150°. It can also be changed by exactly 90° and 180° by the system.

The ω_m and $2\omega_m$ correlators and the modulation source were constructed in a separate rf shielded box (called Superbox for reasons which will become clear later!), to prevent the mixing of the spectrometer and reference frequencies. This will be explained in more detail in section 5.4.3.

5.2.12 Analogue multiplexer and A/D converter

The various signal voltages to be measured are connected to the A/D converter via the analogue multiplexer, which has fifteen differential input channels, with provision for gain auto-ranging on nine of them. Digitally-programmable amplifiers form the basis of the multiplexer, so that any one of the input channels may be connected to the A/D converter on command from the system.

The A/D converter is an Analogic "three-and-one-half-digit" panel meter, model number 2532. The display gives a visual check on the operation of the equipment. For the A/D converter, a full-scale reading of ±2,000 counts corresponds to an input of ±8 V. The

analogue circuitry preceding the A/D converter can handle a voltage in excess of this, thus full use can be made of the converter's dynamic range.

On completion of a conversion from analogue to digital representation, the count number plus the multiplexer gain can be viewed by the operator or computer via the monitor lines. The computer has a software subroutine for converting this output into the floating-point number format recognized by the computer software.

5.2.13 Magnet and NMR field-lock

The magnetic field H_o of approximately 6700 G is produced by a box-section permanent magnet with 8" diameter pole caps and a 2" gap. The magnet is "overshimmed" such that there is a field minimum at the center of the pole gap and a maximum at a radius of 2". The best field homogeneity occurs in the latter region and is about 100 mG over a 1 cm^3 volume. To minimize vibration problems, the magnet is mounted on antivibration pads. Thermal stability is achieved by surrounding the magnet with 1" thick styrofoam. Tests show that the thermal time constant of the insulated magnet is approximately 34 hours.

The temperature coefficient of H_o was found to be -1.2 G/°C. Since we required a field stability of

a few tens of milligauss, it was necessary to stabilize H_o. This was achieved using a ^{7}Li NMR field-lock, which provided a current fed to a pair of field correction coils wound around the pole caps. The ^{7}Li resonance from an aqueous solution of LiCl was detected using a Rollin spectrometer (Rollin, 1946) employing 25 Hz field modulation and lock-in detection at the modulation frequency (see Fig. 5.6 for block diagram of the field-lock unit). The modulation signal and the reference signal for the lock-in detector were obtained by frequency division of a 1 MHz crystal-controlled signal. The lock-in detector is similar to the ω_m detector discussed in section 5.2.11. The 25 Hz modulation frequency of the Rollin spectrometer was chosen so as not to be harmonically related to the 78.125 Hz modulation frequency used in the Robinson spectrometer. The rf source for the Rollin spectrometer was a 11.1 MHz crystal-controlled oscillator of stability 1 part in 10^7/°C. The 11.1 MHz frequency was chosen so that the field correction would be both small, and always of the same sign so that a unipolar power supply could be used. In practice, the field correction was about -10 G.

The Rollin lock-in detector provides a suitable error signal in the region of the resonance center (cf. the discussion in section 5.1 of the ω_m and $2\omega_m$ lock-in detectors). Whenever this error signal is

Figure 5.6

The block diagram of the operation of the NMR Field-lock used to stabilize the magnetic field of the permanent magnet.

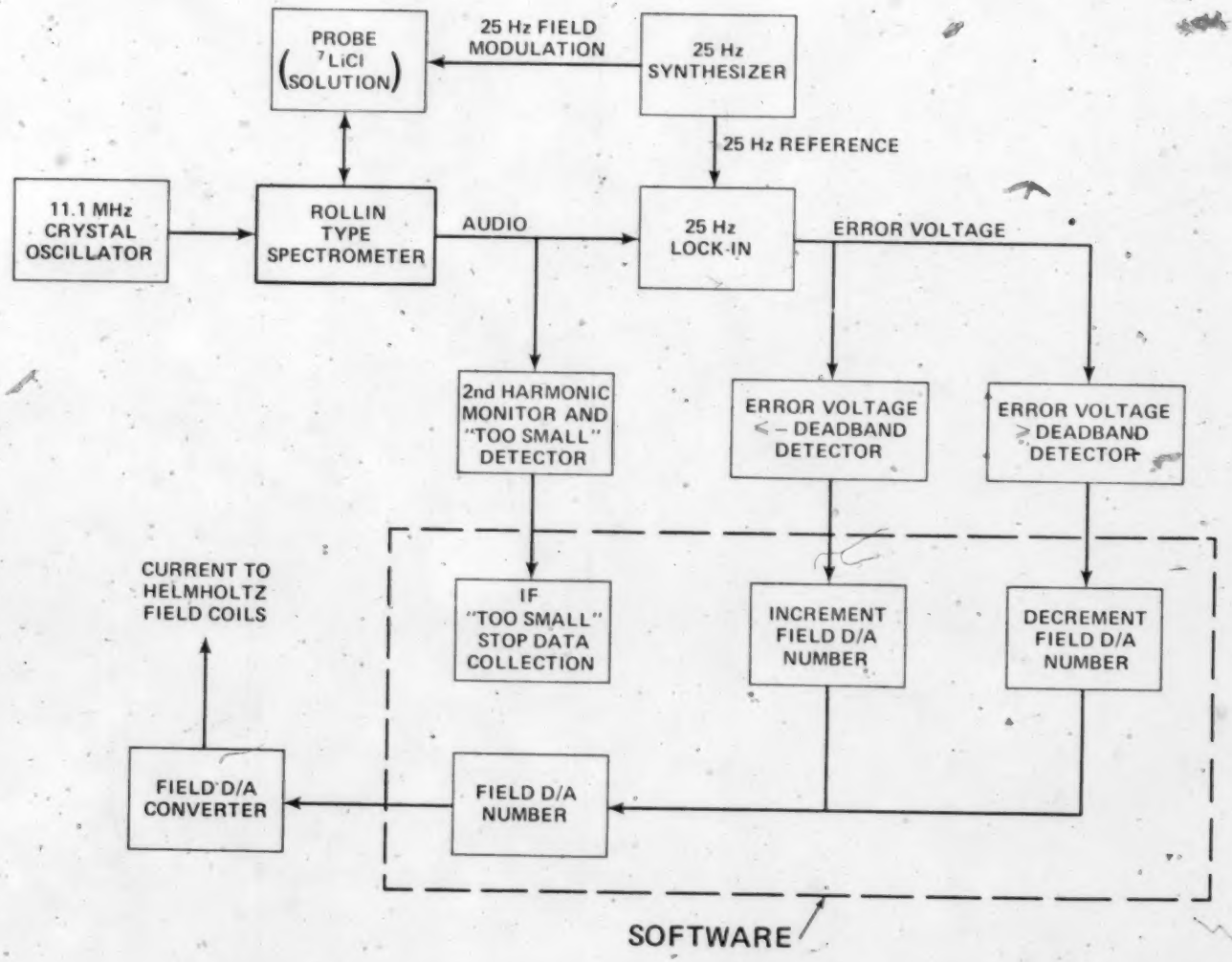
PROBE
(^{7}LiCl SOLUTION)
25 Hz FIELD MODULATION
25 Hz SYNTHESIZER
25 Hz REFERENCE
11.1 MHz CRYSTAL OSCILLATOR
ROLLIN TYPE SPECTROMETER
AUDIO
25 Hz LOCK-IN
ERROR VOLTAGE
2nd HARMONIC MONITOR AND "TOO SMALL" DETECTOR
ERROR VOLTAGE < – DEADBAND DETECTOR
ERROR VOLTAGE > DEADBAND DETECTOR
CURRENT TO HELMHOLTZ FIELD COILS
IF "TOO SMALL" STOP DATA COLLECTION
INCREMENT FIELD D/A NUMBER
DECREMENT FIELD D/A NUMBER
FIELD D/A CONVERTER
FIELD D/A NUMBER
SOFTWARE

larger than a predetermined level, an interrupt signal is sent to the computer. This can then change the current feeding the correction coils thereby reducing the error signal to zero. This current is controlled by a 12 bit D/A converter, the bit size corresponding to 1.83 mG. The noise in the spectrometer output corresponds to less than half a bit, hence H_o is stabilized to a few parts in 10^7.

The lock-in detector output is also zero far from the resonance condition! This possibility is detected by monitoring the output of a filter, tuned to the second harmonic of the modulation frequency. An interrupt is sent to the computer if the output is too small, thereby alerting the operator that the field stabilization unit is out of lock.

The control algorithm for the "Field-lock" is discussed in detail in section 5.3.6.

The "Field-lock" actually stabilizes the field at the LiCl sample, whereas what is really required is to stabilize the field at the $NaNO_3$ sample. This was achieved by positioning each sample on the median plane of the magnet gap and at the same distance from the gap center. For such a symmetrical arrangement, the correction field is the same at both sites. The samples were actually placed four inches apart, thereby ensuring that both were in the region of maximum field

homogeneity. If the changes in the field of the magnet are identical at each site, then H_o is also stabilized at the $NaNO_3$ sample. This was checked by changing the room temperature by 2°C and monitoring the magnetic field at the LiCl and $NaNO_3$ samples.

With the four-inch sample separation and the 40 mG modulation amplitude used for the field-lock, it was found that the 25 Hz fringe field at the $NaNO_3$ sample was negligible. Likewise, the 78 Hz field at the LiCl sample was found to be small. However, the fringe field of the 78 Hz modulation will induce small voltages in the field-lock correction coils and the 25 Hz modulation coils. To prevent these voltages being mixed with the small rf signal which is invariably radiated by the Robinson spectrometer, passive rejection filters tuned to 78 Hz were included in the supply leads to these coils.

5.2.14 Manual operation console

This allows the user to control the system without recourse to the computer, this feature being very useful for maintenance and testing purposes. The console consists of the following items:- an address select switch, sixteen data switches, a three-position "function" switch, three "strobe" buttons, sixteen monitor lamps, various monitor outputs, and the digital

panel meter. The exact effect of the "function" and "strobe" buttons depends upon the particular device being addressed. However, the general procedure of data entry is similar to that used to the frequency control D/A converter, and we shall use this device as an example.

The address of the D/A converter is selected by the address select switch; the monitor and data lines are now connected to the device, and the monitor lamps display the contents of the D/A data latches. To change their contents, the new data are fed into the sixteen data switches, the four most significant switches being in this case redundant. The function switch is then set to LOAD, the relevant "strobe" button is pressed, and the data are transferred from the data switches to the D/A data latches. The monitor lamps now display the new data.

It is sometimes desirable to be able to increment or decrement the number stored in the data latches. This can be achieved via the console by setting the "function" switch to UP. Each time the "strobe" button is pressed, the number is incremented by one. Similarly, when the "function" switch is DOWN, the number is decremented by one.

All the functions which can be accomplished by hand via the manual operation console can be performed

much more rapidly by the computer when it is controlling the system. In this mode, the computer disables the manual operation console. However, since the computer is sending data to the device for only brief periods, manual operation is still possible most of the time.

5.2.15 Computer, interface and teletype

The computer, which is the ALPHA 16 model, manufactured by Computer Automation Inc., is a sixteen-bit stored program machine with 4 K words of magnetic core memory. The following processor options were added: a buffered teletype (TTY) interface, a "power fail restart" and a crystal-controlled real time clock (RTC). The TTY interface connects the computer to the TTY, thereby enabling data transmission between the two. The contents of the core memory are not lost during a power failure and the "power fail restart" option provides an orderly shut-down and restarting procedure if such an event occurs. The RTC provides, with the necessary software, the capability to perform operations in real-time.

The interface is an in-house constructed device which is physically located in the computer case, and which is connected to the system by two fifty-conductor cables. Its function is to enable data to pass between the computer and the spectrometer system, while

allowing each to perform at their appropriate speed.

The TTY is a model ASR33 which consists of a keyboard, printer, and a paper tape punch and reader. The latter feature provides a comparatively quick and easy method of storing and entering programs.

We shall now describe the software aspects of the computer. Whereas there are many data analysis languages such as FORTRAN, there did not appear to be a widely accepted high-level real-time language suitable for our purpose. Therefore, one had to be created which would fit into the 4 K of memory available. The alternative procedure of writing all instructions in machine language would, in the long run, have been much more time consuming.

There are basically two parts to the software: the control program which occupies approximately 3 K of memory, and the user program which can occupy the remainder. The control program is made up of a number of segments which collectively control the spectrometer system and TTY via the user program. Also in this part is a set of instructions used for "debugging" programs. The user program consists of a series of user instructions plus space for data storage and messages. Available to the user program are two working registers, the math register (MR) in which mathematical operations are performed, and the input/

output register (I/O Reg), in which logical operations are performed and through which pass spectrometer system data and instructions. User instructions are in general two sixteen-bit computer words long. The first word is the instruction-class code while the second often contains an address to find or place data. Also included in the second word are up to four bits specifying which instruction within the class is to be performed. The instruction class set is as follows: Write on TTY, Add, Subtract, Multiply, Divide, Modulus, Jump, Increment and skip if 0, AND I/O Reg, Complement I/O Reg, Compare I/O Reg and skip if equal, Set RTC, Test RTC, Read A/D, Pack A/D reading. (This last instruction converts the A/D reading into the floating point format, mentioned in section 5.2.12.) This group of instructions enables the spectrometer system to be efficiently controlled. Additional instructions could be added, but at the expense of the already small space available for the user program.

Each user instruction actually requires many machine instructions in its execution, a task handled by the control program. The control program also performs numerous other housekeeping tasks which are invisible to the user, eg keeping track of time, handling interrupts, and checking user instructions for validity. This last task becomes very visible if any errors are

detected, since the user program is then terminated, and a message indicating the type of error is printed on the TTY!

The use of subroutines facilitates the writing of complex programs, and often enables them to occupy less memory space. There is provision for four levels of subroutines in the user program, this number being the result of a compromise between user language flexibility and available user language space.

Both integer and floating-point numbers are available to the user program. Integer numbers occupy one memory word and have a range ±16,383. Floating-point numbers occupy two consecutive memory words and have a range $\pm 10^{\pm 34}$ with an accuracy of seven decimal digits. Floating-point numbers are used whenever a large dynamic range is important; integer numbers are used in cases, such as manipulations to generate computer addresses, where round-off errors are intolerable.

In our real-time system, the handling of interrupts from the system is a vitally important aspect of its operation. We shall now describe this in some detail. There are two interrupt lines to the computer, one dedicated to the A/D converter, the other to the remaining five system interrupts. This second line is fed from an interrupt receiver which manipulates the five interrupts. To avoid conflicts of interest if two

of these interrupts occur simultaneously, they are rated in priority so that the one with highest priority is serviced first. In order of decreasing priority, the device interrupts are frequency counter, misbalance detector, and those for the NMR field-lock. The interrupt receiver stores each device interrupt in a latch, the output of which passes through a number of masks before being connected to the computer interrupt line. The latches may be reset, and the state of the masks (ie mask or unmask) set by the user program via an Input/Output instruction. This rather complicated arrangement is essential because the computer may be performing a task in which it would be very inconvenient, or even disastrous, to be interrupted by a particular device or devices. When an interrupt is received by the computer, it determines from which device it came and then jumps to the relevant user-program interrupt subroutine.

An example of a situation in which interrupts could cause a problem, is in the control of the A/D converter. After the computer sends a signal to the A/D converter to start its measurement, the computer waits for a signal on the first interrupt line which signifies the end of conversion. If, for example, the field-lock interrupt is received during this wait, the computer would service the field-lock. However,

the field-lock interrupt subroutine involves the A/D converter! To avoid this problem, the control program automatically masks the second interrupt line during the wait, and resets it to its original state after completion of the A/D instruction.

The other major real-time function is the RTC. The user program sets the RTC in units of 10 ms by the set RTC instruction. A test RTC instruction checks if the time is up, and, if it is, the computer jumps to a specified program step. When going from a lower to a higher level subroutine, time is still kept in the lower level. It is also possible to set and test the RTC in the higher level subroutine independently of the lower one.

Finally, we give an example of a simple program which could be used to produce a linear field sweep. In this example, the field is not locked, and the sweep is produced by incrementing the contents of the field-lock D/A converter once per second. The program is shown in Fig. 5.7, the numbers being in hexadecimal format in which decimal numbers ten through fifteen are written A through F respectively. The control program executes step 0 and proceeds with steps 1, 2, 3, etc. unless directed otherwise. The starting location and the storage space indicated can actually be anywhere within the user area of the memory. The parameters of

Figure 5.7

A sample program written in the user language. This program could be used to produce a linear magnetic field sweep. The "contents" column will be entered into the computer memory.

MEMORY LOCATION	STEP NUMBER	CONTENTS	COMMENTS
0E00	0	8088	LOAD MR WITH CONTENTS OF 0F00
0E01		0F00	
0E02	1	8081	ADD CONTENTS OF 0F01 TO MR
0E03		0F01	
0E04	2	8088	LOAD I/O REG WITH MR
0E05		4000	
0E06	3	8089	OUTPUT I/O REG TO FIELD-LOCK D/A
0E07		C0E2	
0E08	4	808A	SET RTC TO 1 SEC
0E09		0064	
0E0A	5	8085	TEST RTC & JUMP TO STEP 5 IF
0E0B		3005	TIME IS NOT UP
0E0C	6	8085	JUMP TO STEP 1
0E0D		0001	
0F00		0000	SWEEP START NUMBER
0F01		0001	SWEEP INCREMENT NUMBER

the sweep can be changed by simply feeding different numbers into locations OE09, OF00 and OF01 of the computer memory.

5.2.16 System monitors

One way of checking the operation of the hardware is to use the manual operation console to view the state of each device. However, in order to view parameters stored within the computer without interrupting the experiment, two monitoring devices are connected to the Buss. Each contains a sixteen-bit data latch and an associated D/A converter; the user program can output important parameters to either of these devices.

Other monitors which are not connected to the Buss are a Hewlett-Packard (HP) 1201B oscilloscope to view the audio output of the Robinson spectrometer, a Darcy TSI 385R frequency counter with decimal display connected to the output of the frequency converter, and two HP 680M strip-chart recorders to monitor the outputs of the ω_m and $2\omega_m$ lock-in detectors. The event markers of these recorders are under the control of the system.

5.2.17 Power supplies

As will be seen in section 5.4.3, a major problem was the elimination of systematic errors arising from the interaction between the rf and audio signals. The ac power line, ground connections and common dc power supplies provide a very effective means of coupling the two signals. In order to reduce the problem, the units associated with the rf circuitry of the spectrometer were physically separated from the low frequency digital and analogue circuitry. Moreover, the rf and audio sections were fed from "independent" 115 V ac power lines. Extensive rf filtering was incorporated in the power line feeding the audio circuitry.

Grounding, as opposed to shielding, is only important for operator safety. Indiscriminate grounding of equipment can cause "ground loops" thereby creating troublesome spurious signals. The ground pins on the ac power plugs of the individual units were therefore not used. Instead a cold water pipe was used as a common ground point for the various parts of the system.

To improve electrical isolation, the Robinson spectrometer has its own 200 V - 200 ma and -6.3 V power supplies which incorporated extensive rf and audio filtering. Since the system contains approximately forty cards of circuitry, it was impractical to provide

an independent dc power supply for each card. Instead, a few high-power supplies were used, and isolation was achieved by incorporating shunt regulators on all of the cards.

5.3 User language computer programs

5.3.1 General considerations

The flow-charts for the User Programs are shown in Figs. 5.8 to 5.16. Although these are not written in the user language, they do display the logical sequence of events of the actual computer program. The flow-chart is read as follows: start at step 0 and proceed with steps 1, 2, 3, etc., unless directed otherwise by a branch step. These are written in the form of a question. If the answer is yes, then branch; if the answer is no, then proceed with the next step.

Normally, the computer is running the "Data Collection Program" and its subroutines, which are "N2", "156" and "Resonance-Lock". When an interrupt is received from the system, the "Data Collection Program" is halted and the computer then jumps to the appropriate interrupt subroutine, namely "Frequency Counter", "Field-Lock" or "Misbalance Detector". On completion of this subroutine, the computer returns to the "Data Collection Program" and continues where

Figure 5.8

Flow chart of the "Data collection program". This program uses the "N2", "156" and "Resonance lock" subroutines.

```
01   SET SIGMA(U,S,E,ESQUARE) = 0
02      ↓
03   OUTPUT 156 Hz PHASE 0
04      ↓
05   OUTPUT SATURATION POWER OFF
06      ↓
07   SET N3 CNTR = 0
08      ↓
09   SET SIGMA(Du,Ds,78) = 0
10      ↓
11   ENTER N2 SUBROUTINE
12      ↓
13   OUTPUT SATURATION POWER ON
14      ↓
15   MASK MISBALANCE DETECTOR INTERRUPT
16      ↓
17   WAIT 30 SECS
18      ↓
19   CLEAR MISBALANCE DETECTOR INTERRUPT
20      ↓
21   UNMASK MISBALANCE DETECTOR INTERRUPT
22      ↓
23   WAIT 10 SECS
24      ↓
25   ENTER N2 SUBROUTINE
26      ↓
27   ENTER N2 SUBROUTINE
28      ↓
29   OUTPUT SATURATION POWER OFF
30      ↓
31   WAIT 40 SECS
32      ↓
33   ENTER N2 SUBROUTINE
34      ↓
35   CALCULATE SIGMA Du/N2 = U
36      ↓
37   STORE U
38      ↓
39   ADD U TO SIGMA U
40      ↓
```

```
41   CALCULATE DΣ/N2 = S
42      ↓
43   STORE S
44      ↓
45   ADD S TO SIGMA S
46      ↓
47   CALCULATE S/U = E
48      ↓
49   STORE E
50      ↓
51   ADD E TO SIGMA E
52      ↓
53   ADD ESQUARE TO SIGMA ESQUARE
54      ↓
55   CALCULATE (SIGMA S)/(SIGMA U) = EAV
56      ↓
57   STORE EAV
58      ↓
59   CALCULATE DELTA EAV
60      ↓
61   STORE DELTA EAV
62      ↓
63   ENTER RESONANCE-LOCK SUBROUTINE
64      ↓
65   PRINT U,S,E,EAV,DELTA EAV
66      ↓
67   INCREMENT N3 CNTR
68      ↓
69   IS N3 CNTR ≠ N3 ? ——————→(9)
70      ↓
71   PRINT TIME,CNTR 1TO 5
72      ↓
73   SET CNTR 1TO 5 = 0
74      ↓
75   JUMP TO STEP 7 ——————→(7)
```

Figure 5.9

The flow chart of the "N2" sub-routine which is used by the "Data collection program".

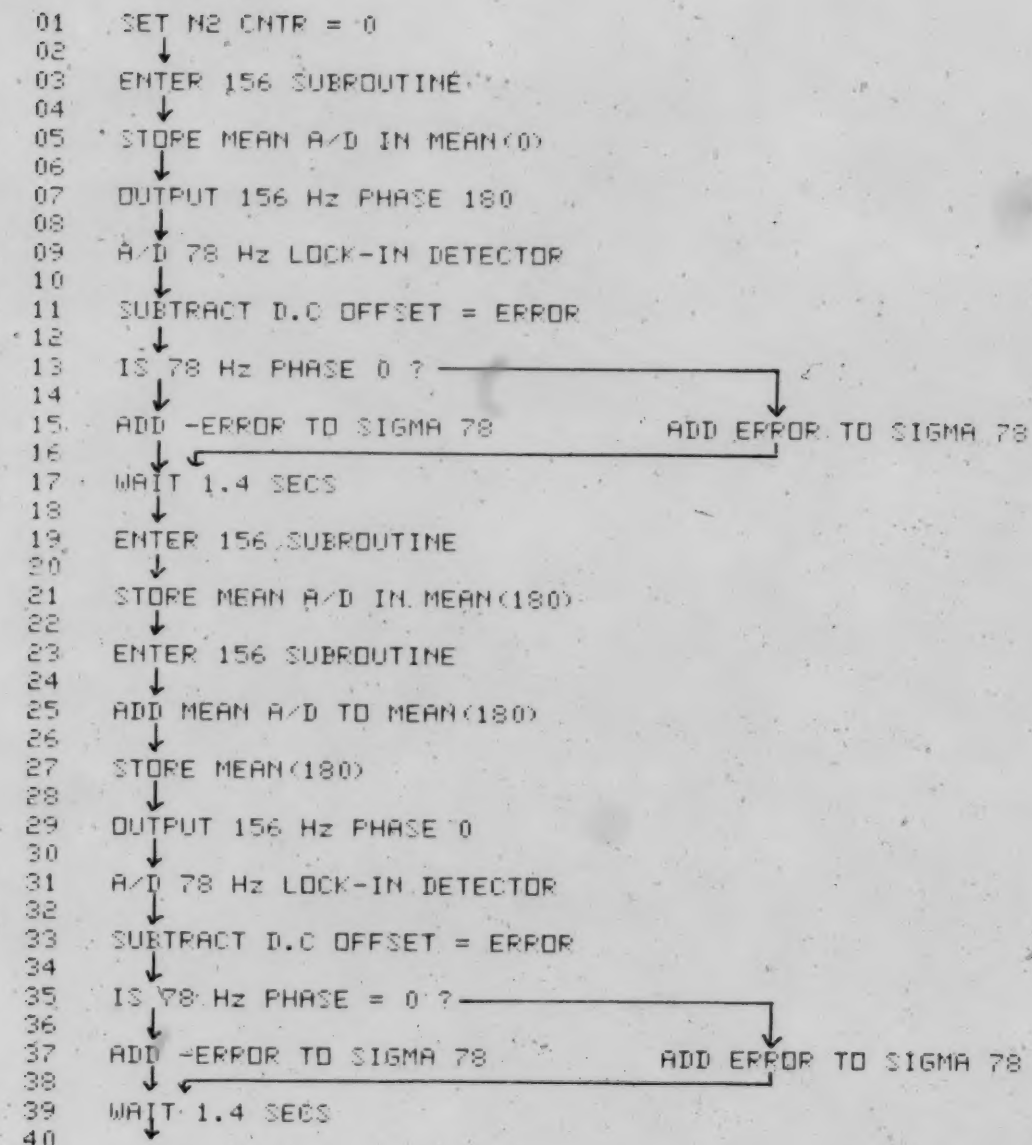
01 SET N2 CNTR = 0
02
03 ENTER 156 SUBROUTINE
04
05 STORE MEAN A/D IN MEAN(0)
06
07 OUTPUT 156 Hz PHASE 180
08
09 A/D 78 Hz LOCK-IN DETECTOR
10
11 SUBTRACT D.C OFFSET = ERROR
12
13 IS 78 Hz PHASE 0 ?
14
15 ADD -ERROR TO SIGMA 78
ADD ERROR TO SIGMA 78
16
17 WAIT 1.4 SECS
18
19 ENTER 156 SUBROUTINE
20
21 STORE MEAN A/D IN MEAN(180)
22
23 ENTER 156 SUBROUTINE
24
25 ADD MEAN A/D TO MEAN(180)
26
27 STORE MEAN(180)
28
29 OUTPUT 156 Hz PHASE 0
30
31 A/D 78 Hz LOCK-IN DETECTOR
32
33 SUBTRACT D.C OFFSET = ERROR
34
35 IS 78 Hz PHASE = 0 ?
36
37 ADD -ERROR TO SIGMA 78
ADD ERROR TO SIGMA 78
38
39 WAIT 1.4 SECS
40

```
41   ENTER 156 SUBROUTINE
42      ↓
43   ADD MEAN A/D TO MEAN(0)
44      ↓
45   STORE MEAN(0)
46      ↓
47   CALCULATE (MEAN(0))-(MEAN(180)) = D
48      ↓
49   IS SATURATION POWER ON ?──────────────┐
50      ↓                                  ↓
51   ADD D TO SIGMA D0                  ADD D TO SIGMA D1
52      ↓                                  ↓
53   INCREMENT N2 CNTR  <──────────────────┘
54      ↓
55   IS N2 CNTR ≠ N2 ? ──────────→(3)
56      ↓
57   EXIT
```

Figure 5.10

The flow chart of the "156" sub-routine which is used by the "Data collection program".

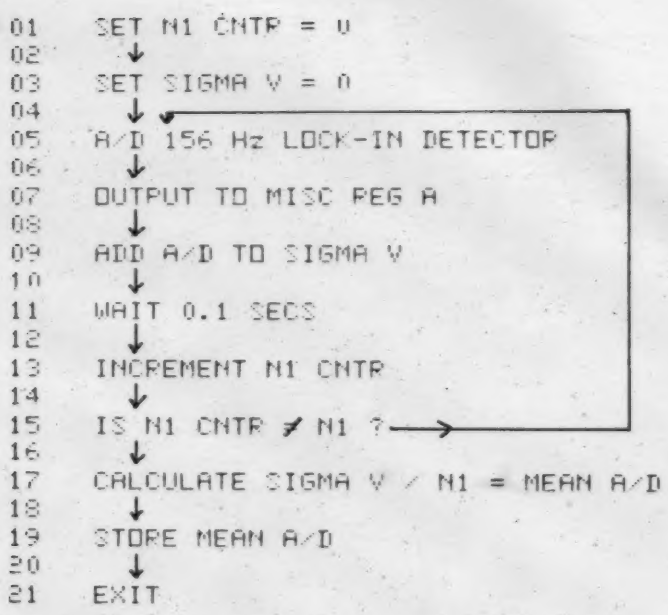
01 SET N1 CNTR = 0
02 ↓
03 SET SIGMA V = 0
04 ↓
05 A/D 156 Hz LOCK-IN DETECTOR
06 ↓
07 OUTPUT TO MISC REG A
08 ↓
09 ADD A/D TO SIGMA V
10 ↓
11 WAIT 0.1 SECS
12 ↓
13 INCREMENT N1 CNTR
14 ↓
15 IS N1 CNTR ≠ N1 ?
16 ↓
17 CALCULATE SIGMA V / N1 = MEAN A/D
18 ↓
19 STORE MEAN A/D
20 ↓
21 EXIT

Figure 5.11

The flow chart of the "Resonance lock" subroutine which is used by the "Data collection program".

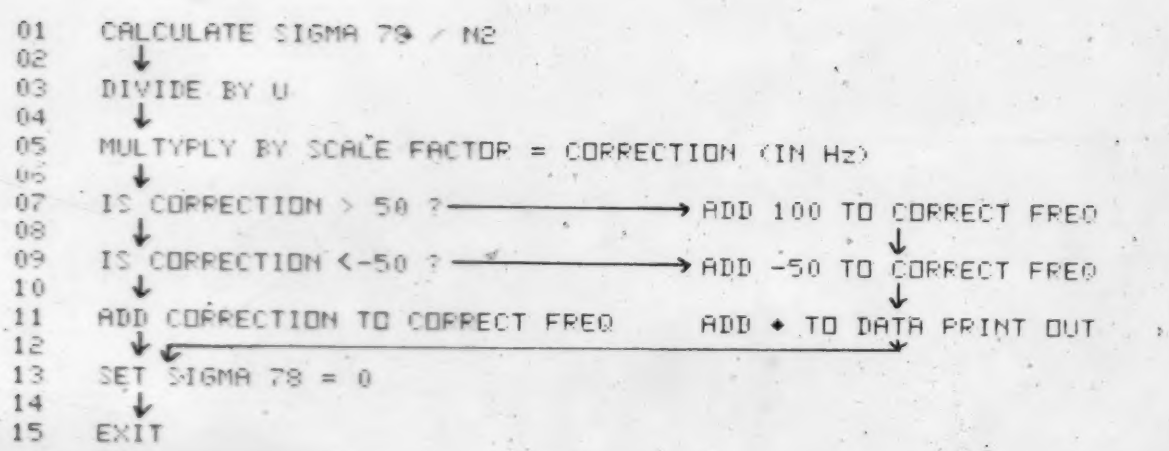
01 CALCULATE SIGMA 79 / N2
02
03 DIVIDE BY U
04
05 MULTYPLY BY SCALE FACTOR = CORRECTION (IN Hz)
06
07 IS CORRECTION > 50 ?
ADD 100 TO CORRECT FREQ
08
09 IS CORRECTION <-50 ?
ADD -50 TO CORRECT FREQ
10
11 ADD CORRECTION TO CORRECT FREQ
ADD ♦ TO DATA PRINT OUT
12
13 SET SIGMA 78 = 0
14
15 EXIT

Figure 5.12

The flow chart of the
"Frequency counter interrupt"
subroutine.

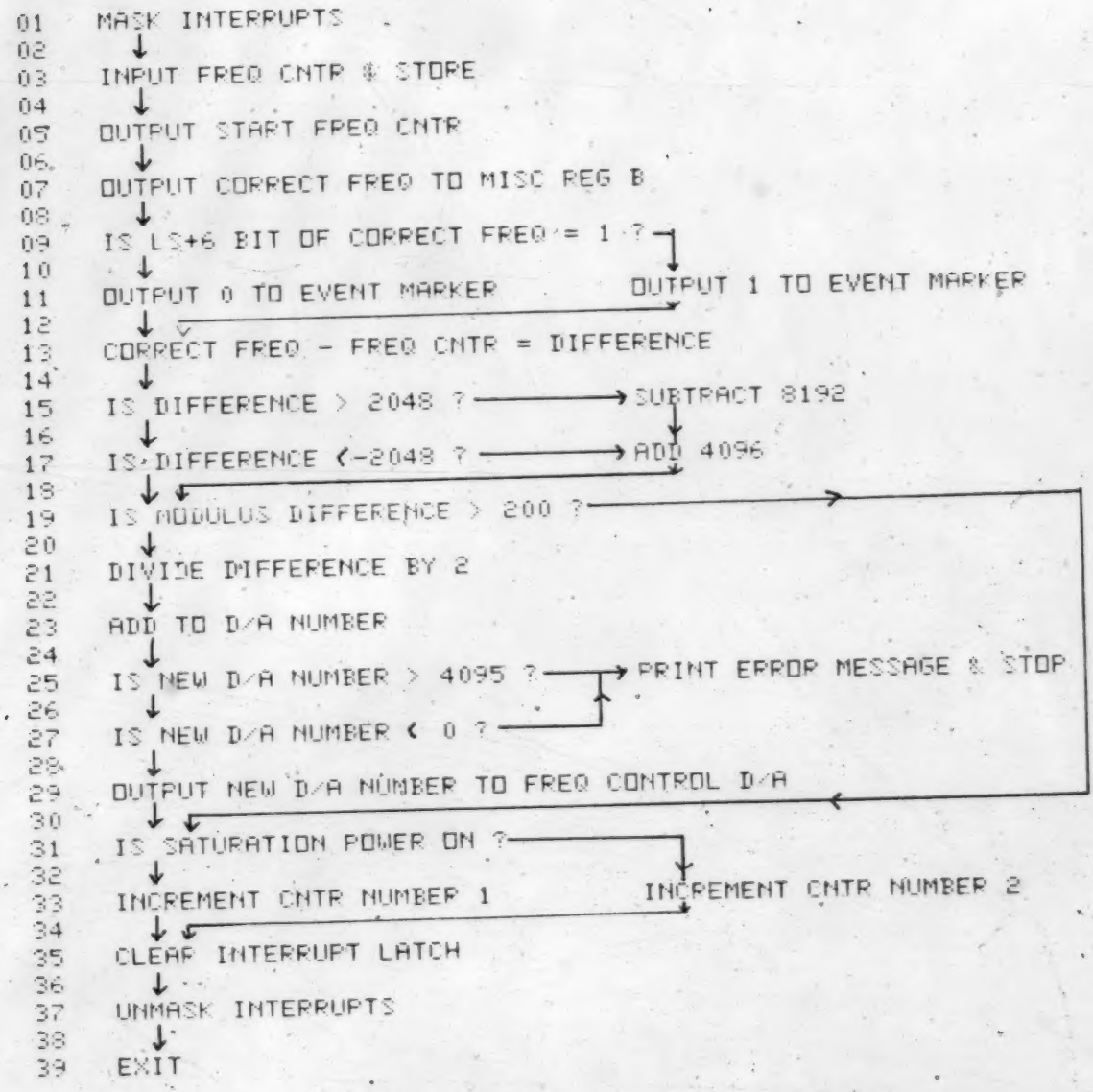
01 MASK INTERRUPTS
02
03 INPUT FREQ CNTR & STORE
04
05 OUTPUT START FREQ CNTR
06
07 OUTPUT CORRECT FREQ TO MISC REG B
08
09 IS LS+6 BIT OF CORRECT FREQ = 1 ?
10
11 OUTPUT 0 TO EVENT MARKER
OUTPUT 1 TO EVENT MARKER
12
13 CORRECT FREQ - FREQ CNTR = DIFFERENCE
14
15 IS DIFFERENCE > 2048 ?
SUBTRACT 8192
16
17 IS DIFFERENCE <-2048 ?
ADD 4096
18
19 IS MODULUS DIFFERENCE > 200 ?
20
21 DIVIDE DIFFERENCE BY 2
22
23 ADD TO D/A NUMBER
24
25 IS NEW D/A NUMBER > 4095 ?
PRINT ERROR MESSAGE & STOP
26
27 IS NEW D/A NUMBER < 0 ?
28
29 OUTPUT NEW D/A NUMBER TO FREQ CONTROL D/A
30
31 IS SATURATION POWER ON ?
32
33 INCREMENT CNTR NUMBER 1
INCREMENT CNTR NUMBER 2
34
35 CLEAR INTERRUPT LATCH
36
37 UNMASK INTERRUPTS
38
39 EXIT

Figure 5.13

The flow chart of the "NMR Field-lock interrupt" subroutine.

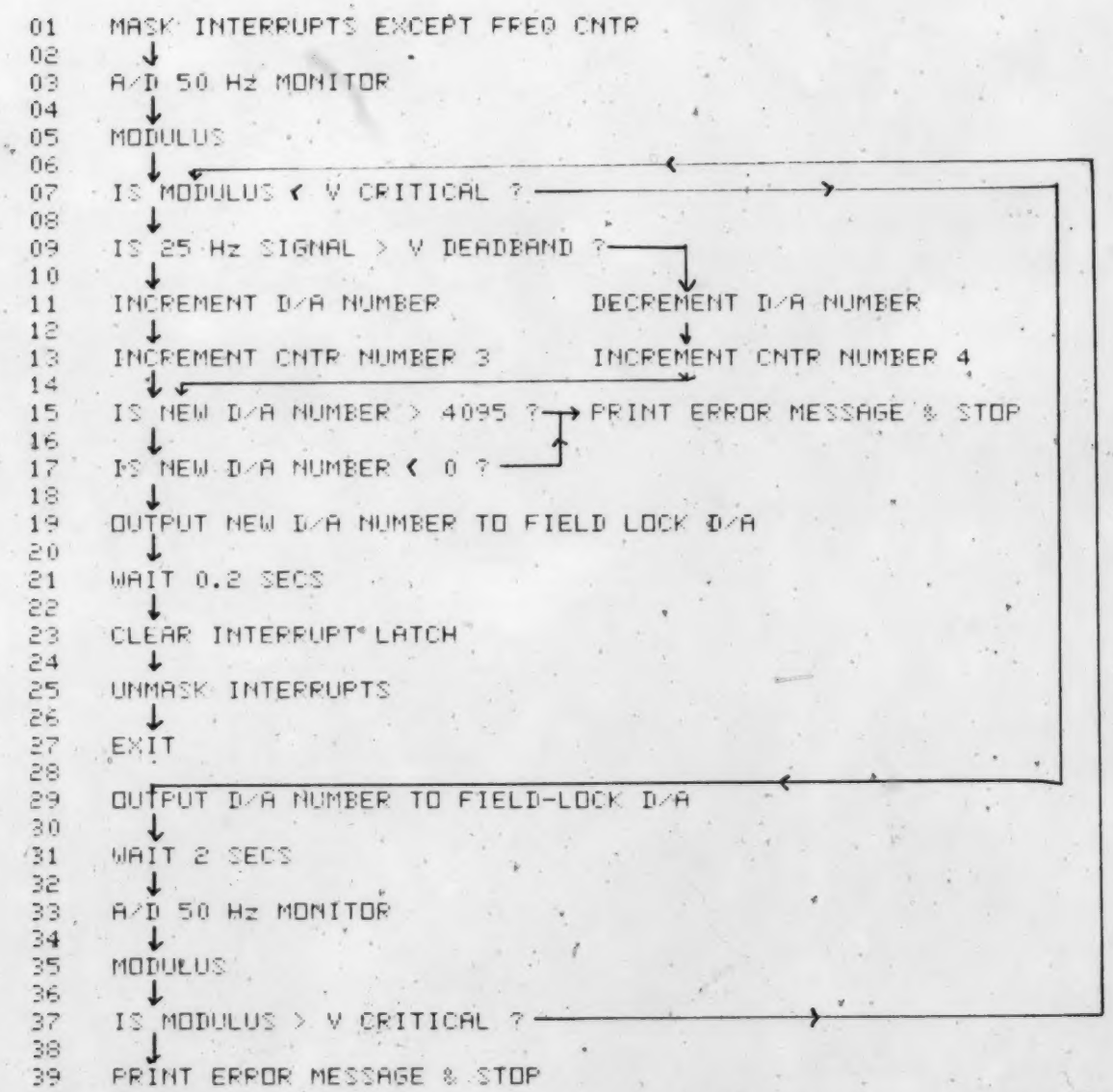
MASK INTERRUPTS EXCEPT FREQ CNTR
A/D 50 Hz MONITOR
MODULUS
IS MODULUS < V CRITICAL ?
IS 25 Hz SIGNAL > V DEADBAND ?
INCREMENT D/A NUMBER
DECREMENT D/A NUMBER
INCREMENT CNTR NUMBER 3
INCREMENT CNTR NUMBER 4
IS NEW D/A NUMBER > 4095 ?
PRINT ERROR MESSAGE & STOP
IS NEW D/A NUMBER < 0 ?
OUTPUT NEW D/A NUMBER TO FIELD LOCK D/A
WAIT 0.2 SECS
CLEAR INTERRUPT LATCH
UNMASK INTERRUPTS
EXIT
OUTPUT D/A NUMBER TO FIELD-LOCK D/A
WAIT 2 SECS
A/D 50 Hz MONITOR
MODULUS
IS MODULUS > V CRITICAL ?
PRINT ERROR MESSAGE & STOP

Figure 5.14

The flow chart of the "Balance network interrupt" subroutine.

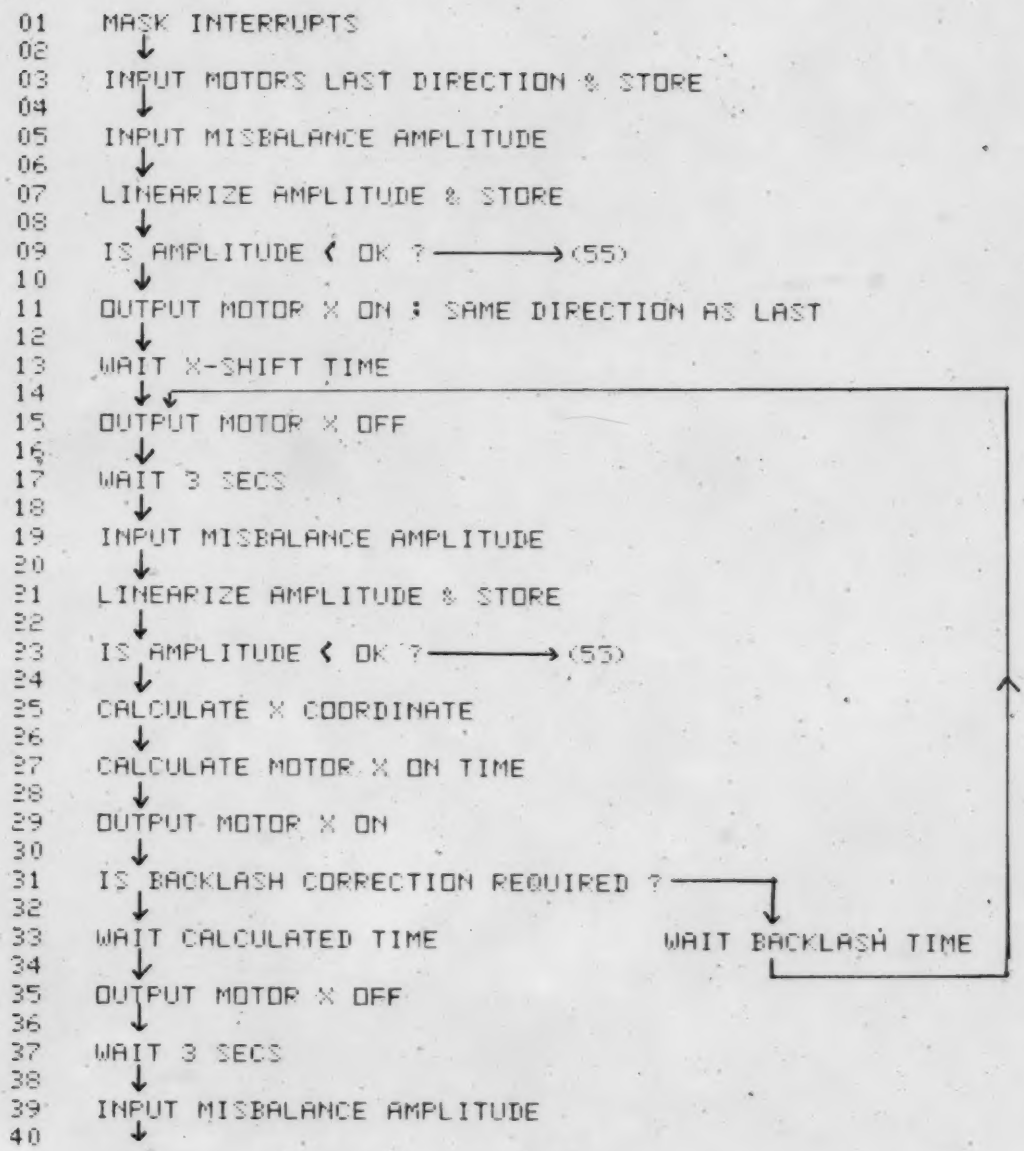
01 MASK INTERRUPTS
03 INPUT MOTORS LAST DIRECTION & STORE
05 INPUT MISBALANCE AMPLITUDE
07 LINEARIZE AMPLITUDE & STORE
09 IS AMPLITUDE < OK ?
(55)
11 OUTPUT MOTOR X ON ; SAME DIRECTION AS LAST
13 WAIT X-SHIFT TIME
15 OUTPUT MOTOR X OFF
17 WAIT 3 SECS
19 INPUT MISBALANCE AMPLITUDE
21 LINEARIZE AMPLITUDE & STORE
23 IS AMPLITUDE < OK ?
(55)
25 CALCULATE X COORDINATE
27 CALCULATE MOTOR X ON TIME
29 OUTPUT MOTOR X ON
31 IS BACKLASH CORRECTION REQUIRED ?
33 WAIT CALCULATED TIME
WAIT BACKLASH TIME
35 OUTPUT MOTOR X OFF
37 WAIT 3 SECS
39 INPUT MISBALANCE AMPLITUDE

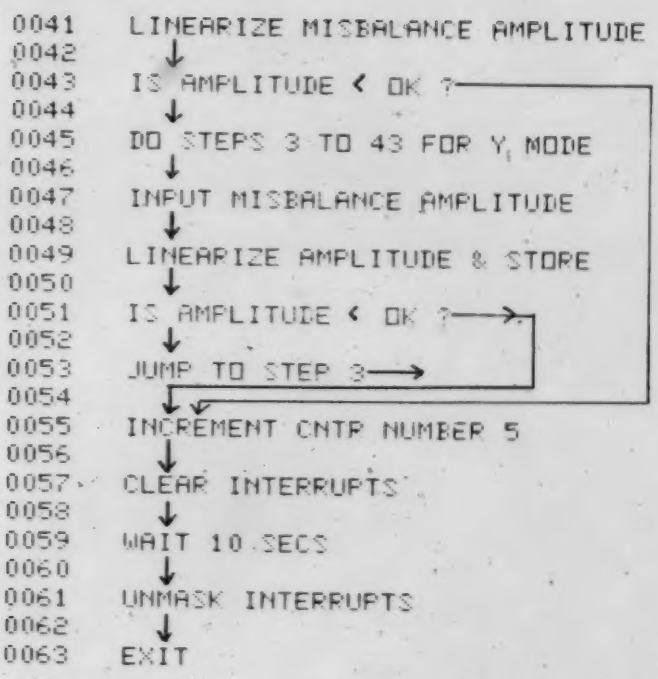
0041 LINEARIZE MISBALANCE AMPLITUDE
0042
0043 IS AMPLITUDE < OK ?
0044
0045 DO STEPS 3 TO 43 FOR Y, MODE
0046
0047 INPUT MISBALANCE AMPLITUDE
0048
0049 LINEARIZE AMPLITUDE & STORE
0050
0051 IS AMPLITUDE < OK ?
0052
0053 JUMP TO STEP 3
0054
0055 INCREMENT CNTR NUMBER 5
0056
0057 CLEAR INTERRUPTS
0058
0059 WAIT 10 SECS
0060
0061 UNMASK INTERRUPTS
0062
0063 EXIT

Figure 5.15

The flow chart of the

"Frequency sweep" program.

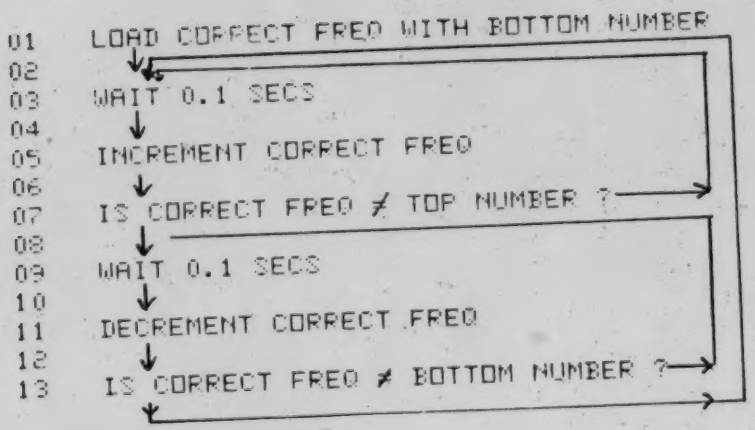
01 LOAD CORRECT FREQ WITH BOTTOM NUMBER
02
03 WAIT 0.1 SECS
04
05 INCREMENT CORRECT FREQ
06
07 IS CORRECT FREQ ≠ TOP NUMBER ?
08
09 WAIT 0.1 SECS
10
11 DECREMENT CORRECT FREQ
12
13 IS CORRECT FREQ ≠ BOTTOM NUMBER ?

Figure 5.16

The flow chart of the "Transient experiment" program.

```
01   OUTPUT SATURATION POWER ON
02     ↓
03   WAIT 2 SECS
04     ↓
05   OUTPUT MASK INTERRUPTS
06     ↓
07   OUTPUT SATURATION POWER OFF
08     ↓
09   OUTPUT START FABRI-TEK
10     ↓
11   OUTPUT UNMASK INTERRUPTS
12     ↓
13   WAIT 41 SECS
14     ↓
15   JUMP TO STEP 1
```

it left off.

The "Frequency Sweep Program" is used to generate a triangular frequency sweep for the spectrometer. It is used instead of the "Data Collection Program" whenever it is necessary to plot or search for a resonance.

Of the total memory space of 4095 words, only 1160 are available for the user programs. Of these, approximately 1000 are occupied by the 500 user instructions and the remainder are usable for data storage.

We discuss in the following sections 5.3.2 to 5.3.6 the programs used for the enhancement experiment.

5.3.2 The "Data Collection" Program

As discussed in section 5.1, the ω_m lock-in detector maintains the spectrometer frequency at the resonance center and the $2\omega_m$ lock-in detector measures the resonance amplitude. The output of the $2\omega_m$ lock-in detector is shown for one "saturation cycle" in Fig. 5.2. At the start of this cycle, the lock-in detector reference has a phase 0° (say) and the saturation power is off. Data is collected for ten seconds and then the reference phase is changed to 180°, thus reversing the lock-in detector output. After waiting 1.4 seconds to allow the output from Tchebyscheff low-pass filter to come to within 0.05% of its final value, another twenty seconds of data is collected. The

reference phase is now reversed back to 0° and, after the 1.4 seconds wait, ten seconds of data are again collected. This completes one "phase-cycle", which is repeated two more times. The saturation power is then applied and the resonance amplitude thus increases rapidly. (The noise level also increases due to noise from the saturation source.) A time of forty seconds is allowed for the spin system to reach equilibrium. Six "phase-cycles" are then performed. The saturation power is thereafter removed and the spin system relaxes back to the unsaturated state. (This recovery allows the value of W_1 to be determined as discussed in section 4.2.) Forty seconds after removing the saturation power, three more "phase-cycles" are performed. The "saturation cycle" is completed by the teletype printing out the experimental data. Every fifth "saturation cycle", some diagnostic information is printed with the experimental data.

The flow charts of the program which generated the sequence of events just described are shown in Figs. 5.8 to 5.10. This program also analyzes the data collected. In these flow charts, N1 is the number of times per quarter "phase-cycle" that the $2\omega_m$ lock-in detector is measured with the A/D converter; N2 is the number of times per quarter "saturation cycle" that the "phase-cycle" is performed, and N3 is the

number of "saturation cycles" performed between diagnostic data printing. In the present experiment, they are 100, 3 and 5 respectively. In Figs. 5.8 to 5.10, D is the true peak resonance amplitude for one "phase-cycle". The quantity U_i is the mean over the i'th "saturation cycle" of the D values obtained in the absence of the saturation power. Similarly S_i is the mean of the D values obtained in the presence of the saturation power.

We shall now describe some aspects of the data analysis. The output of the $2\omega_m$ lock-in detector in general includes a dc offset. This offset, however, remains constant on reversing the reference phase, whereas the resonance signal changes sign. Therefore, the difference between the lock-in detector signals obtained at the two reference phase settings is a measure of the true peak-to-peak resonance amplitude. Also, because equal time is spent collecting data at each of the two phase settings, and because the "phase-cycle" is such that the data for each setting is centered about the same point in time, D is unaffected by linear drifts in the dc offset. Higher order drifts do, however, introduce an error in D, but it is unlikely that such drifts would occur consistently over many "phase-cycles". Therefore, the error introduced will statistically average to zero. The

"saturation cycle" similarly cancels completely any error due to a linear gain drift and reduces any error caused by non-linear drifts.

Ideally, the "phase" and "saturation" cycles should be short compared with the characteristic time of any drifts. However, there are practical limitations as to how short these cycles can be. One is the forty second wait required for the spin system to reach equilibrium. The shorter the "saturation cycle", the greater the proportion of time spent in this wait period, therefore less time is spent collecting data. The other waiting period is the 1.4 seconds required by the low-pass filter to stabilize after a reference phase-change. This time can be reduced by increasing the filter bandwidth. This would mean that the A/D sampling rate would have to be increased proportionally, to avoid aliasing problems (Carlson, 1975) and loss of data. Our A/D converter has a maximum practical sampling rate of 10 Hz, which implies that components with frequencies above 5 Hz must be rejected. This was achieved by setting the 3 db cut-off frequency of the Tschebyscheff filter to 1 Hz. Hence for the cycle shown in Fig. 5.2, data was collected for an acceptable 80% of the time.

Although S_i and U_i, the enhanced and unenhanced resonance amplitudes, have normally distributed errors, the ratio $E_i = S_i/U_i$ will in general have a skewed distribution with a long tail on the high-value side. We therefore take as our best estimate of the enhancement EAV = $\Sigma S_i/\Sigma U_i$ rather than $\bar{E}$ the mean of the individual E_i. The difference between $\bar{E}$ and EAV depends upon the error in U_i, and in our case was found to be approximately 1%. We obtain the random error in EAV from the scatter of E_i about the mean, using the expression

$$(\delta EAV)^2 = \frac{1}{n(n-1)} \left\{ (\Sigma E_i^2) - \frac{1}{n} (\Sigma E_i)^2 \right\} . \qquad (5.5)$$

The quantity δEAV could alternatively have been calculated from the errors in ΣU_i and ΣS_i. However, this has the disadvantage that one would have to take into account correlations in U_i and S_i caused by gain variations. The effect of such gain variations on the value of E_i is, of course, minimized by the structure of the "saturation cycle" as described previously.

The values of U_i, S_i, E_i, EAV and $(\delta EAV)^2$ are printed on the teletype after each saturation cycle: A two hour sample is shown in Fig. 5.17.

Figure 5.17

A two-hour sample of the data "printout" obtained during the steady state double resonance measurements.

```
U= -5.611847E+00 S= -8.155416E+00 E= +1.453250E+00
EAV= +1.453250E+00  +2.384186E-07

U= -5.367164E+00 S= -8.339816E+00 E= +1.553710E+00
EAV= +1.582361E+00  +1.261592E-03

U= -5.408147E+00 S= -7.974300E+00 E= +1.474498E+00
EAV= +1.493165E+00  +6.228553E-04

U= -5.376705E+00 S= -7.981791E+00 E= +1.484513E+00
EAV= +1.491028E+00  +3.544892E-04*

U= -5.584389E+00 S= -8.067274E+00 E= +1.444612E+00
EAV= +1.481550E+00  +2.972030E-04*
T= +00335
+01391
+01563
+00000
+00001
+00004

U= -5.384547E+00 S= -8.026966E+00 E= +1.498741E+00
EAV= +1.483062E+00  +2.081129E-04

U= -5.472248E+00 S= -8.284849E+00 E= +1.513975E+00
EAV= +1.487490E+00  +1.691312E-04

U= -5.516047E+00 S= -8.349989E+00 E= +1.513763E+00
EAV= +1.490804E+00  +1.386106E-04

U= -5.341648E+00 S= -8.391632E+00 E= +1.578984E+00
EAV= +1.499534E+00  +1.794556E-04

U= -5.390581E+00 S= -7.962885E+00 E= +1.477185E+00
EAV= +1.497321E+00  +1.580702E-04
T= +00666
+01390
+01590
+00000
+00002
+00002
```

5.3.3 The "Frequency Counter Interrupt" Subroutine

The loops which control the Robinson spectrometer frequency are shown in Fig. 5.18. The frequency counter is contained within the FAST LOOP, the function of which is to maintain the spectrometer frequency at a predetermined "Correct Frequency". The purpose of the SLOW LOOP will be discussed in section 5.3.4.

The flow chart for the frequency counter interrupt subroutine is shown in Fig. 5.12. This program is entered when the frequency counter generates an interrupt signifying the end of the frequency count. Steps 9 and 11 of the program provide frequency markers on the chart recorder in the following manner. The "Correct Frequency" is stored in the computer as a binary number. Whenever the 64 Hz bit is one, a "one" is fed to the chart recorder event marker. Correspondingly, when the 64 Hz bit is zero a "zero" is fed to the event marker. Thus, the event marker generates a square wave of "period" 128 Hz, whenever the frequency sweep program is being executed. Steps 15 and 17 remove the ambiguity introduced by the 12-bit count number supplied by the frequency counter. If the apparent change in the spectrometer frequency is greater than 200 Hz, it is assumed that the frequency counter has malfunctioned for this count; therefore no correction

Figure 5.18

Block diagram showing how the frequency of the Robinson spectrometer may be varied and controlled.

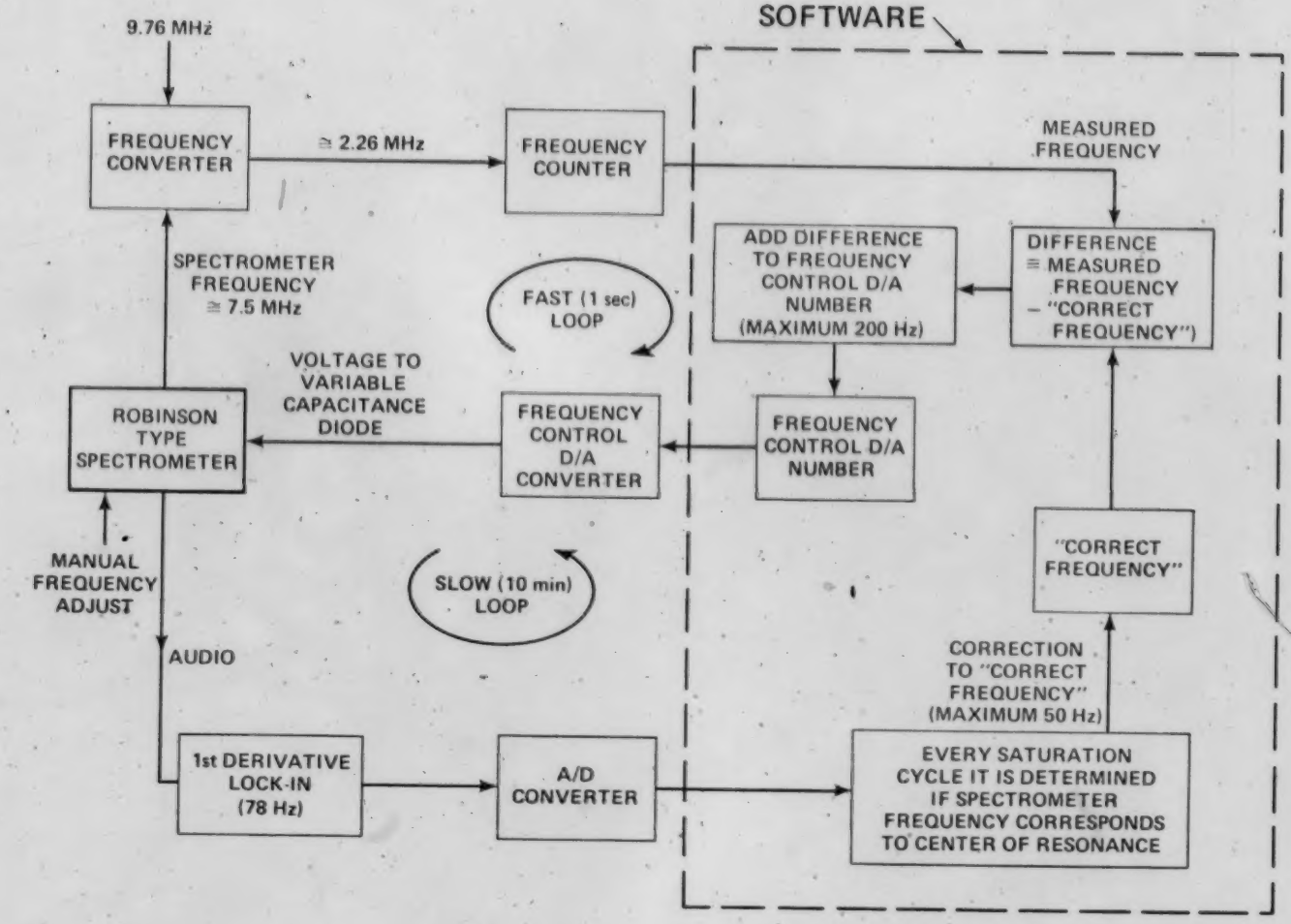
SOFTWARE
9.76 MHz
FREQUENCY CONVERTER
≅ 2.26 MHz
FREQUENCY COUNTER
MEASURED FREQUENCY
ADD DIFFERENCE TO FREQUENCY CONTROL D/A NUMBER (MAXIMUM 200 Hz)
DIFFERENCE ≡ MEASURED FREQUENCY – "CORRECT FREQUENCY")
SPECTROMETER FREQUENCY ≅ 7.5 MHz
FAST (1 sec) LOOP
VOLTAGE TO VARIABLE CAPACITANCE DIODE
ROBINSON TYPE SPECTROMETER
FREQUENCY CONTROL D/A CONVERTER
FREQUENCY CONTROL D/A NUMBER
"CORRECT FREQUENCY"
MANUAL FREQUENCY ADJUST
SLOW (10 min) LOOP
AUDIO
CORRECTION TO "CORRECT FREQUENCY" (MAXIMUM 50 Hz)
1st DERIVATIVE LOCK-IN (78 Hz)
A/D CONVERTER
EVERY SATURATION CYCLE IT IS DETERMINED IF SPECTROMETER FREQUENCY CORRESPONDS TO CENTER OF RESONANCE

is made. Steps 25 and 27 check if the D/A number exceeds the allowable range of the 12-bit frequency control D/A converter. Steps 31 and 33 are used to count the number of times this subroutine is used. These numbers are part of the diagnostic information printed every five "saturation cycles".

5.3.4 The "Resonance-Lock" Program

If the resonance-lock is achieved in the usual continuous analogue manner, a systematic error in the determination of enhancement could result for the following reason. The output of the $2\omega_m$ lock-in detector is an even function of the frequency deviation from the resonance center. Therefore, the mean detector output will depend not only upon the resonance amplitude but also on the magnitude of these frequency deviations. As the signal-to-noise ratio of the error signal is, in general, different for the saturated and unsaturated parts of the cycle, the magnitude of the frequency deviations would also be different. Hence, the value of E obtained would depend upon the difference in magnitude of these frequency fluctuations between the two parts of the saturation cycle. This systematic error can be avoided by keeping the locking frequency fixed throughout one complete "saturation cycle", and only making corrections to this frequency

between cycles.

The "Frequency Counter Interrupt" subroutine keeps the spectrometer frequency locked to the "Correct Frequency"; the "Resonance-lock" program ensure that this frequency coincides with the resonance center. The ω_m lock-in detector provides the error signal for achieving this condition, as indicated in the SLOW LOOP of Fig. 5.18. The error signal is sampled every twenty seconds, as indicated in Fig. 5.9. (For convenience, this sampling occurs every time the $2\omega_m$ lock-in detector reference phase is reversed.) At the end of each saturation cycle (i.e. once per ten minutes), the cumulative error ($\Sigma 78$) is used to determine the required change in the "Correct Frequency" by means of the relation:

$$\text{"Correction (in Hz)"} = k\Sigma 78/U_i, \qquad (5.6)$$

as indicated in Fig. 5.11. The parameter k is an experimentally determined scale factor. The cumulative error ($\Sigma 78$) is divided by the resonance amplitude U_i, so as to avoid having to redetermine k for each spectrometer observing power or crystal setting. The "Correction (in Hz)" is usually not more than 20 Hz, so if a correction of greater than 50 Hz is indicated, it is assumed to be due to noise rather than a genuine shift of resonance frequency. If this situation occurs,

a correction of only 50 Hz is made and the user is notified by a star (*) appearing after the data printout of this cycle. Stars occurring in many successive cycles usually indicate an equipment malfunction.

5.3.5 The "Balance Network" Subroutine

This subroutine can be entered if an interrupt is generated by the misbalance detector, indicating a significant NMR sensitivity change, as discussed in section 5.2.7. The purpose of this subroutine is to readjust the balance network so that the misbalance detector output falls to an acceptable level (corresponding to an NMR sensitivity change of no more than 0.01%). This is the "OK" level mentioned in the flowchart given in Fig. 5.14. Unfortunately, the misbalance detector gives only the amplitude but not the phase of the misbalance. This deficiency can be overcome by the following procedure: We measure the misbalance amplitude A_1 and then turn on, for a given time, the motor driving the in-phase (X) mode. This changes the misbalance by a previously calibrated amount Δx in the x direction. We now again measure the misbalance amplitude A_2, and the x-coordinate of the final misbalance is given by

$$x = (A_2^2 - A_1^2 + \Delta x^2)/2\Delta x \quad . \qquad (5.7)$$

This procedure is shown in Fig. 5.19. Once the x-coordinate is known, the X-mode motor is turned on for the correct time and in the correct direction to make the x-coordinate of the misbalance equal to zero. A similar procedure can then be performed for the orthogonal (Y) mode. This procedure is repeated if necessary, until the desired misbalance level is reached.

For the above procedure to work in practice, a number of imperfections have to be accounted for. The output of the misbalance detector is not perfectly linear with input amplitude; this output is therefore linearized by a simple polynomial transformation. Also, the inertia of the motors and the backlash in the reduction gear-train are not negligible. The first problem is overcome by waiting three seconds after the motors are switched off before measuring the misbalance. For the standard Δx or Δy shifts, the backlash problem was avoided by choosing the sign of the shift to be such that the motor turns in the same direction as before. Whenever a correction calls for the motors to turn in the opposite direction to its last movement, the motor is activated for a sufficient time to take up the backlash. Since a perfect backlash correction is not possible, the misbalance amplitude is remeasured

Figure 5.19

Vector diagram illustrating the procedure used to rebalance the "Balance network".

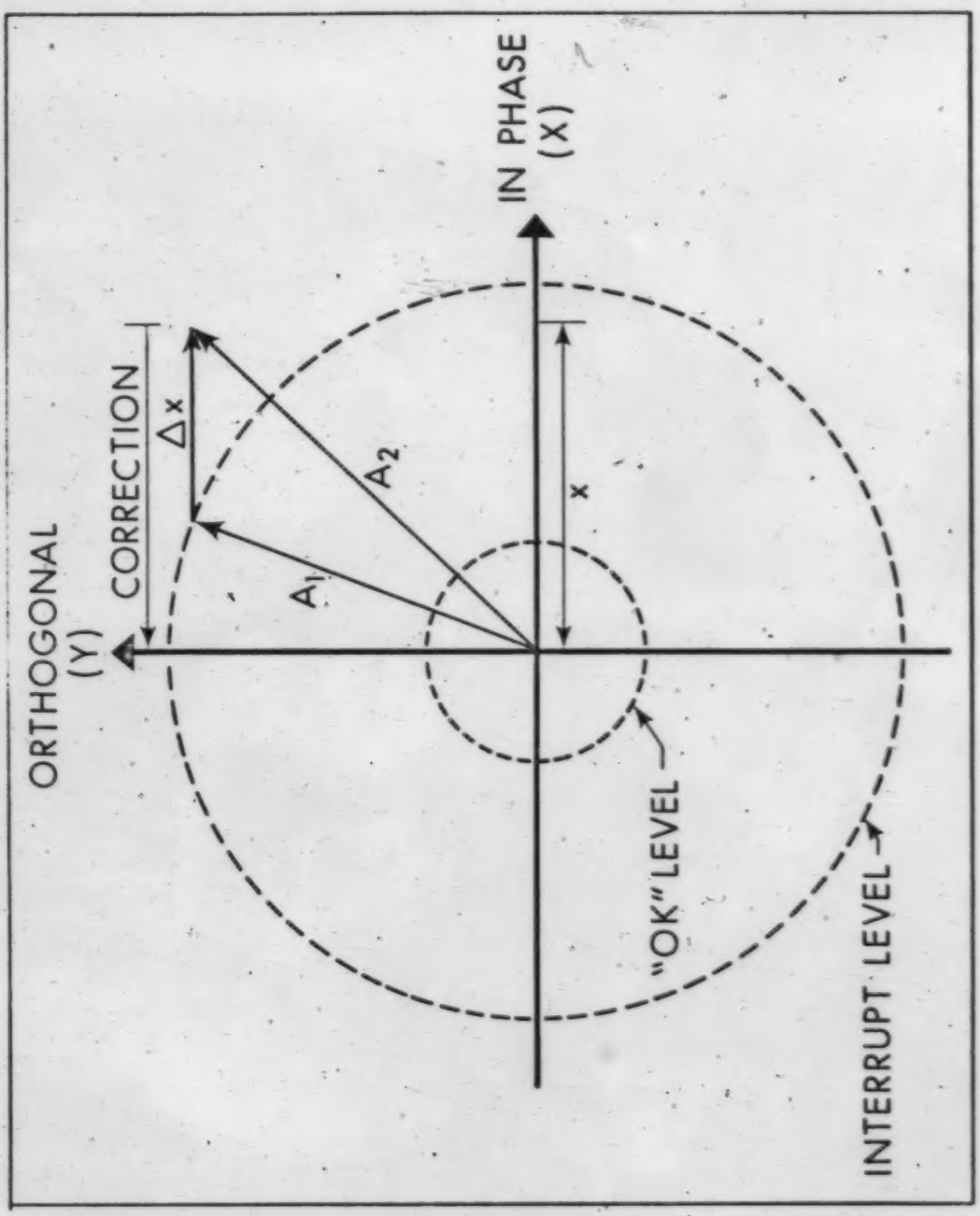
IN PHASE
(X)
ORTHOGONAL
(Y)
CORRECTION
Δx
A2
A1
x
"OK" LEVEL
INTERRUPT LEVEL

and the new x (or y) coordinate is calculated. A final problem is the Joule heating of the delay line which causes the orthogonal mode to drift for several seconds after the saturating signal is applied.. The misbalance detector interrupt is therefore masked for the first thirty seconds to allow thermal equilibrium to be achieved and to prevent needless balance-network corrections.

The correction procedure works quite effectively in practice, and only one or two corrections are required to achieve balance. The overall stability of the network is such that at the minimum separation of 20 kHz between center line and satellite, the subroutine was used only about four times per hour.

5.3.6 The "NMR Field-Lock Interrupt" Subroutine

This subroutine performs the software tasks involved with maintaining a constant magnetic field. The block diagram of the NMR field-lock is shown in Fig. 5.6 and the flow-chart is given in Fig. 5.13. A field-lock interrupt is generated if the Rollin lock-in detector output is greater than the deadband, or if the second harmonic monitor output is too small. The deadband voltage was chosen to be equivalent to a one-bit change of the field-lock D/A converter. This

subroutine checks if the second harmonic signal is too small (step 7 of flow chart); if it is, it "outputs" the D/A number to the field-lock D/A converter. This is done in case a stray pulse has altered the D/A contents. In step 9, the computer decides which Rollin lock-in detector interrupt was generated. It then increments or decrements the D/A number as appropriate. Step 13 is part of the diagnostic information printed every five saturation cycles.

Because the magnetic field drifts are typically very slow, the "one-bit-at-a-time correction algorithm" was satisfactory. Occasionally, rapid field changes of up to fifteen bits occur when iron objects are moved within the magnet's fringe field. However, even these transient errors are within the required stability of a few tens of milligauss.

5.4 Systematic errors in the determination of the enhancement

5.4.1 Classification of systematic errors

There are basically three types of systematic errors in the determination of the enhancement; those relating to NMR, those relating to instrumentation, and those relating to data aquisition and analysis. Methods of overcoming systematic errors in the last

category have already been described in section 5.3.2. They consist of data aquisition in "phase" and "saturation" cycles to eliminate offset and gain drift errors, and taking EAV rather than $\bar{E}$ as the best value of the enhancement. In the following two subsections we shall describe the other classes of systematic errors.

5.4.2 NMR - related systematic errors

We can determine W_2/W_1 using any pair of the three resonance lines of ^{23}Na in $NaNO_3$. There are definite advantages, however, to observing a satellite and saturating the center line. As shown in section 3.2, the separation between the satellite and center line is, to first order, proportional to the z component of the electric field gradient at the nuclear site, whereas the much smaller shift of the center line is a second order effect. Lattice imperfections will cause local deviations in the electric field gradient, and it was found experimentally by Kornfeld and Lemanov (1960) that such imperfections result in a small loss of intensity of a satellite line, but a negligible loss in the intensity of the center line. It is therefore safer to saturate the center line rather than a satellite to ensure complete saturation of the spin system.

Failure to achieve complete saturation would obviously lead to low enhancement values.

If any spurious resonances from the materials in the probe occur at the Robinson spectrometer frequency, they will introduce an error in the determination of the enhancement. Sodium is not a constituent of any material used within the body of the probe. However, since ^{63}Cu and ^{23}Na have similar resonance frequencies, all coils and wiring within the probe were made of silver rather than copper. Another possible source of error is the ^{27}Al resonance from the probe body. One would expect the ^{27}Al resonance to be weak since the modulation amplitude is very much less than the ^{27}Al NMR linewidth. (This is particularly true for our present method of detection, since the signal is proportional to the square of the modulation amplitude provided this is small.) Moreover, the aluminium is at least half an inch away from the spectrometer coil. In addition, the rf observing power used in the experiment is very much less than the optimum power for observing the ^{27}Al resonance in aluminium metal. A search over the frequency region where the resonances from $NaNO_3$ can occur revealed no spurious resonances. In addition, the ^{27}Al resonance occurs at a frequency lower than the ^{23}Na center line in $NaNO_3$. We therefore generally made our measurements

on the high frequency rather than the low frequency satellite, thereby ensuring that there was no possibility of a systematic error arising from ^{27}Al.

For the enhancement value to give an accurate measure of W_2/W_1, the resonance line shape must be unaffected by the saturation field. When the transition rate caused by the saturation field becomes comparable with the spin-flip transition rate, "motional" narrowing of the line will occur (Bloch, 1958; Sarles and Cotts, 1958). This would lead to enhancement values which are too large. Estimations of the transition rates indicate that this regime occurs at a saturation level orders of magnitude greater than that used in our work. Also, no evidence of line shapes changes on saturation was found.

According to the theory of Redfield (1955), Provotorov (1961) and Goldburg (1960, 1961), it is not possible to completely saturate a resonance by a steady-state technique, if the saturation frequency is mis-set from the resonance center. As we require essentially complete saturation of the center line, an experiment was performed to investigate how close to the center of the resonance the saturation frequency must be. By performing an enhancement experiment in the normal way, but mis-setting the saturation frequency from the center of the line, the results of Fig. 5.20

Figure 5.20

The enhancement of the high frequency satellite as a function of the frequency offset of the saturation signal from the middle of the center line. The field modulation amplitude corresponds to 1.4 kHz in frequency units. The solid line is the best fit to the data points.

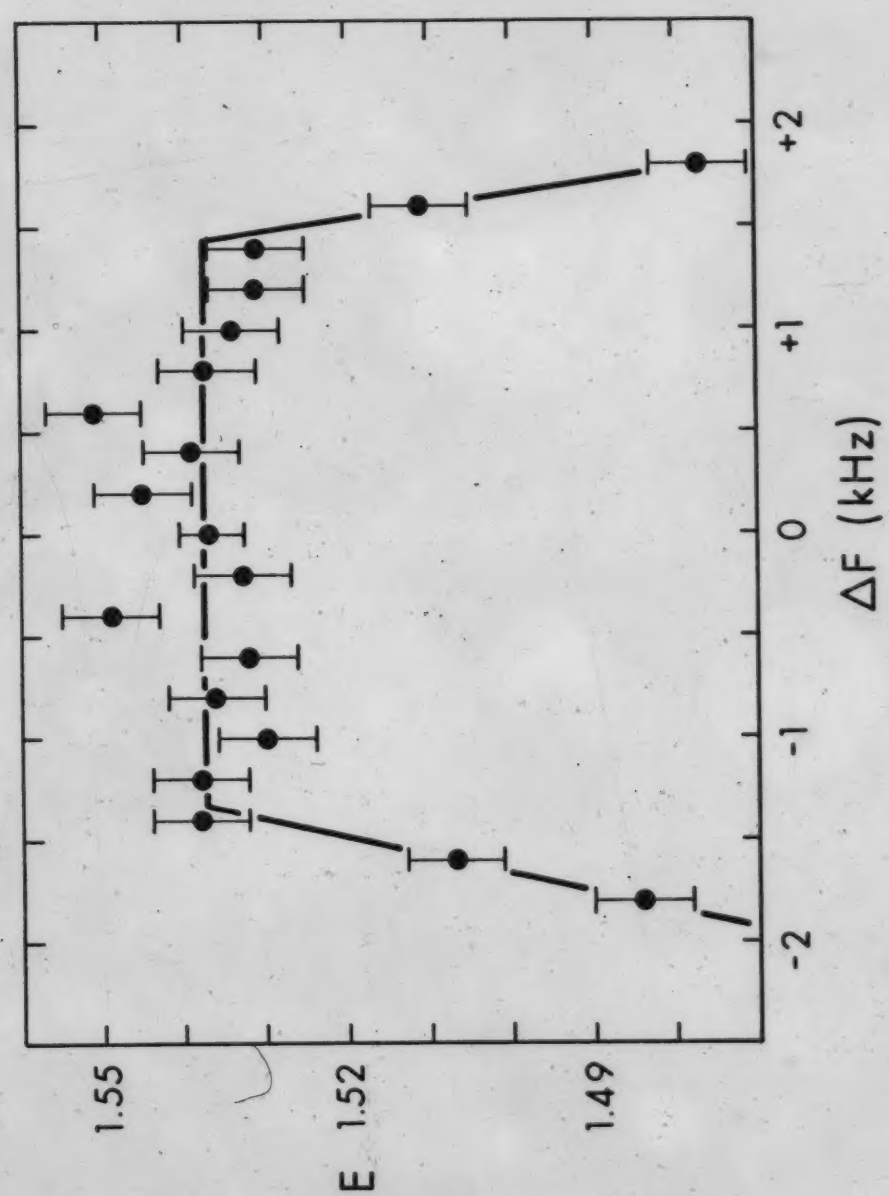
1.55
E 1.52
1.49
-2
-1
0
+1
+2
ΔF (kHz)

were obtained. The extended region of constant enhancement can be understood (Hughes and Reed, 1971) by noting that the field modulation has the effect of sweeping the saturation field back and forth across the resonance. Experimentally it appears that essentially complete saturation occurs provided the modulation takes the saturation field across the resonance center at some stage of the modulation cycle.

Near the crystal orientation $\theta = 54°$, the separation between a satellite and the center line is small, and it is possible for the "wings" of these resonances to overlap. Some of the saturating power would then "leak" into the satellite resonance by spin-exchange interactions (Bloembergen et al, 1959), thereby altering the populations of the various energy levels. This point was investigated by performing an enhancement experiment in which the saturation power was applied to the wing of the satellite resonance. When the separation between the satellite and the center line is 40 kHz and the saturation power is set 20 kHz below the high frequency satellite line, we obtained a satellite enhancement $E = 1.0025 \pm 0.0040$. When the saturation frequency was 40 kHz higher than the high frequency satellite frequency, we obtained $E = 1.0004 \pm 0.0027$. These results indicate that "overlap" effects are unimportant in our crystal, since we would

otherwise expect an enhancement of less than unity.

This is another way in which the saturation field can introduce a systematic error. Sodium nitrate is not a perfectly loss-free dielectric (Mariani et al, 1967). Thus, the large saturation field will directly heat the sample, thereby introducing an asymmetry into the two parts of the "saturation cycle". This will lead to values of enhancement which are too small. The measurements described in the previous paragraph therefore show that overlap effects and heating effects are insignificant.

The linear E-P_{obs} extrapolation is only valid for small values of P_{obs} as was found experimentally by Reed (1970). He observed deviations from linearity when the increase δE in the enhancement caused by the finite P_{obs} was approximately one tenth of the enhancement value. In our measurements, for safety, we restricted our P_{obs} range so that $\delta E/E$ was always less than 0.05. The data obtained at $\theta = 180°$ shown in Fig. 5.21 show no evidence of any non-linearity, although this angular setting is one at which the satellite line saturates comparatively easily.

As will be seen from section 6.4, the observed signal decays exponentially with a time constant of approximately six seconds after removing the saturation power. To avoid the systematic error associated with

Figure 5.21

Enhancement of the high frequency satellite as a function of the spectrometer power P_{obs}. The data were taken when the center line was severely saturated and the crystal orientation corresponded to $\theta = 180°$.

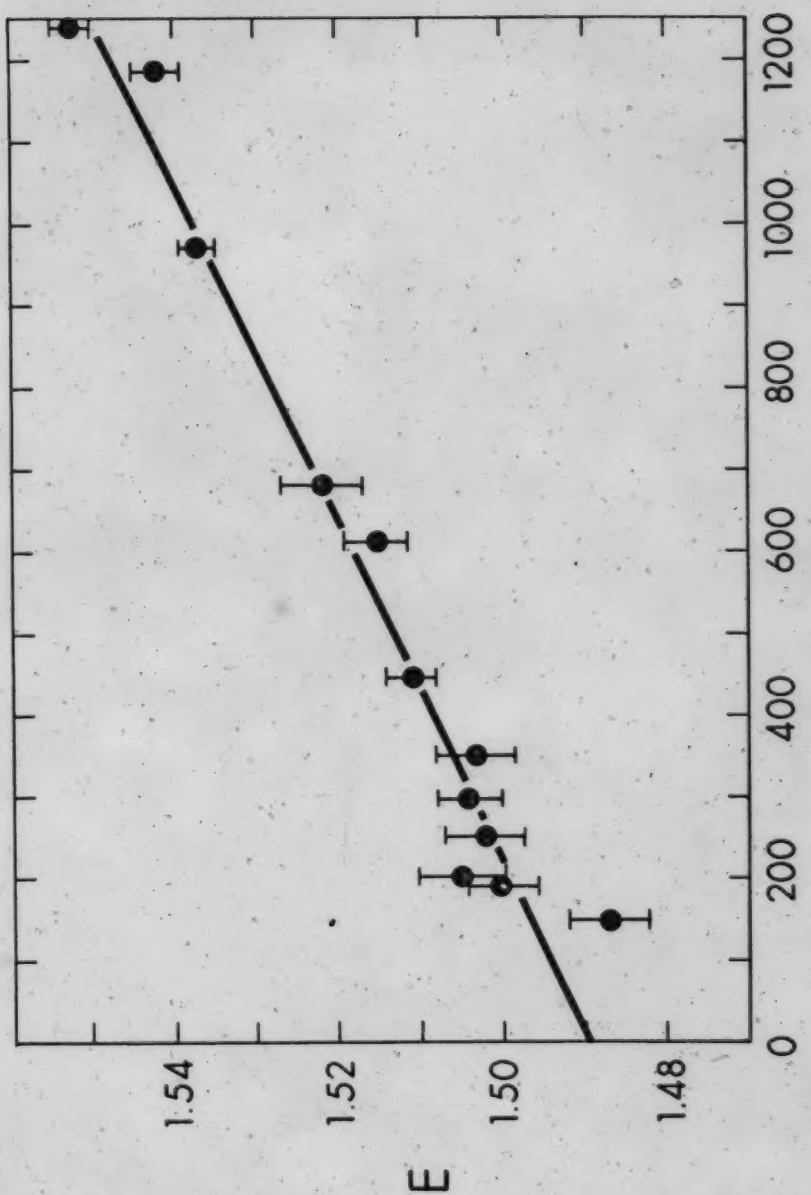
E
1.54
1.52
1.50
1.48
0
200
400
600
800
1000
1200
P_{OBS} (arbitrary units)

recording the unsaturated resonance amplitude while it is recovering from saturation, we must wait several time constants before recording any data. This is the reason for the forty second wait in the "saturation cycles". Calculation shows that at the end of this period, the unenhanced amplitude is 0.06% too large, and the mean error over the whole unsaturated part of the cycle is only 0.001%.

5.4.3 Instrumentation-related systematic errors

One error already mentioned in section 5.2.7 is the NMR sensitivity change caused by a spurious injection of saturation voltage into the spectrometer. Associated with this sensitivity change is a pulling of the spectrometer frequency (Hughes et al, 1973). In fact, for large injections, the frequency pulling can be so severe that the spectrometer is locked to the saturation frequency! Without the frequency-lock, the free-running spectrometer frequency will in general be slightly different for the two parts of the "saturation cycle". Data would therefore be gathered from two different points on the resonance. However, the frequency-lock ensures that the same point on the resonance is observed throughout the complete "saturation cycle".

Another problem is the mixing of the modulation and rf signals within the spectrometer to produce an rf signal which is amplitude modulated at ω_m or $2\omega_m$. This will then cause spurious outputs at the lock-in detectors, whose signs are reversed when the reference phased is reversed. The modulation at $2\omega_m$ is particularly troublesome since it contributes a systematic error to the measured NMR amplitudes. A typical modulation depth for the NMR signals in our experiment is 10^{-6}; we regard a systematic error of 0.1% of this is troublesome. This translates into a maximum spurious modulation amplitude of only 100 picovolts across the sample coil.

One method whereby an amplitude modulation is produced is via the magnetoresistance of the silver spectrometer coil. This has the effect of directly modulating the Q of the tuned circuit. Indeed the only difference between this magnetoresistance effect and NMR absorption is that the latter is resonant whereas the former is not. However, measurement* shows that the magnetoresistance of silver is small, and it is estimated that a two gauss modulation field would produce a negligible modulation depth of 10^{-12} at $2\omega_m$.

---

* We are grateful to Dr. J. Rowlands for performing the magnetoresistance measurement.

An amplitude modulated signal can also be caused by the non-linear mixing of the rf voltage and any voltages at ω_m, or indeed $2\omega_m$, which enter the spectrometer. Voltages at ω_m are more likely to be present than those at $2\omega_m$ because of the low harmonic content of the modulation signal. Initial tests without the NMR sample showed that the U_i and S_i values were non-zero, thus indicating an amplitude modulation at $2\omega_m$. These U_i and S_i values were found to be roughly proportional to the rf amplitude and to the square of the field modulation amplitude. This indicates that mixing was occurring via a cubic term in the transfer characteristics of the rf amplifier. We now discuss various ways by which the modulation voltage can enter the spectrometer, and methods used to overcome this problem.

The field modulation will obviously induce a voltage in the spectrometer sample coil. The coupling to the rf amplifiers was therefore minimized by inserting a high-pass L-C filter between the sample tuned circuit and the first rf stage. The capacitor was approximately 3000 pF; the inductor was self-resonant at 2MHz, and had a resistance of 5 Ω. This filter behaves like a 10^5:1 voltage divider at 78 Hz and like a low-loss capacitative divider at 7.5 MHz.

The fringe field of the modulation coils will also induce voltages in the spectrometer wiring. This

field was reduced an order of magnitude by placing a sheet of 1" thick aluminium between the spectrometer and the modulation coils. Further reduction was provided by placing soft iron tube caps over the sensitive rf amplifying tubes.

The electrostatic coupling between the modulation coils and the probe can give rise to small currents at ω_m flowing in the probe body! These were minimized by feeding the modulation coils from a source which was balanced relative to ground.

The modulation voltage present in the input tuned circuit can also produce an amplitude modulation by a totally different mechanism. This voltage will alter the resonant frequency of the tuned circuit via the variable capacitance diode. A frequency dependent gain, for example, will then convert this frequency modulation into an amplitude modulation. The modulation voltage across the diode was therefore reduced by using four diodes in parallel and decreasing the size of the series capacitor to the smallest value which would give the desired tuning range. As seen from Fig. 5.5, these capacitors form a voltage divider, which in the final configuration provided an order of magnitude reduction of the modulation voltage pickup across the diodes.

Precautions were also taken to prevent signals at the modulation frequency from entering the spectrometer by any other route. All connections, in

particular those from the power supplies, were extensively filtered.

Disappointingly, in spite of all these precautions a significant modulation was present even with the modulation source disconnected! This indicated that the problem was more subtle than appeared at first sight. It was finally traced to the following mechanism: radiation from the spectrometer mixed with signals coherent with the $2\omega_m$ reference voltage and the modulated rf signal was reradiated back into the spectrometer! To reduce this strange phenomenon, the radiation from the spectrometer was reduced by including rf filters in all leads connected to the spectrometer, except the one to the frequency converter. (All of these precautions also reduce the sensitivity of the spectrometer to external radiation.) However, the line from the spectrometer to the frequency converter still provided an unfiltered path into the spectrometer. This line was therefore fed by an amplifier with a low reverse gain, thereby reducing the chance of radiation leaking in by this route. The frequency converter, itself, was mounted adjacent to the spectrometer, and was encased in an "rf tight" steel box. At this stage of the development, the wiring to the probe and balance network was changed from the original coaxial to triaxial cable in order to improve the shielding of these

units.

However, even these additional measures did not eliminate the spurious modulation completely! Tests showed that the amplitude and sign of the spurious U_i and S_i were strongly dependent upon the spectrometer frequency and level. Indeed, it was finally realized that anything that changed the rf radiation field in the laboratory also changed U_i and S_i. The nature of the mechanisms was finally confirmed when the lock-in detectors and their associated equipment were located in a room two hundred feet away from the laboratory. In this configuration the spurious U_i and S_i values were found to be negligible. This was obviously a rather inconvenient permanent arrangement and another solution was sought! The cure was to keep the rf radiation field physically separated from the circuitry containing ω_m and $2\omega_m$ voltages. This was achieved by reconstructing the correlators for the lock-in detectors plus the associated reference and field modulation source in a separate shielded box, which we called "Superbox". All leads entering this unit were extensively rf and audio filtered, and the box was constructed from 1/8" steel. "Rf gaskets" of aluminium foil were used to make the box as rf leak-proof as possible. Furthermore, the circuitry was constructed from low

power logic to reduce the currents flowing at the troublesome frequencies.

A final test of two weeks duration found no evidence of any spurious output, and it is estimated that any residual modulation must be less than one part in 10^{11}.

As mentioned in section 5.4.2, measurement of the enhancement of a satellite when the saturation power was "off resonance" gave an enhancement close to unity. These measurements were performed when the separation between the saturation and observing frequencies was 40 kHz or less. We also measured the "off resonance" enhancement when this separation was 150 kHz. Rather surprisingly, the enhancement was found to be roughly 0.25% low. A careful study of the P_{obs} dependence indicated that this systematic error decreases with decreasing P_{obs}. Hence the error in the determination of W_2/W_1 should be small since they are obtained from an extrapolation of the $E\text{-}P_{obs}$ data. We attribute this frequency-dependent systematic error to the following mechanism. A small amount of radiation at the observing frequency finds its way from the spectrometer into the rf power source supplying the saturation field. Since the balance network is only perfectly balanced at one frequency, there will be a net coupling between the saturation coils and the

spectrometer coil at frequencies other than the saturation frequency. Thus, the spurious signal at the spectrometer frequency will appear as an additional feedback path. This will then change the spectrometer level in a way which depends on its phase and amplitude. The amplitude will depend upon whether the rf power source is on or off. Thus, there will be a difference in the spectrometer level between the two parts of the "saturation cycle", though a change of 0.25% would be too small to detect directly with our spectrometer level monitor. Since the NMR signal amplitude is proportional to the spectrometer level, this mechanism will obviously lead to a systematic error in the measurement of enhancement. From an analysis of the characteristics of the balance network, we would expect that the error would be proportional to the difference between the saturation and observing frequencies, although this point has not been checked.

Another possible source of error in the determination of enhancement is non-linearity of any of the signal-processing stages. Since a typical modulation depth for the NMR is only 10^{-6}, it is extremely unlikely that a significant non-linearity would occur in the rf stages of the spectrometer. The signal plus noise levels in the audio sections of the spectrometer is

typically a few tens of millivolts. Inspection of the tube characteristics indicates that the non-linearity over such a range is very much less than 0.01%. The remainder of the signal processing was performed by operational amplifiers, which, because of the very large amount of negative feedback, are linear to a high degree. Thus, the only significant non-linearity will be caused by any stage overloading. The gain and bandwidth of the various stages were optimized to make full use of the available dynamic range. Also, the signal and noise levels were kept much smaller than the dynamic range. We note that in the stages just prior to the correlators where the noise is "narrow-band", the noise has a Rayleigh distribution (Cohn, 1964). In the stages following the correlators, the noise should have a Gaussian amplitude distribution. The system, from the output of the spectrometer to the computer was nevertheless checked for linearity. No non-linearity was found to within the accuracy of the "five and one half digit" voltmeter used to measure the input signal.

Finally, we consider any systematic errors that can arise from the A/D converter. Its linearity, as specified by the manufacturer, is one half a bit. For typical voltage levels measured, this corresponds to approximately 0.05%. Another error can be introduced

by the following mechanism. If a voltage occurs between count numbers n and n+1, the first number will result. Therefore, on average, the count number will be one half a count too low. However, since we adjusted the overall gain of the system so that the voltage feeding the A/D converter was in the upper part of its dynamic range, this last systematic error is estimated to be less than 0.03%. The performance of our A/D converter was checked and was found to give an error of 0.2 rather than 0.5 count, which therefore implies a systematic error of less than 0.01%.

5.5 Reduction of the random error in the enhancement measurements

5.5.1 Field modulation considerations

Since we are only interested in resonance amplitudes as opposed to lineshapes, we adjusted the modulation amplitude to give a maximum output from the $2\omega_m$ lock-in detector when the spectrometer is locked to the center of the resonance. This optimization was performed at each crystal orientation because of the significant change in the resonance linewidth with crystal orientation.

We note that the output of the spectrometer will in general also contain components at $4\omega_m$, $6\omega_m$ ... $2n\omega_n$. This information is lost, but in principle could be

regained by using a lock-in detector for each additional harmonic. However, the improvement in the error in E would be rather small. For example, if we recovered a $4\omega_m$ signal which was 25% of the amplitude of the $2\omega_m$ signal, the error would be reduced by only 3%. A more promising alternative is to use only the $2\omega_m$ lock-in detector but choose the modulation waveform such that all of the other components are zero. A series of tests in which a different amount of a $3\omega_m$ component was added to the modulation signal indicated that a small increase in signal amplitude of roughly 10% was possible. However, this feature was not incorporated into the system because of the time required to construct and test a working system free from systematic errors. Another alternative would be to use a bisymmetrical square wave field modulation of large amplitude, since this would produce a $2\omega_m$ square wave at the spectrometer output. The $2\omega_m$ component would be 37% larger than in the previous case. However, in this scheme transient effects would have to be considered, and so this point was not pursued.

5.5.2 Optimization of the data collection

To take into account the perturbing effect of the observing power, P_{obs}, on the measured value of E, we use a linear extrapolation of the E-P_{obs} graph to

P_{obs} equals zero. Since W_2/W_1 is derived from the extrapolated value of E, we should collect data in such a way as to make the random error in this value as small as possible

As shown in Appendix III, the optimum data collection procedure consists of spending one ninth of the time at P_{obs} equals the maximum allowable value, and the remainder of the time at a value of observing power a quarter of the maximum. If instead of taking just two data points we were to undertake six measurements at P_{obs} = 1/6, 2/6, 3/6, 4/6, 5/6 and 6/6 of the maximum, and spend time on each point such that each has the same weight, then the random error in the intercept would be 1.7 times greater than that obtained by the two point method. Thus, the total time required for the second method would be $(1.7)^2$ times longer than that required for the first to give equal error in the intercept.

In practice we took a number of different data points. However, the P_{obs} values were in two groups close to the optimum values described in Appendix III. This was done to provide checks on the consistency of the data.

5.6 Experimental details of the transient experiment

As described in section 4.2, the magnitude of W_1 can be determined by recording the recovery of a satellite line after removal of the saturation power from the center line. Such an experiment was performed at $\theta = 180°$ using the computer-controlled spectrometer system. As before, the resonance amplitude was measured using field modulation at ω_m and phase sensitive detection at $2\omega_m$. The "Field-Lock" and "Frequency-Lock" programs (see sections 5.3.6 and 5.3.3) were utilized in order to maintain the resonance condition. To record the recovery of the satellite without distortion, it was necessary to use a detector bandwidth of 5 Hz. The signal-to-noise ratio was then so poor that signal averaging was essential. In principle this could be performed using the computer. However, there was insufficient spare memory, so the signal averaging was achieved externally in a Fabritek Signal Average model number 1062. The data acquisition of this unit was under the direct command of the computer, and the $2\omega_m$ lock-in detector output was sampled every 80 milliseconds for a total of 512 data points per sweep. The flow chart for the user program for this experiment is shown in Fig. 5.16. Approximately twelve hours of data were collected at each value of P_{obs}, and the average

recovery was numerically printed by a Fabritek high speed printer, model number 201.

The optimum "two point" method discussed in Appendix III was not used since the linear extrapolation of the decay constant had not been previously experimentally verified. Also, since the decay had not been experimentally shown to be a single exponential, the complete decay was recorded far out into the baseline for approximately seven time constants.

5.7 Crystal information

Most of the data reported in this thesis were obtained using a sodium nitrate crystal provided by the Harshaw Chemical Company, Cleveland, U.S.A. The crystal was in the form of a cylinder 10 mm in diameter and 9 mm long and the three-fold axis was parallel to the end face of the cylinder. A spectroscopic analysis supplied by the manufacturer showed the following impurities: Al, 3 ppm; Ca, 8 ppm; Mg, 3ppm; Cu $\leq$ 1 ppm and Si $\leq$ 1 ppm. No trace of the paramagnetic impurities Fe, Co, Ni and Mn was found. The crystal was annealed by the manufacturer prior to shipment.

A few measurements were taken on a second sodium nitrate crystal also obtained from Harshaw.

This crystal was 15 mm in diameter and 11 mm long and was of the same nominal purity.

5.8 Determination of the crystal orientation

It is desirable to be able to vary the polar and azimuthal angles θ and ϕ independently of one another. The crystal was therefore installed in a nylon sample holder in such a way that it could be rotated about two mutually perpendicular axes. The crystal itself was mounted in a collar which could be rotated about a horizontal axis relative to the sample holder. The collar was equipped with a graduated scale so that the crystal orientation could be set to within one degree. The sample holder could be rotated about a vertical axis in the NMR probe. It was equipped with a circular scale and vernier which could be set to an accuracy of about a quarter of a degree. The crystal was aligned so that the three-fold axis was along the axis of rotation of the collar. In this arrangement rotation about the vertical axis changed θ but not ϕ, while rotation of the collar altered ϕ but not θ.

The angle θ was determined from the quadrupole splitting (see eq. (3.1) with $\eta = 0$), while the angle ϕ was determined by the following combination of X-ray and NMR techniques. A precession photograph taken with the X-ray beam directed along the three-fold

axis* allowed the angle ϕ to be obtained relative to the crystal cylinder to an accuracy of $\pm 1°$. The centrosymmetric nature of the X-ray pattern (Buerger, 1963) did not allow a distinction to be made between ϕ and $\phi + 60°$. However, this ambiguity was removed by monitoring the NMR linewidth of the center line as a function of θ. By comparion with eq. (3.5), the theoretical expression for the second moment of the center line, the correct x axis could be selected. Moreover, careful linewidth measurement at $\theta = 60°$ and $120°$ (where the amplitude of the cos 3ϕ term is greatest) enabled the position of the x axis to be independently determined to within one degree.

---

* We are grateful to Dr. M.J. Bennett of the Department of Chemistry for performing the X-ray work.

CHAPTER VI

RESULTS

6.1 Orientation dependence of the quadrupole splitting

The electric field gradient at a nuclear site is characterized by the quadrupole coupling constant e^2Qq/h and the asymmetry parameter η, quantities which were introduced in section 2.3. It follows from eq. (3.1) that the first order quadrupole splitting between a satellite and the center line for I = 3/2 is given by

$$\nu_{\pm} - \nu_o = \pm(e^2Qq/4h)(3\cos^2\theta - 1 + \eta\sin^2\theta\cos 2\phi). \qquad (6.1)$$

When this work was begun, it was believed (Reed, 1970) that there was a possibility that the crystal structure of sodium nitrate did not correspond precisely to that predicted from X-ray measurements. In order to verify that the ^{23}Na nuclei did indeed lie on a three-fold symmetry axis, careful measurements of the orientation dependence of the quadrupole splitting were made. In order to detect a very small asymmetry parameter it is clear from eq. (6.1) that the satellite splitting should be measured in the vicinity of $\theta = 90°$ for different values of ϕ. The low frequency satellite line in sodium nitrate was therefore plotted on a chart recorder as the first derivative of the absorption

line. This was done every 0.5° near $\theta = 90°$ for $\phi = -3.5°$ and 86.5°. In order to obtain a precise measurement of the quadrupole splitting the "Field-lock" feature was operative and a linear sweep through the resonance was provided by the "Frequency sweep" facility described in section 5.3.1. The resonance center frequency was taken to be that of the cross-over point of the first derivative signal. To avoid the systematic error associated with the time delay of the low-pass filter on the output of the ω_m lock-in detector, resonances were recorded with both the frequency increasing and frequency decreasing. The mean of the two cross-over frequencies was taken to be the resonance center frequency. Another systematic error can be caused by a drift of the sample temperature since the quadrupole coupling constant has a temperature coefficient of -0.33 kHz/°C (Andrew et al, 1962). The sample was fairly well thermally isolated from the laboratory, so that any temperature drifts would be slow. However, to minimize any residual systematic error, measurements were made alternately at the two settings $\phi = -3.5°$ and 86.5°.

The results of these measurements are shown in Fig. 6.1. The solid curves represent the best fit of the theoretical form (eq. (6.1)) to the data. We find that the maximum satellite separation from the

Figure 6.1

Measurements of the satellite splitting near $\theta = 90°$ for $\phi = -3.5°$ and $\phi = 86.5°$. The solid lines are the least squares fit to the data.

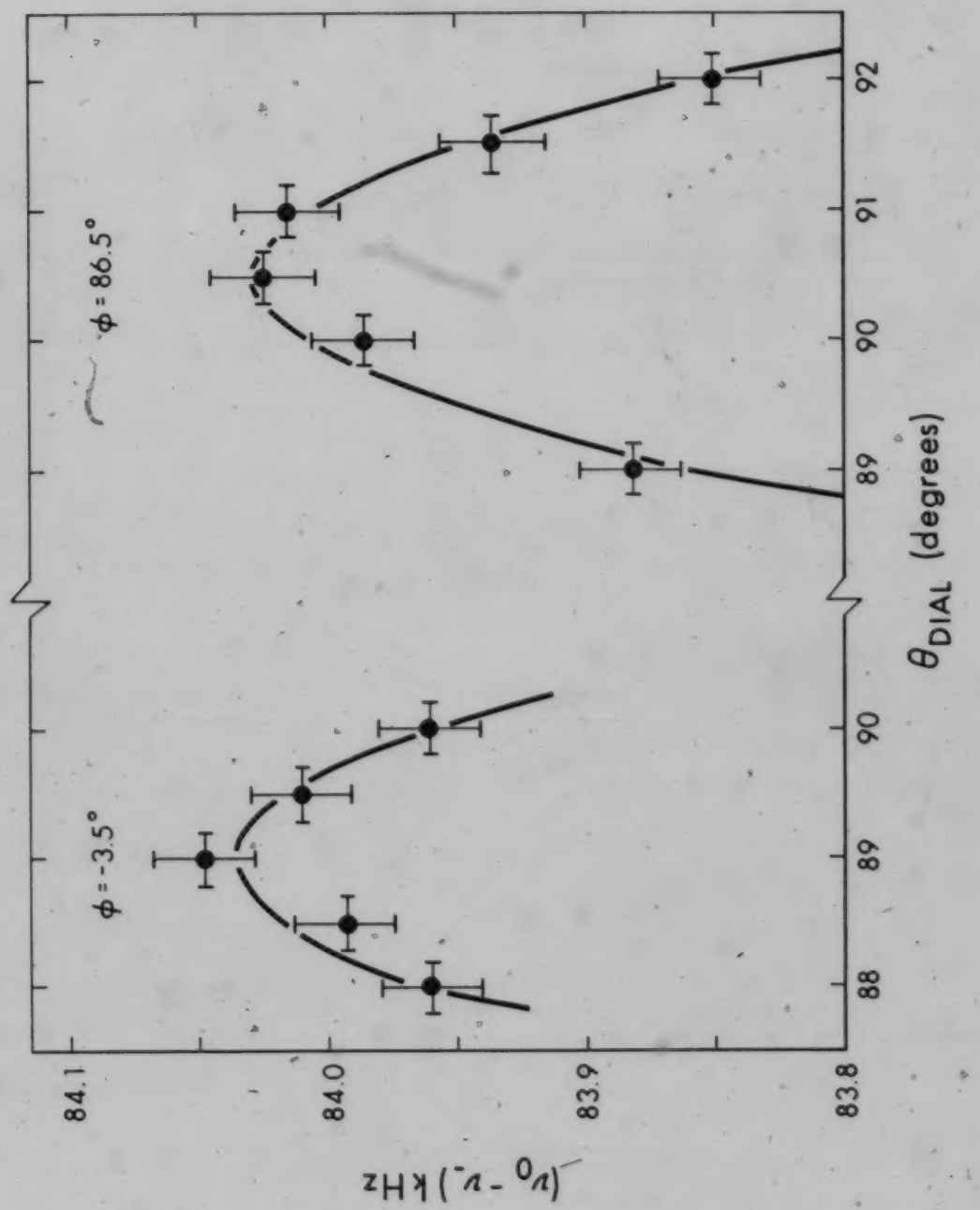
$(\nu_0 - \nu_-)$ kHz
84.1
84.0
83.9
83.8
ϕ = -3.5°
ϕ = 86.5°
88
89
90
89
90
91
92
θ_{DIAL} (degrees)

center line is

$$84.035 \pm 0.025 \text{ kHz} \quad \text{at} \quad \phi = -3.5°$$

and $$84.025 \pm 0.025 \text{ kHz} \quad \text{at} \quad \phi = 86.5° .$$

From this it follows that

$$\eta = (0.6 \pm 1.8) \times 10^{-4}$$

from which it appears that the asymmetry parameter is indeed zero at the ^{23}Na sites in sodium nitrate.

From these measurements we can also obtain the value of the quadrupole coupling constant. Indeed, a more reliable value will in general be obtained by making measurements near $\theta = 90°$ rather than near $\theta = 0°$, since any misorientation of the symmetry axis out of the plane of rotation will give rise to an error at the latter orientation. An alternative method of measuring the satellite splitting at intervals throughout the full 180° range of θ, suffers from the additional drawback that small errors in the angular setting have a large effect on the satellite separation near $\theta = 45°$ and 135°.

The quadrupole coupling constant derived from our measurements in conjunction with eq. (6.1) is

$$336.12 \pm 0.05 \text{ kHz} \quad \text{at} \quad 21.5 \pm 0.3°C .$$

This value is in agreement with the value 334 ± 2 kHz given by Pound (1950), the value of 334.2 ± 0.8 kHz deduced from Andrew et al (1962), and the value of 335.4 kHz deduced from D'Alessio and Scott (1971). The fact that our value is marginally larger is not surprising since the other measurements suffer from the drawbacks mentioned above, which would give rise to a slight underestimate of the quadrupole coupling constant.

6.2 Orientation dependence of the linewidth

Firstly, the ϕ dependence of the NMR linewidth was measured to remove the ambiguity in the X-ray determination of the angle ϕ. Also in view of the anomalous ϕ dependence of W_2/W_1 reported by Hughes and Reed (1971), a careful measurement of the linewidth of the center line and a satellite line was performed. The measurements were made at $\theta = 60°$ and $120°$, where the amplitude of the ϕ dependent term is largest. Assuming that the linewidth is proportional to the square root of the second moment, it follows from eqs. (3.4) and (3.5) that the width of the center line is approximately given by

$$\Delta F_c = 1.791(1 - 0.189 \cos 3\phi) \text{ kHz} \qquad (6.2)$$

at $\theta = 120°$. The corresponding expression for the

width of a satellite line is

$$\Delta F_s = 1.659(1 + 0.189 \cos 3\phi) \text{ kHz} \qquad (6.3)$$

at $\theta = 60°$.

The peak-to-peak linewidth was measured by recording the output of the ω_m lock-in detector when a linear frequency sweep through the resonance was performed. The field modulation amplitude was typically one sixth of the linewidth.

The data are shown in Figs.6.2 and 6.3. The solid line is a least squares fit to the function

$$A + B \cos 3\phi \qquad (6.4)$$

where ϕ is the value deduced from the X-ray work. The least squares fit gave the following results

$$\Delta F_c = (1.755 \pm 0.010)[1 - (0.269 \pm 0.006)\cos 3\phi] \text{ kHz}$$

$$\Delta F_s = (1.594 \pm 0.013)[1 + (0.200 \pm 0.007)\cos 3\phi] \text{ kHz} .$$

The data clearly confirm that the ^{23}Na nuclei lie on a three-fold symmetry axis, and that the X-ray determination of the angle ϕ is correct.

The agreement between the theoretical and experimental linewidths is surprisingly good, considering the approximation (eq. 3.4) that linewidth = $3\sqrt{M_2}$. The agreement for both center line and satellite line

Figure 6.2

Peak-to-peak linewidth of the center line resonance for $\theta = 120°$ as a function of the angle ϕ. The solid line is a least squares fit to the expression

$$A + B \cos 3\phi.$$

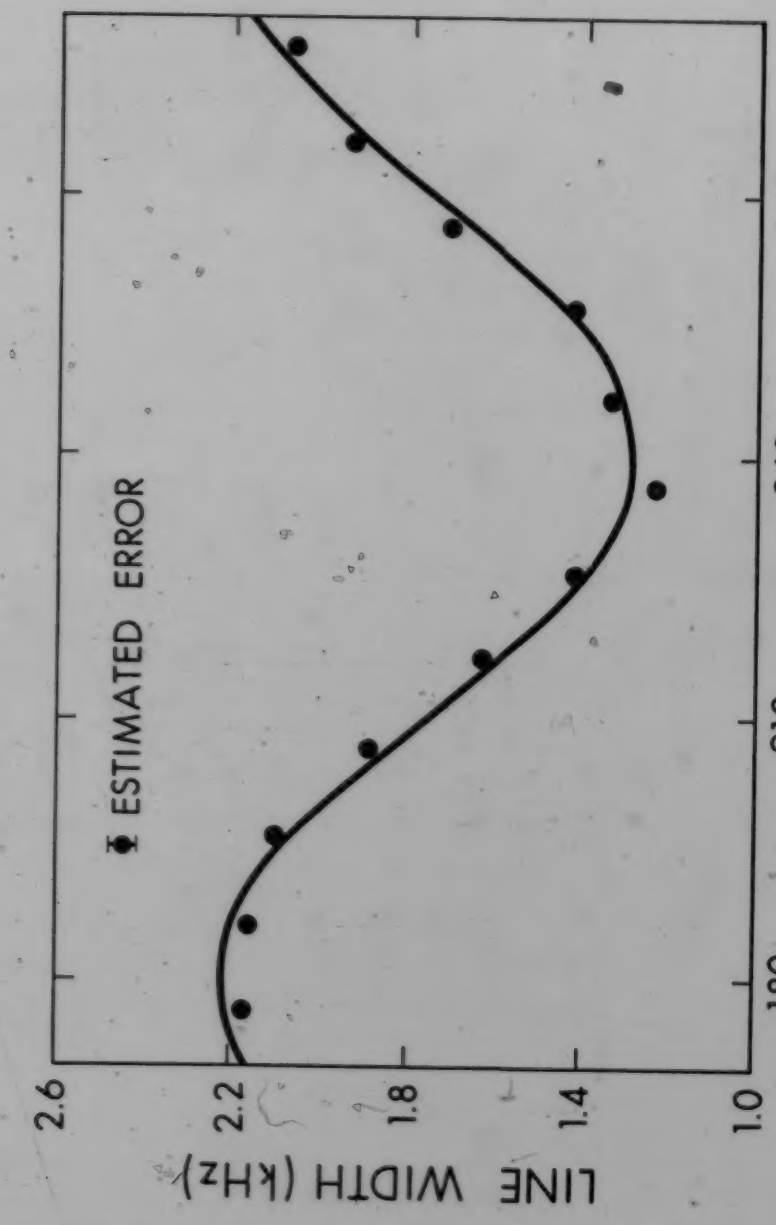
LINE WIDTH (kHz)
2.6
2.2
1.8
1.4
1.0
180
210
240
270
ANGLE φ (degrees)
ESTIMATED ERROR

Figure 6.3

Peak-to-peak linewidth of the high frequency satellite resonance for $\theta = 60°$ as a function of the angle ϕ. The solid line is a least squares fit to the expression

$$A + B \cos 3\phi.$$

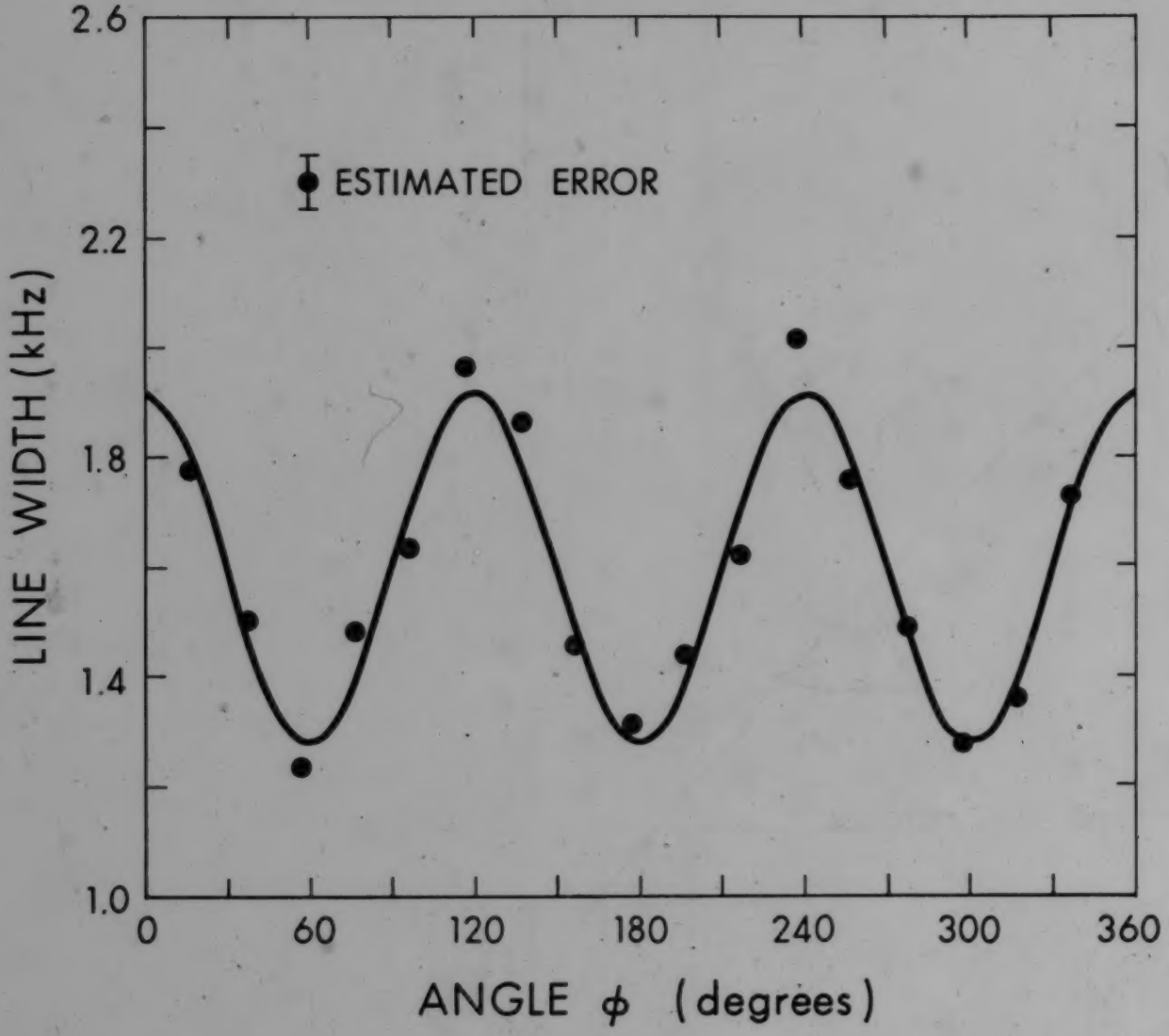
2.6
2.2
1.8
1.4
1.0
LINE WIDTH (kHz)
ESTIMATED ERROR
0
60
120
180
240
300
360
ANGLE φ (degrees)

indicates that contributions to the linewidth from lattice defects are negligible in our crystal.

6.3 Orientation dependence of W_2/W_1

The E-P_{obs} data for each crystal orientation were fitted to a straight line by a weighted least squares fit technique. The error for each point was given by the scatter of the E_i, as discussed in section 5.3.2. The goodness of fit was not used to determine the error in the intercept because, for the small number of data points used, this value is unreliable. Instead, the error was calculated using eq. (A3.3), and this error value will be quoted in all cases.

The correction for the non-infinite saturation power was determined from measurements at each crystal setting using equation (4.8) or (4.9) as appropriate. The value of the extrapolated enhancement obtained from the E-P_{obs} data was multiplied in each case by the small correction factor ξ defined by

$$\xi = \frac{\text{E at infinite saturation power}}{\text{E at the power used for the } P_{obs} \text{ data}} \quad . \qquad (6.5)$$

The parameter δ, which is required in the calculation of W_2/W_1 was determined in each case from the quadrupole splitting.

The results obtained at $\theta = 180°$ and $\phi = -3.5°$ for Cases I, II and III are given in Table I. The quantity E is the enhancement obtained by extrapolation to $P_{obs} = 0$, and $E_{corr} = \xi E$. The values of E_{corr} were used in conjunction with eqs. (4.4), (4.5) and (4.6) giving the following values:

$$\left.\begin{aligned} W_2/W_1 &= 1.024 \pm 0.006 \\ W_3/W_1 &= 0.0034 \pm 0.0011 \end{aligned}\right\} \qquad (6.6)$$

The quantity W_3/W_1 represents a small amount of magnetic relaxation occurring in the crystal, presumably due to paramagnetic impurities.

It was shown by Niemelä (1967) that W_3 for ^{23}Na in sodium nitrate depended only weakly on crystal orientation. Since W_1 also does not vary by more than ±15%, we make the simplifying assumption that y or W_3/W_1 is independent of crystal orientation. A small magnetic relaxation correction was therefore applied to all subsequent Case I measurements by using the relation:

$$x = (E-1)/[2-E-\delta-(3y/(1+x))] \; . \qquad (6.7)$$

Using the numerical values of M_{1313}/M_{1111}, M_{3333}/M_{1111} and M_{1113}/M_{1111} given by Reed (1970) the derivatives $\partial(W_2/W_1)/\partial(M_{1313}/M_{1111})$ etc. were

Table I

Enhancement measurements obtained at $\theta = 180°$

Case I

$$E = 1.4894 \pm 0.0023$$

$$\xi = 1.0023$$

$$E_{corr} = 1.4928 \pm 0.0023$$

Case II

$$E = 1.5104 \pm 0.0035$$

$$\xi = 1.0023$$

$$E_{corr} = 1.5136 \pm 0.0035$$

Case III

$$E = 1.6714 \pm 0.0019$$

$$\xi = 1.0035$$

$$E_{corr} = 1.6773 \pm 0.019$$

calculated and are shown as a function of θ in Fig. 6.4. These curves were used in choosing the θ values at which the enhancement should be measured. For example, points near $\theta = 60°$ or $120°$ are particularly useful in determining M_{1113}/M_{1111}.

The results for the θ dependence of W_2/W_1 for $\phi = -3.5°$ are shown in Table II. Unfortunately, it was discovered that the trigger level for the Misbalance Detector had not been set low enough when the separation between center line and satellite was 20 kHz. When a separate experiment was performed to measure the NMR sensitivity change which had occurred under these circumstances, it was found that all enhancement values taken at a separation of 20 kHz should be multiplied by the small correction factor 1.0023. Measurements at 40 kHz separation indicated that no significant systematic error was present. Each determination of W_2/W_1 required approximately forty-eight to sixty hours of data, depending upon the signal-to-noise ratio at the particular orientation. The results of Table II are shown graphically in Fig. 6.5, the solid line being the non-linear least squares fit to the theoretical expression eq. (3.15). In order to estimate the goodness of fit we calculated the values of χ^2 per degree of freedom, and the mean deviation defined as

$$\frac{1}{P} \sum \frac{(x_i - x_{th})}{\sigma_i} \qquad (6.8)$$

Figure 6.4

The sensitivity of W_2/W_1 to a variation of M'_{1313}, M'_{3333} or M'_{1113} as a function of the angle θ.

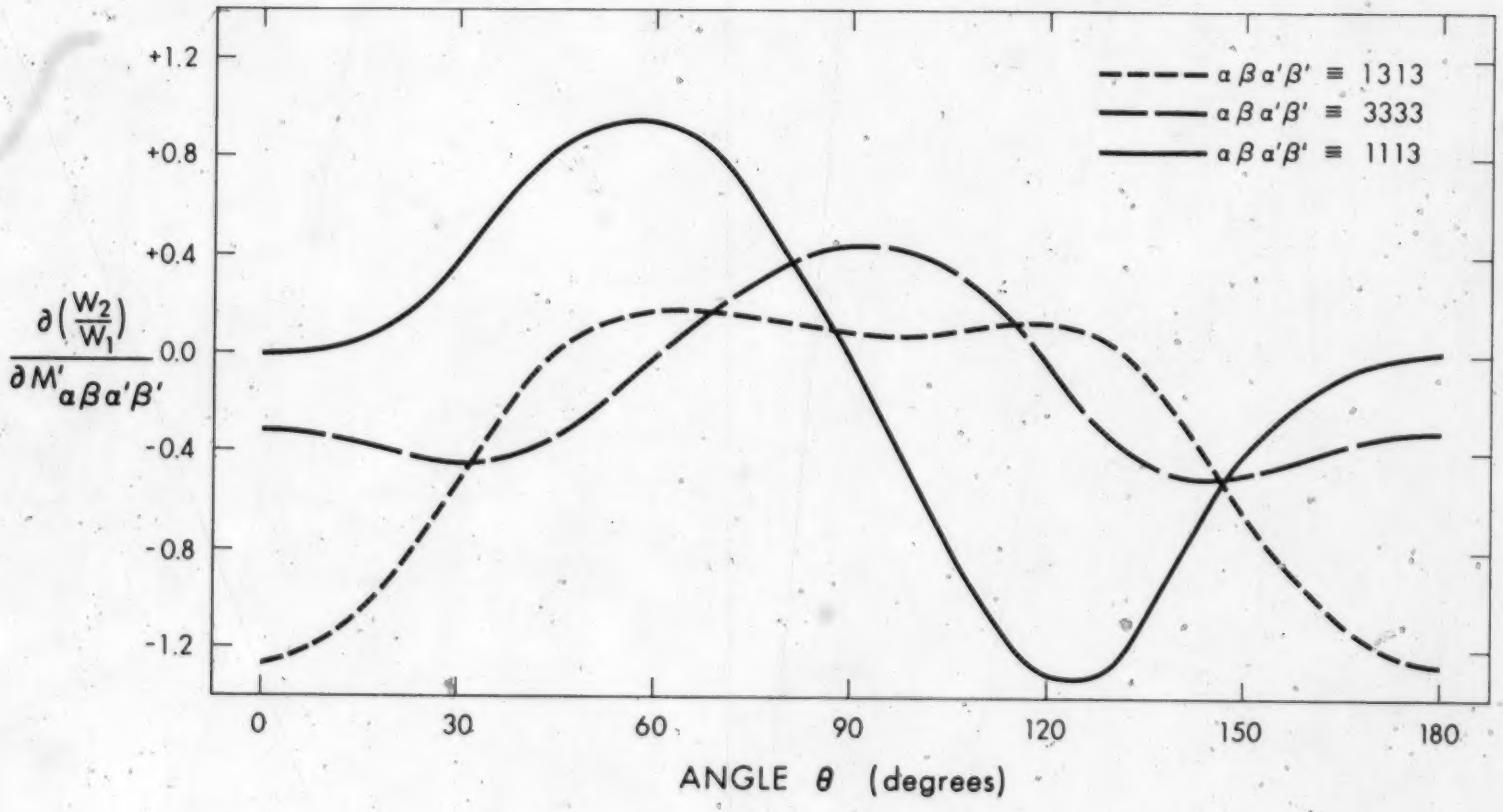
+1.2
+0.8
+0.4
0.0
-0.4
-0.8
-1.2
$\frac{\partial\left(\frac{W_2}{W_1}\right)}{\partial M'_{\alpha\beta\alpha'\beta'}}$
$\alpha\beta\alpha'\beta' \equiv 1313$
$\alpha\beta\alpha'\beta' \equiv 3333$
$\alpha\beta\alpha'\beta' \equiv 1113$
0
30
60
90
120
150
180
ANGLE θ (degrees)

Table II

The θ dependence of W_2/W_1 at $\phi = -3.5°$ for Case I

θ°	E	ξ	W_2/W_1
0.0	1.4893±0.0030	1.0016	1.022±0.012
13.0	1.4974±0.0033	1.0016	1.052±0.013
28.2	1.5069±0.0031	1.0020	1.082±0.013
43.2	1.5012±0.0033	1.0020	1.040±0.013
59.1	1.4742±0.0035*	1.0023	0.928±0.012
73.3	1.4695±0.0031	1.0015	0.846±0.011
88.4	1.4542±0.0028	1.0017	0.867±0.010
103.4	1.4806±0.0050	1.0016	0.961±0.018
113.2	1.5100±0.0022	1.0016	1.075±0.009
120.1	1.5306±0.0036*	1.0016	1.160±0.016
129.8	1.5367±0.0038*	1.0016	1.189±0.018
134.1	1.5416±0.0035	1.0025	1.228±0.017
141.1	1.5335±0.0034	1.0017	1.190±0.016
148.3	1.5208±0.0039	1.0024	1.150±0.017
163.3	1.5028±0.0040	1.0020	1.078±0.016
179.0	Mean of Cases I, II, III		1.024±0.006

* A "Misbalance" correction of 1.0023 has been applied.

Figure 6.5

The orientation dependence of W_2/W_1 as a function of the angle θ for $\phi = -3.5°$. The solid line is a least squares fit of the data to the theoretical form. The dotted line represents the results obtained by Reed (1970).

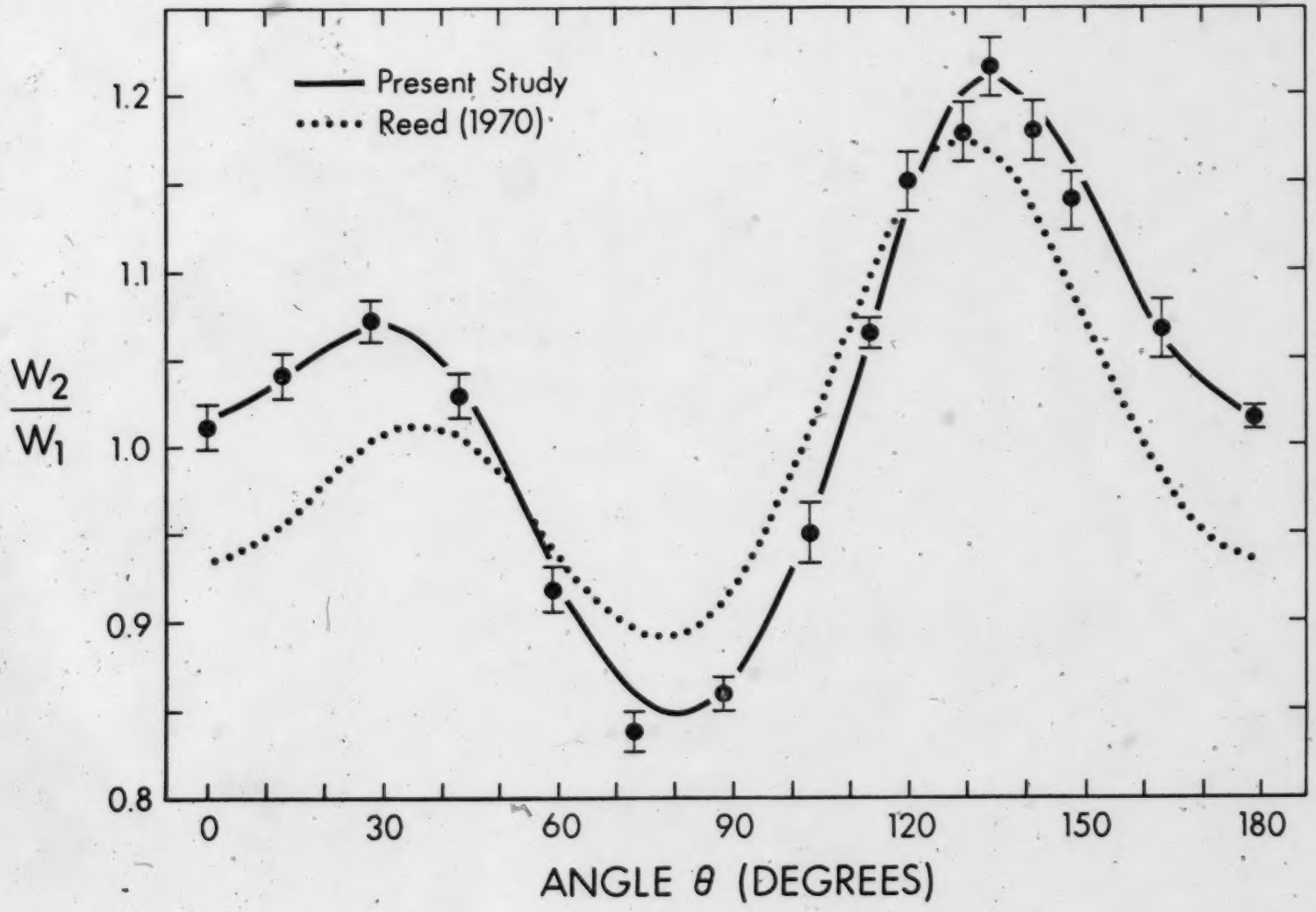
Present Study
Reed (1970)
1.2
1.1
1.0
0.9
0.8
W2/W1
0
30
60
90
120
150
180
ANGLE θ (DEGREES)

where P is the number of degrees of freedom, and x_{th} is the best fit value of x. For the data given in Table II we found

$$\chi^2 \text{ per degree of freedom} = 0.49$$

and Mean deviation $= 0.13 \pm 0.28$.

These values indicate that the theoretical form is an excellent fitting function to the data. The low value of χ^2 per degree of freedom (we would expect a value close to unity) could be interpreted as either due to good fortune or to pessimistic error limits. One possible explanation is the fact that P_{obs} was found to vary up to ±5% during the longer runs. Because of the non-zero slope of the E-P_{obs} graph this will introduce an additional random error in the E_i values. This leads in turn to a pessimistic estimate of the error in the enhancement, since in practice, we recorded P_{obs} at frequent intervals and used the mean value of P_{obs} in subsequent analysis. In other words, eq. (5.5) gives a reliable error estimate only if the observing power is essentially constant. An estimate of the magnitude of this effect shows that it is capable of explaining the low value of χ^2 per degree of freedom.

From the least squares fit to the data in Fig. 6.5 we found the following values for the fitted parameters

$$\left.\begin{aligned} M_{1313}/M_{1111} &= 0.8025 \pm 0.0025 \\ M_{3333}/M_{1111} &= 0.7091 \pm 0.0059 \\ M_{1113}/M_{1111} &= -0.1001 \pm 0.0022 \end{aligned}\right\} . \qquad (6.9)$$

In section 7.1 we estimate the magnitude of systematic errors in the determination of the enhancement in order to make a realistic estimate of the error in the above quantities.

It can be seen from Fig. 6.5 that there is a significant discrepancy between the present results and those of Reed (1970). As mention in section 5.1, the method of Reed consisted of measuring the peak-to-peak amplitude of the absorption derivative when a linear frequency sweep through the resonance was performed. To check that the discrepancy between our results and those of Reed was not due to the difference in detection methods per se, we performed a "Reed type" experiment with the present apparatus at the crystal orientation $\theta = 180°$ where the discrepancy is largest. Repetitive linear frequency sweeps were performed under the control of the computer, and the output of the ω_m lock-in detector was recorded in the Fabritek signal averager. The averaged resonances were then displayed on an X-Y recorder and the peak-to-peak resonance amplitude was measured. The data for this experiment are shown in Table III. The value of 1.4909 ± 0.0033 for E_{corr} is

Table III

The E-P_{obs} and E-P_{sat} data for Case I at $\theta = 180°$ obtained using the "first derivative" method.

P_{obs}	E
279	1.500±0.005
350	1.507±0.005
842	1.534±0.005
1124	1.546±0.005
1359	1.554±0.005

P_{sat}	E
0.36	1.178±0.005
2.25	1.401±0.005
144.0	1.507±0.005

From the least square fit $E = 1.4886 \pm 0.0033$

and $\xi = 1.0015$

Thus $E_{corr} = 1.4909 \pm 0.0033$

in excellent agreement with the value 1.4928 ± 0.0023 found previously (see Table I). Thus, we conclude that the discrepancy is not due to the use of a different measuring technique. Other explanations for the discrepancy will be discussed in section 7.3.

Because of the anomalous ϕ dependence of W_2/W_1 reported by Reed (1970), we undertook a detailed study of W_2/W_1 as a function of ϕ near $\theta = 60°$ and $120°$ where the amplitude of the ϕ dependence is largest. The results are shown in Table IV. Since the separation between the center line and the satellite line was 20 kHz for these measurements, the previously described correction of 1.0023 has been applied. The corrected results are shown graphically in Fig. 6.6. The solid line is the theoretical form calculated using the M-values found from the θ dependence. In other words, it is a "zero parameter" fit and there is no sign of any anomaly in the ϕ dependence. The value of χ^2 per degree of freedom is 0.73 and the mean deviation, defined in eq. (6.8), is 0.04 ± 0.29. We again find that χ^2 per degree of freedom is substantially less than unity, thereby confirming our suspicion that the error limits are pessimistic on account of the variation in P_{obs}.

Table IV

The ϕ dependence of W_2/W_1 at $\theta = 120.1°$ for Case I

$\phi°$	E*	ξ	W_2/W_1
-3.5	1.5271±0.0036	1.0016	1.160±0.016
26.5	1.4951±0.0033	1.0018	1.020±0.013
56.5	1.4722±0.0033	1.0026	0.935±0.012
86.5	1.4909±0.0034	1.0017	1.001±0.013
116.5	1.5235±0.0030	1.0015	1.143±0.013
146.5	1.5011±0.0024	1.0018	1.045±0.010
176.5	1.4718±0.0039	1.0029	0.936±0.014
206.5	1.4902±0.0036	1.0018	1.000±0.014
236.5	1.5219±0.0034	1.0019	1.138±0.015
266.5	1.5003±0.0037	1.0018	1.042±0.015
296.5	1.4660±0.0034	1.0028	0.911±0.012
326.5	1.4921±0.0035	1.0019	1.009±0.014

* A "Misbalance" correction of 1.0023 has been applied.

Figure 6.6

The orientation dependence of W_2/W_1 as a function of the angle ϕ for $\theta = 120.1°$. The solid line represents the theoretical prediction.

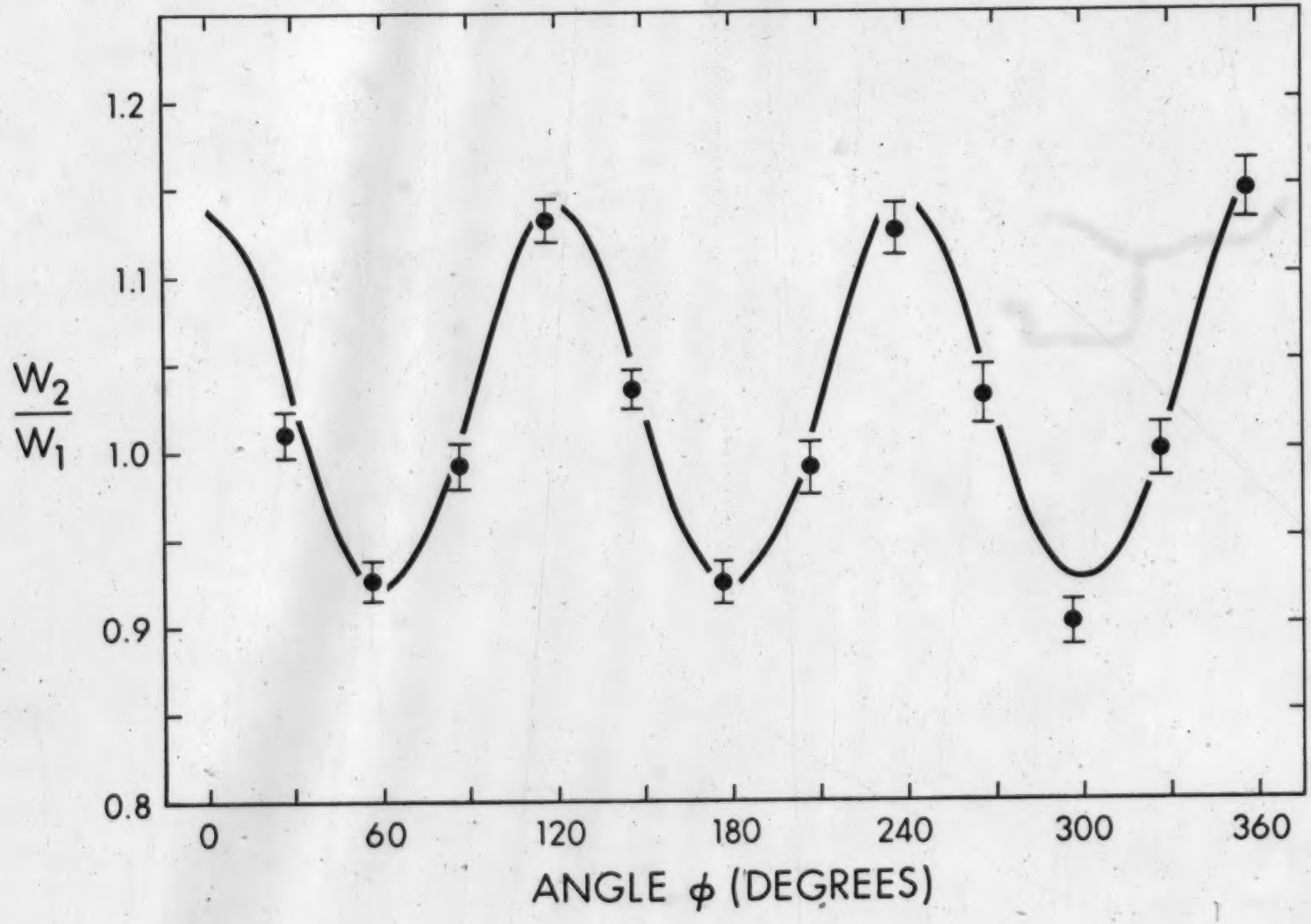
1.2
1.1
1.0
0.9
0.8
$\frac{W_2}{W_1}$
0
60
120
180
240
300
360
ANGLE ϕ (DEGREES)

In order to check the consistency of our results, we have undertaken some measurements on the second crystal of sodium nitrate discussed in section 5.7. Results obtained at the orientation $\theta = 0°$ for Cases I to IV are given in Table V. Using eqs. (4.4) to (4.7), we obtain the values:

$$\left.\begin{aligned} W_2/W_1 &= 1.020 \pm 0.004 \\ W_3/W_1 &= 0.0097 \pm 0.0010 \end{aligned}\right\} . \qquad (6.10)$$

Comparison of eqs. (6.6) and (6.10) shows good agreement between the W_2/W_1 results obtained with both crystals. The magnetic relaxation contribution W_3/W_1 is approximately three times greater in the second crystal than in the first. This presumably is an indication that the paramagnetic impurity concentration is not identical in the two crystals.

6.4 Measurement of W_1 by the transient method

In order to obtain a value of W_1, we measured the time dependence of the amplitude of the low frequency satellite at $\theta = 180°$ after removal of the saturation power from the center line (as described in section 5.6). This was repeated at various values of P_{obs}. In order that the data could be reasonably fitted to a single exponential (see section 4.2) all

Table V

Enhancement measurements obtained at $\theta = 0°$ using the second sodium nitrate crystal.

Case I

$E = 1.4859 \pm 0.0030$

$\xi = 1.0017$

$E_{corr} = 1.4884 \pm 0.0030$

Case II

$E = 1.5015 \pm 0.0028$

$\xi = 1.0017$

$E_{corr} = 1.5040 \pm 0.0028$

Case III

$E = 1.6568 \pm 0.0025$

$\xi = 1.0017$

$E_{corr} = 1.6596 \pm 0.0025$

Case IV

$E = 1.6367 \pm 0.0025$

$\xi = 1.0016$

$E_{corr} = 1.6931 \pm 0.0025$

the P_{obs} values were small. As expected, the signal-to-noise ratios were poor, thereby requiring many hours of data collection. A typical example of a twelve-hour run is shown in analogue form in Fig. 6.7.

The usual method for analyzing an exponential decay is to take the logarithm of the data before fitting to a straight line. The value of the baseline of the data is then adjusted to minimize χ^2. This method is only applicable if the noise is small compared with the signal. A systematic error in the determination of the decay constant would otherwise occur since the error bars would be asymmetric after taking the logarithm. A more satisfactory method is to use a non-linear least squares technique by fitting the original data to the theoretical form

$$A + B \exp(-\lambda t) .$$

In this method, there is no restriction on the signal-to-noise ratio of the data, and no systematic error should occur. Consequently, all the data collected is usable, including that in the "tail" of the decay.

We used such a non-linear least squares fit method to analyze all of our numerical data, and the decay constant λ is shown as a function of P_{obs} in Table VI and in graphical form in Fig. 6.8. According to eq. (4.11), λ should be a linear function of P_{obs},

Figure 6.7

The recovery to equilibrium of the high frequency satellite after removal of the saturation power from the center line. The trace represents 12 hours of data collection at a low value of P_{obs}.

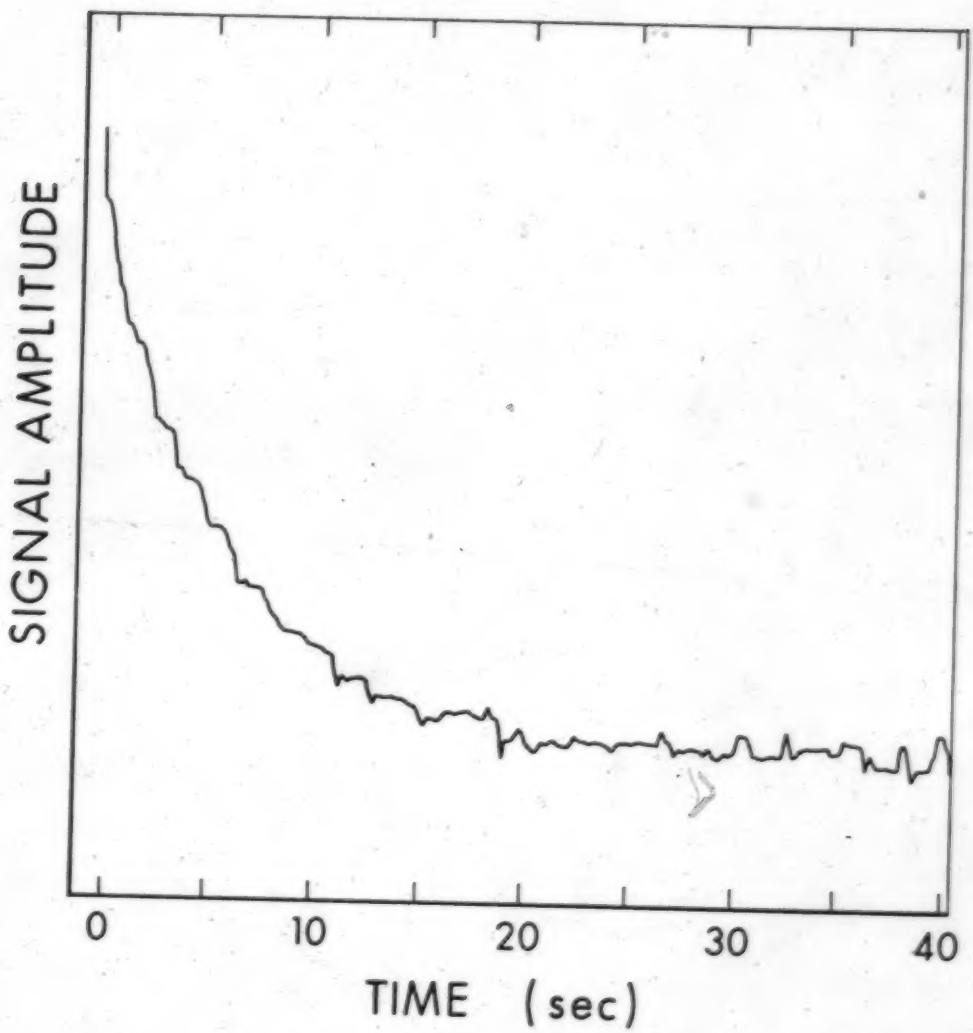
SIGNAL AMPLITUDE
0
10
20
30
40
TIME (sec)

Table VI

The decay constant λ as a function of P_{obs} obtained at $\theta = 180°$.

P_{obs}	λ sec^{-1}
155	0.1683±0.0020
219	0.1714±0.0012
309	0.1677±0.0021
360	0.1724±0.0016
512	0.1683±0.0020
767	0.1741±0.0021
962	0.1789±0.0013
1154	0.1853±0.0015

Least squares fit value of the intercept = 0.1622±0.0017 sec^{-1}.

and the solid line in Fig. 6.8 is a weighted least squares fit to that theoretical form. The intercept is equal to

$$0.1622 \pm 0.0017 \text{ sec}^{-1} .$$

In this case, the standard error is given by the goodness of fit, since the fit is not quite as good as one would expect from the errors of the individual data points. This discrepancy may be due to the approximation of fitting the decay to only one exponential, or it may be due to small variations in spectrometer level during an individual run.

The value of the intercept is used in conjunction with eq. (4.12) to determine W_1. Using the previously determined value $y = 0.0034 \pm 0.0011$, we find

$$\begin{aligned} W_1 &= (8.032 \pm 0.0084) \times 10^{-2} \text{ sec}^{-1} \\ W_3 &= (2.7 \pm 0.9) \times 10^{-4} \text{ sec}^{-1} . \end{aligned} \tag{6.11}$$

Inspection of eq. (3.12) shows that only at $\theta = 0$ or $180°$ is W_1 a function of just one M-component. Thus, we can deduce immediately that:

$$e^2Q^2M_{1313} = (4.819 \pm 0.050) \times 10^{-1} \text{ sec}^{-1} . \tag{6.12}$$

The smallness of the magnetic relaxation contribution can be appreciated by noting that if this

Figure 6.8

The variation of the decay constant λ as a function of spectrometer power P_{obs}. The solid line is a least squares fit to a linear form.

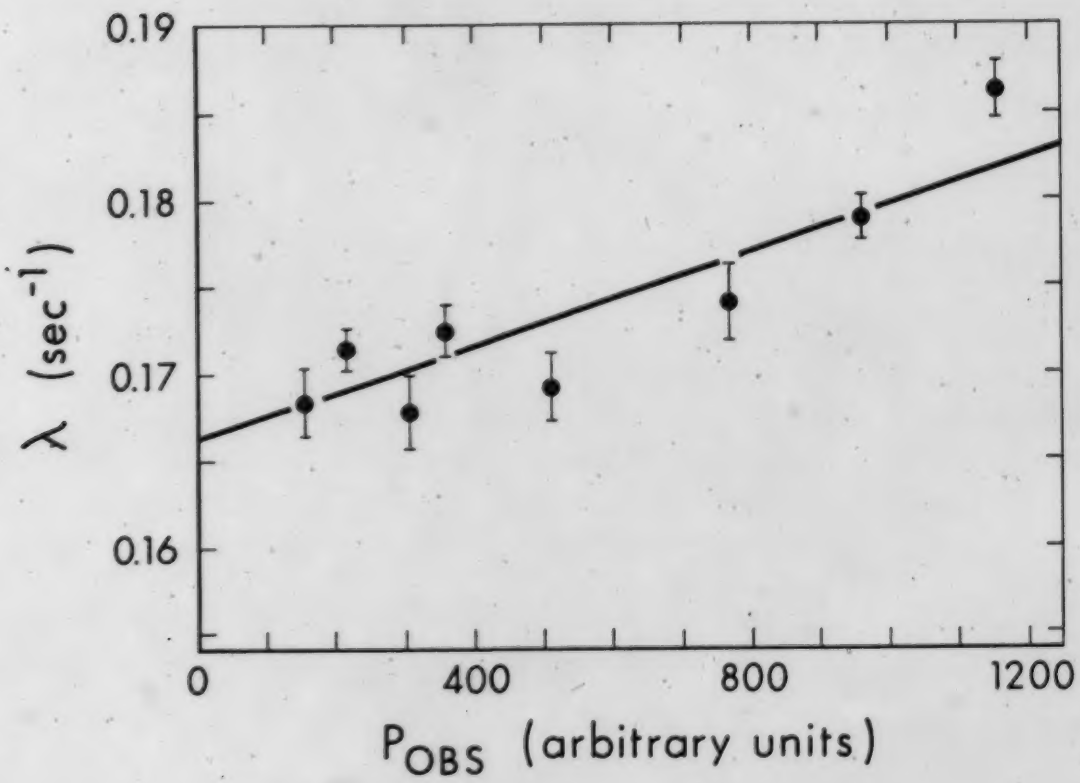
0.19
0.18
0.17
0.16
λ (sec⁻¹)
0
400
800
1200
P_OBS (arbitrary units)

were the only relaxation process, the spin-lattice relaxation time for the satellite line would be approximately 20 minutes instead of 6 seconds!

CHAPTER VII

DISCUSSION OF THE RELAXATION MEASUREMENTS

7.1 Estimation of systematic errors in the relaxation data

From Tables II and IV we see that a typical random error in the extrapolated enhancement is 0.2%. Thus, we need only consider systematic errors greater than about 0.01%. Of the systematic errors considered in section 5.4, we find that the only significant ones are of instrumental origin, which we shall now discuss.

The trigger level for the "Misbalance detector" was set at a level which corresponds to no more than a 0.05% NMR sensitivity change. (The only exception was when the saturation and observing frequencies differed by 20 kHz; a separate correction was applied for this case, as indicated in section 6.3.) We estimate that the systematic error in the enhancement caused by this source is about 0.03%, since the misbalance signal is near the 0.05% trigger level only a small fraction of the time.

Since noise is random, there is a finite probability of it exceeding the dynamic range of the signal processing circuitry, however small the standard deviation of the noise. As mentioned in section 5.4.3,

this problem is most serious in the circuitry just prior to the correlator in the lock-in detectors. Using the graphs given by Cohn (1964), in conjunction with a knowledge of typical signal plus noise levels in our amplifiers, we estimate that the systematic error from this cause is no more than 0.05%.

The A/D converter in our system has a maximum non-linearity of one half a bit and a resolution of twelve bits. For the typical signal levels measured, this corresponds to a maximum systematic error of approximately 0.05%.

We now consider the magnitude of any residual systematic error caused by the mixing of the rf and modulation related signals. The two-week check mentioned in section 5.4.3 revealed no significant systematic error. Since a typical enhancement measurement required forty-eight hours of data, we estimate any residual error to be less than 0.35 (i.e. $\sqrt{2/14}$) of the random error in an enhancement measurement. This corresponds to a 0.07% error.

We have discussed in section 5.4.3 the frequency-dependent systematic error which we believe is due to stray signals at the spectrometer frequency being amplified by the rf power source and reentering the spectrometer via the saturation coils. Since this systematic error was observed to decrease with decreasing

P_{obs}, the error in the extrapolated enhancement should be no larger than about 0.07%.

The first two systematic errors discussed here will lead to enhancement values which are too low. However, the remaining errors could be of either sign. We therefore combine the errors in the usual way to find a probable systematic error in the extrapolated enhancement of about 0.15%. If this systematic error is uncorrelated from point to point, then the "goodness of fit" error limits on the ratios of the M-components should include the effects of these uncorrelated systematic errors. However, the systematic error is, by its very nature, likely to be correlated from point to point. To take this into account, we increase the error limits given in eq. (6.9) and our final estimate of the ratios of the M-components is

$$\left.\begin{aligned} M_{1313}/M_{1111} &= 0.8025 \pm 0.0035 \\ M_{3333}/M_{1111} &= 0.7091 \pm 0.0083 \\ M_{1113}/M_{1111} &= -0.1001 \pm 0.0031 \end{aligned}\right\} . \qquad (7.1)$$

The good agreement between the W_2/W_1 values obtained with the first and second sodium nitrate crystals, indicates firstly that this quantity does not appear to be sample dependent. Secondly, since the second crystal is considerably larger than the

first, it shows that any systematic errors associated with sample size are negligible. Possible size dependent errors could be caused by large inhomogeneities in the rf fields or weak background NMR signals emenating from the probe.

We shall now consider possible systematic errors in the determination of the decay constant λ by the transient method. Unlike pulsed NMR experiments in which the spectrometer has to recover from an extremely large overloading of the input stage, our method does not suffer from such transients. Thus, shifts in the baseline of the data are not likely to be a significant problem. Also, the NMR information appears as a small modulation of an rf carrier. Thus, linearity problems in the detectors will not be significant. The finite bandwidth of the detection system can introduce a systematic error in the determination of the decay constant. The low-pass filter following the $2\omega_m$ lock-in detector had a time constant of 0.03 seconds (corresponding to a 3 db frequency of 5 Hz). Since this time constant is so much shorter than the 6 second time constant of the observed decay, it is clear that this systematic error should be negligible.

7.2 Comparison of the W_2/W_1 results with theoretical predictions

The excellent agreement between the θ and ϕ dependence of W_2/W_1 and eq. (3.15) confirms the validity of the theoretical treatment of the orientation dependence of W_1 and W_2. It also shows that the M-components which occur in W_1 are equal to those in W_2. In turn, this implies that the spin-lattice relaxation is predominantly caused by a multiphonon interaction.

It was found (Satoh, 1965) that spin-lattice relaxation caused by vacancy diffusion becomes significant at elevated temperatures (>400 K) in sodium chloride. They therefore consider the possibility that such a mechanism could contribute to the ^{23}Na spin-lattice relaxation in sodium nitrate at room temperature. It was shown by Snyder and Hughes (1971) that the M-tensor components for this mechanism can be expressed as

$$M_{\alpha\beta\alpha'\beta'} = \overline{V_{\alpha\beta}(t)V_{\alpha'\beta'}(t)}\; 2\tau_c\{1+(E_{m+\mu}-E_m)^2\,\tau_c^2/\hbar^2\}^{-1} \qquad (7.2)$$

where $V_{\alpha\beta}(t)$ is a time dependent field gradient component, the bar signifies an ensemble average, and τ_c is the correlation time characterizing the diffusion. In the long correlation time limit

$$(E_{m+\mu} - E_m)^2 \tau_c^2 / \hbar^2 \gg 1 \qquad (7.3)$$

or in our case

$$\tau_c^2 \gg 10^{-14} \text{ sec}^2 \quad , \qquad (7.4)$$

we see from equation (7.2) that the M-tensor components governing W_2 are approximately one quarter of those governing W_1. Diffusion narrowing of the ^{23}Na resonance in sodium nitrate occurs near 500 K (Andrew et al, 1962). This implies that the correlation time of self-diffusion of the ^{23}Na ions is $\sim 10^{-3}$ seconds at this temperature. While the correlation time deduced from motional narrowing is not necessarily identical to τ_c which occurs in eq. (7.2), it seems clear that eq. (7.4) is well satisfied for sodium nitrate at room temperature. Since the mean deviation, defined in eq. (6.8), is

$$0.13 \pm 0.28$$

for the θ dependence of W_2/W_1, it follows that the "diffusional" contribution is no more than about 0.4% of W_1, or about 3×10^{-4} s^{-1}, in our crystal.

We now compare the experimental M'-values with the predictions of the point charge model described in Appendix II. Figs. 7.1 to 7.3 show the M'-components for a "linear" process as a function of the angle Θ of the parameter k describing the asymmetry of the nuclear

Figure 7.1

Point charge model estimate of M_{1313}/M_{1111} for a "linear" process. The horizontal line is the experimentally obtained value.

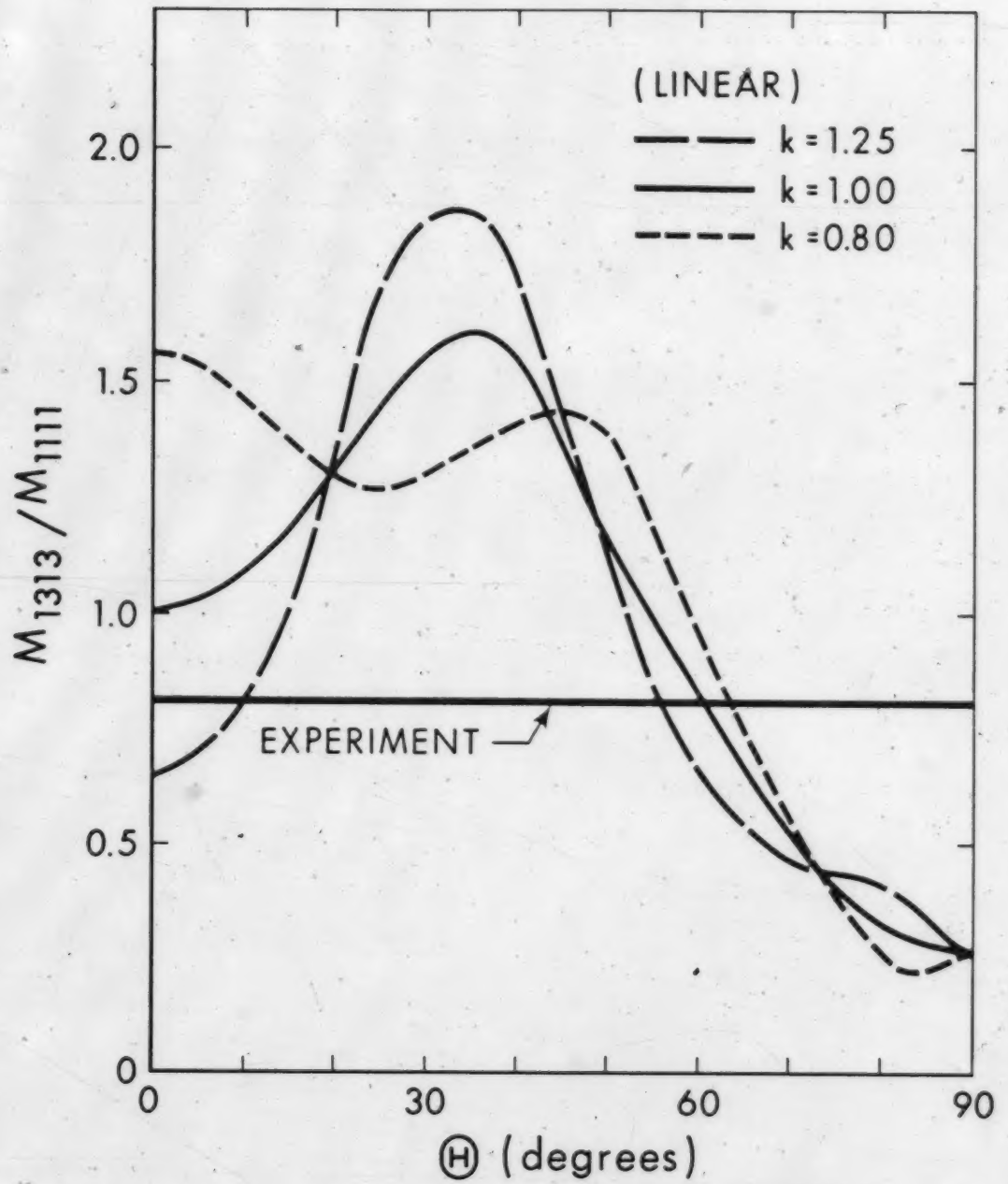
(LINEAR)
k = 1.25
k = 1.00
k = 0.80
EXPERIMENT
2.0
1.5
1.0
0.5
0
0
30
60
90
M_{1313}/M_{1111}
Θ (degrees)

Figure 7.2

Point charge model estimate of M_{3333}/M_{1111} for a "linear" process. The horizontal line is the experimentally obtained value.

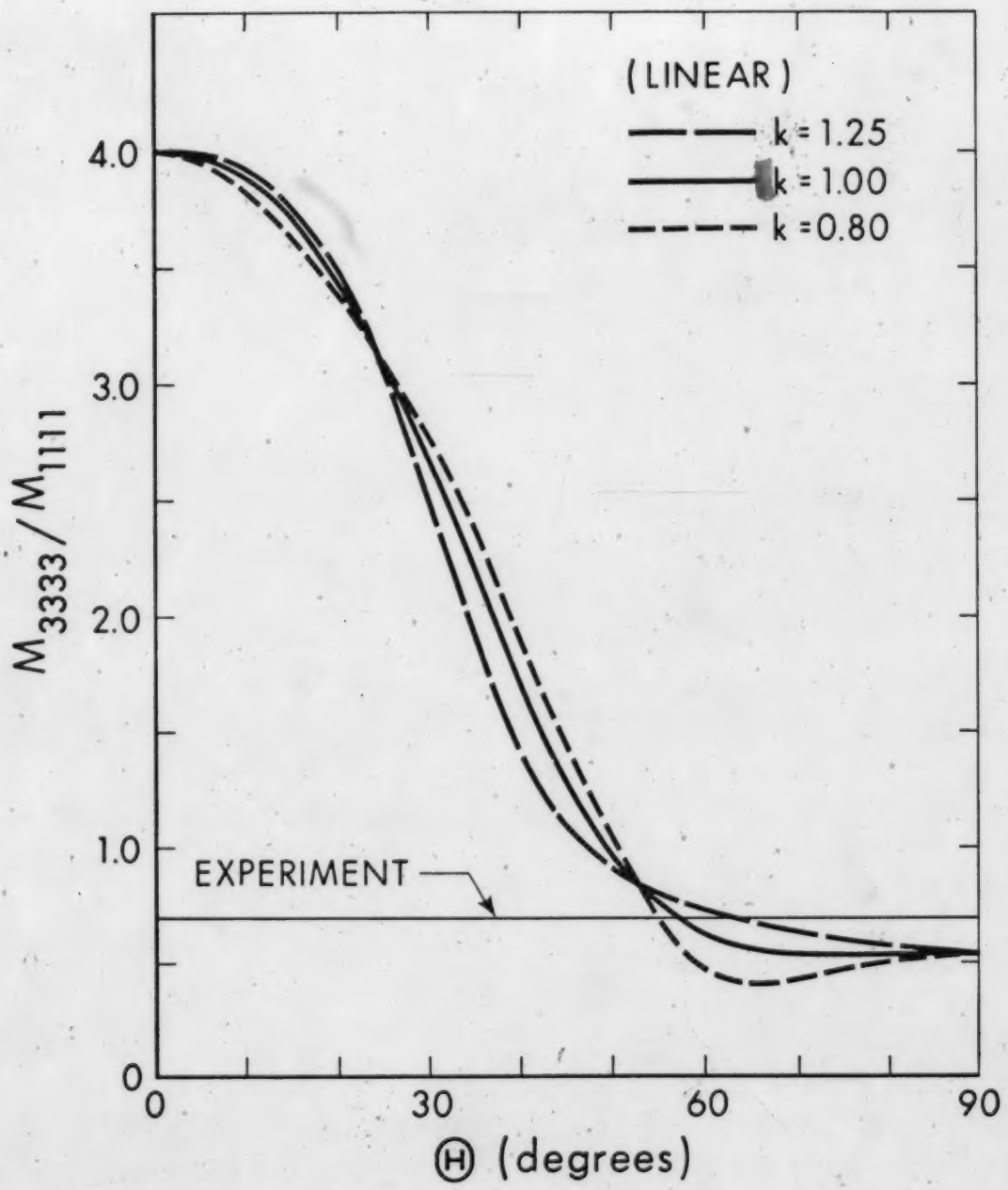
(LINEAR)
k = 1.25
k = 1.00
k = 0.80
EXPERIMENT
M_{3333}/M_{1111}
4.0
3.0
2.0
1.0
0
0
30
60
90
Θ (degrees)

Figure 7.3

Point charge model estimate of M_{1113}/M_{1111} for a "linear" process. The horizontal line is the experimentally obtained value.

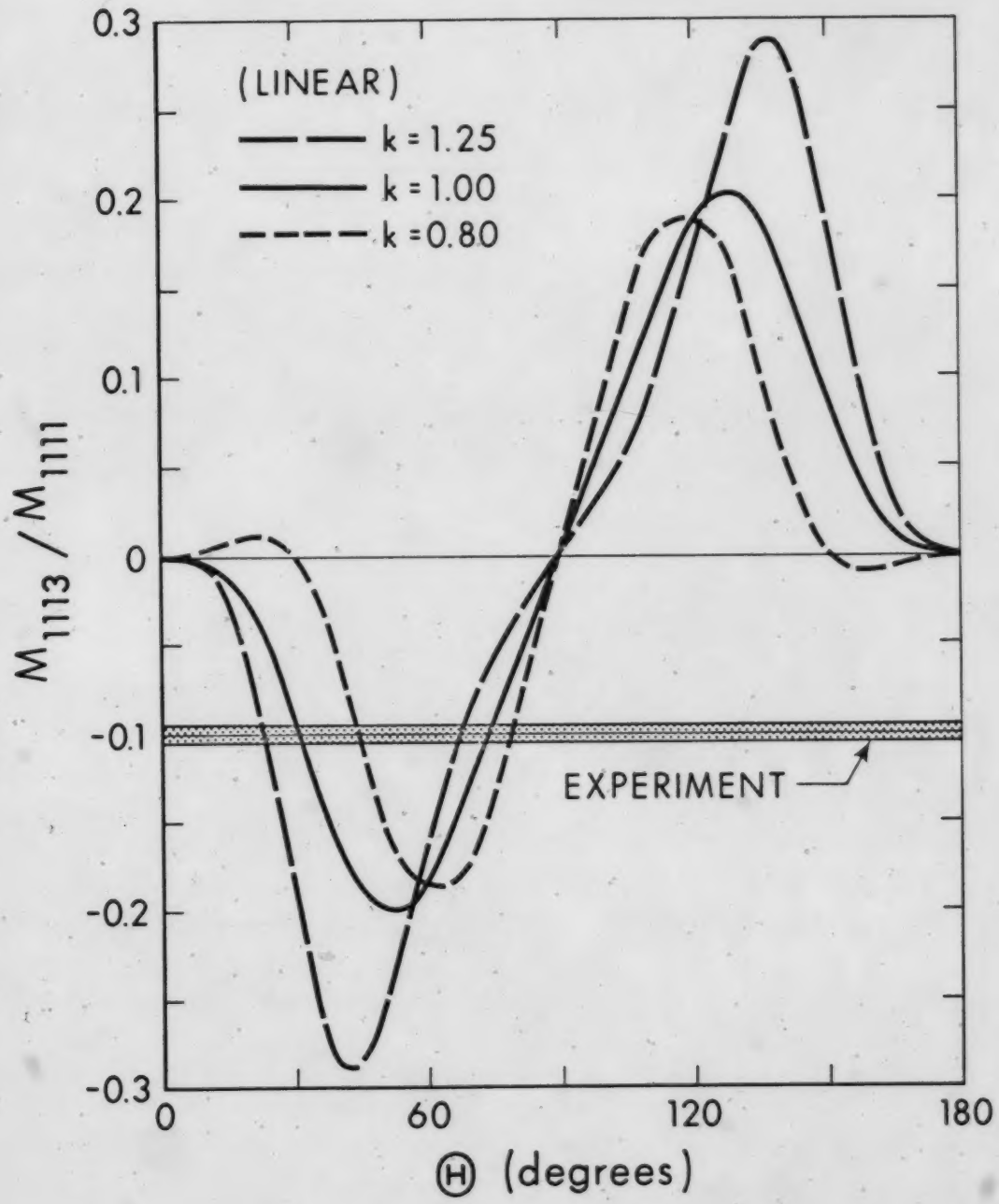
0.3
0.2
0.1
0
-0.1
-0.2
-0.3
(LINEAR)
k = 1.25
k = 1.00
k = 0.80
EXPERIMENT
M_{1113} / M_{1111}
0
60
120
180
Θ (degrees)

vibration. It can be seen from these diagrams that the M' values are determined primarily by Θ rather than k. In sodium nitrate the angle Θ is 54.5° at room temperature (Cherin et al, 1967). From the neutron diffraction study of Paul and Pryor (1971) we deduce that the parameter k is roughly 1.05. Thus, we can see that for M'_{1313} and M'_{3333} the agreement between theory and experiment is surprisingly good. However, unless we assume values of k which differ greatly from unity, agreement for M'_{1113} is poor. In Figs. 7.4 to 7.6 are shown the M'-components for a "quadratic" process. Again the agreement is excellent for M'_{1313} and M'_{3333}, but we now obtain good agreement for M'_{1113}. Thus, it is tempting to conclude that in sodium nitrate the dominant relaxation mechanism is a "quadratic" one at room temperature. (This presumably would be the harmonic Raman process considered by Van Kranendonk (1954), since the anharmonic process (Van Kranendonk and Walker, 1967, 1968) is "linear.) This point will be discussed further in section 7.4 when we discuss data taken at 77 K.

The theoretical estimates of Van Kranendonk and Walker (1967, 1968) indicate that the anharmonic Raman process is roughly two orders of magnitude more important than the harmonic Raman process.

Figure 7.4

Point charge model estimate of M_{1313}/M_{1111} for a "quadratic" process. The horizontal line is the experimentally obtained value.

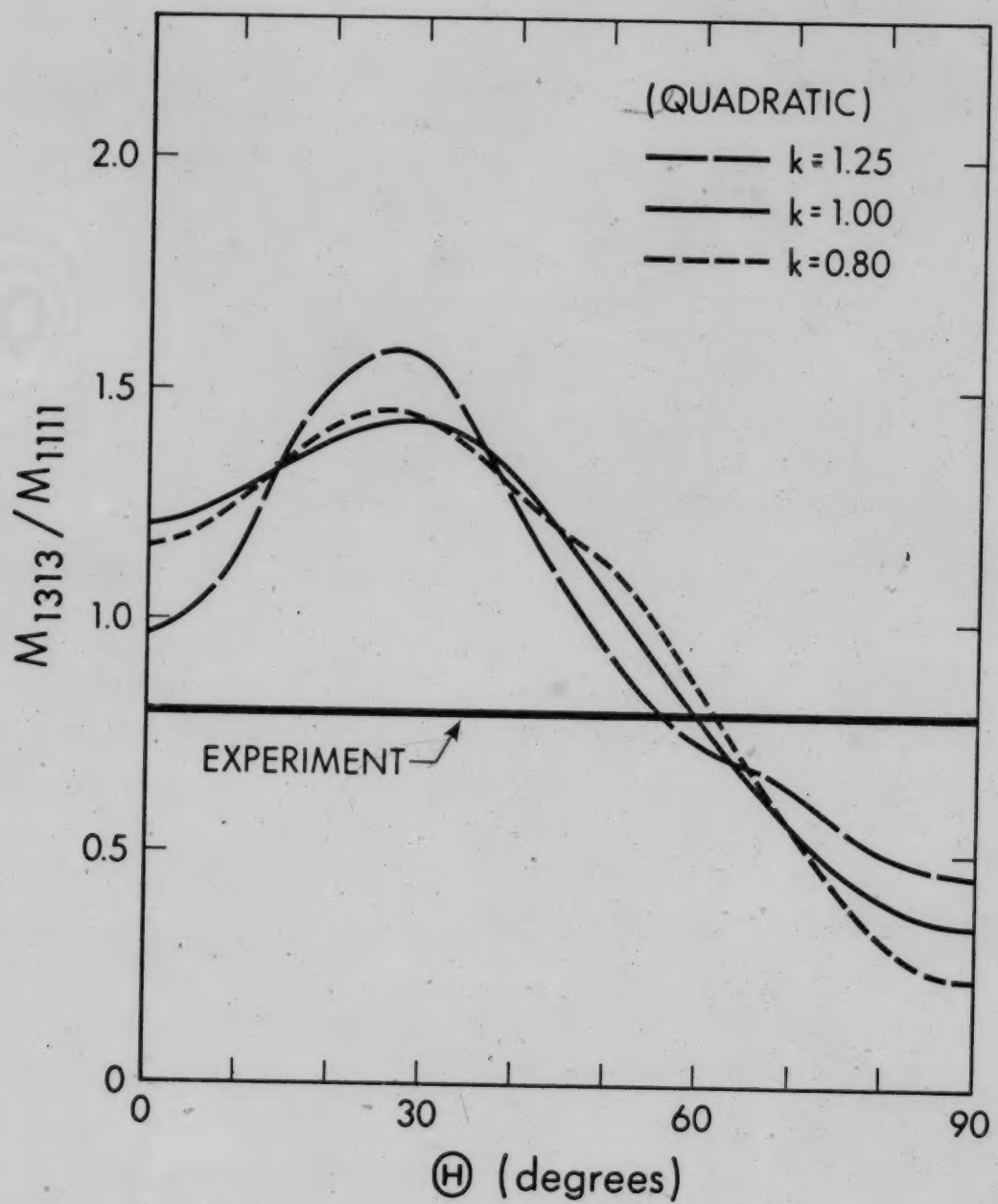
(QUADRATIC)
k = 1.25
k = 1.00
k = 0.80
EXPERIMENT
M_{1313} / M_{1111}
2.0
1.5
1.0
0.5
0
0
30
60
90
Θ (degrees)

Figure 7.5

Point charge model estimate of M_{3333}/M_{1111} for a "quadratic" process. The horizontal line is the experimentally obtained value.

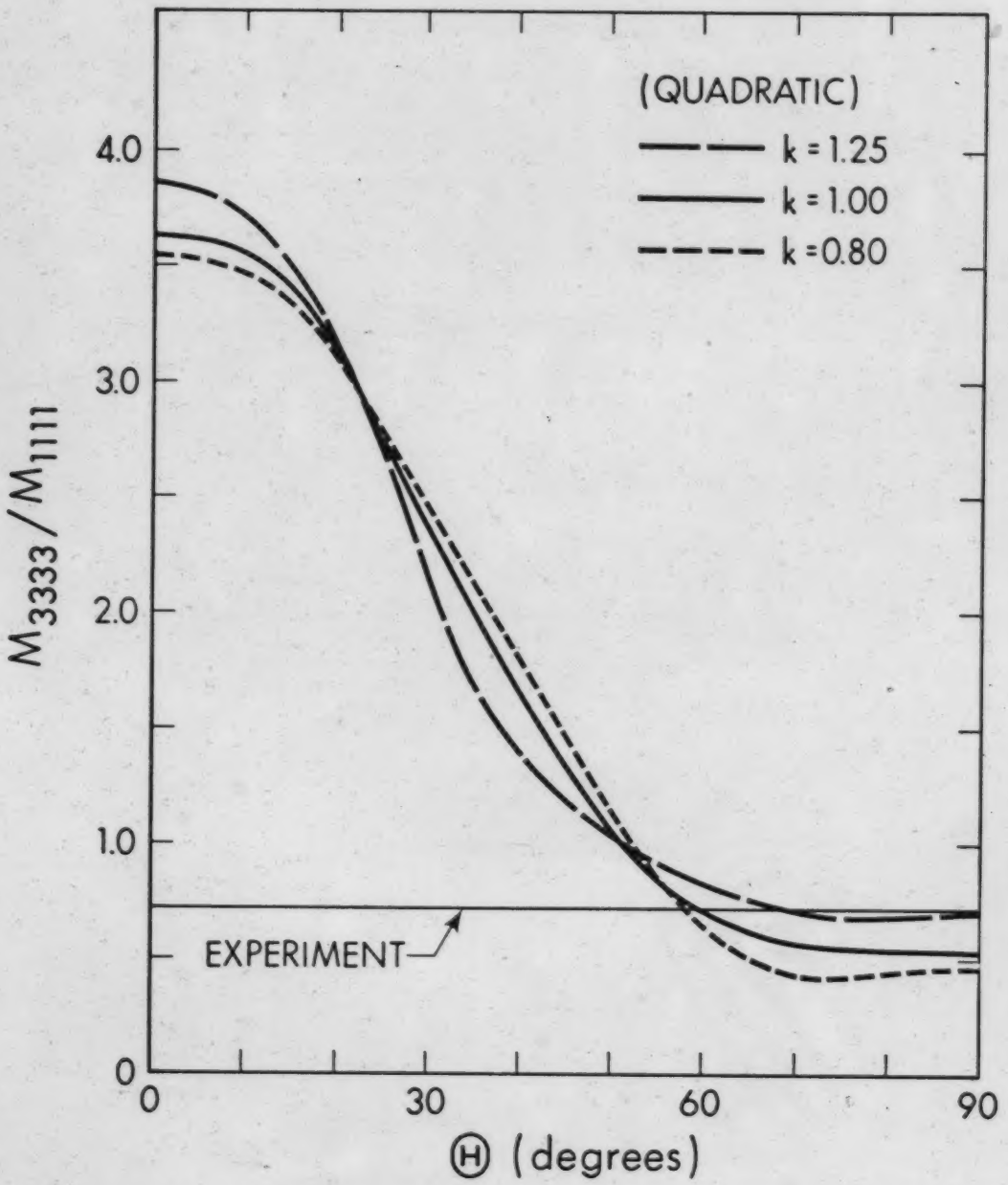
(QUADRATIC)
k = 1.25
k = 1.00
k = 0.80
4.0
3.0
2.0
1.0
0
M_{3333}/M_{1111}
EXPERIMENT
0
30
60
90
Ⓗ (degrees)

Figure 7.6

Point charge model estimate of M_{1113}/M_{1111} for a "quadratic" process. The horizontal line is the experimentally obtained value.

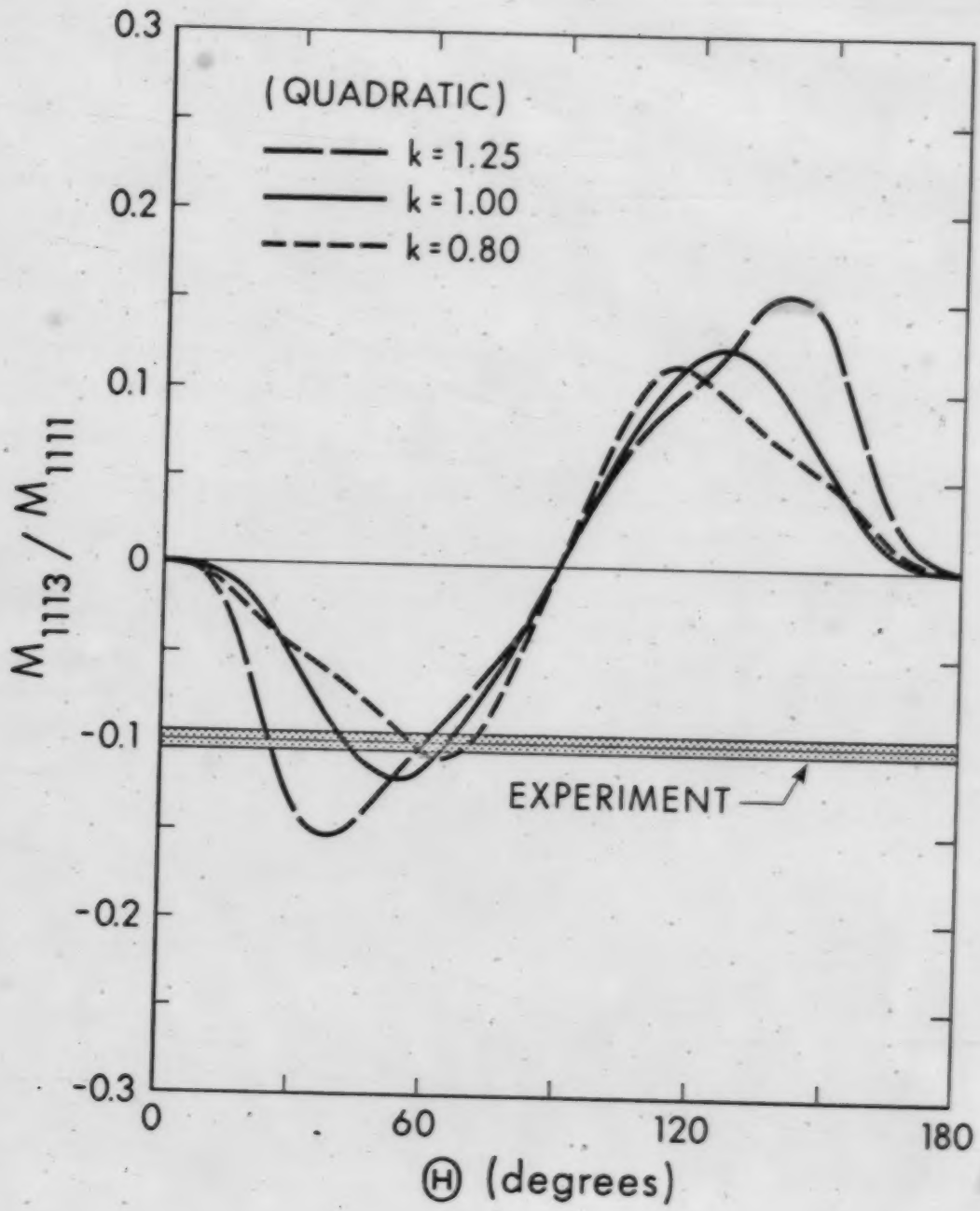
(QUADRATIC)
k = 1.25
k = 1.00
k = 0.80
EXPERIMENT
M_{1113} / M_{1111}
Ⓗ (degrees)
0.3
0.2
0.1
0
-0.1
-0.2
-0.3
0
60
120
180

However, subsequent more detailed calculations by Pietilä (1974) have shown that the two processes may be equally important for ^{23}Na in sodium chloride at room temperature. Thus, the theoretical situation is by no means clear.

7.3 Comparison with previous room temperature results

The original enhancement measurements on sodium nitrate were performed by Pound (1950). The precision of his measurements was sufficient to demonstrate that a quadrupole spin-lattice relaxation mechanism was dominant in sodium nitrate. Furthermore, he showed that W_2/W_1 was the order of unity at the crystal orientation $\theta = 0°$.

Sarnatskii and Shutilov (1972) have performed a double resonance experiment on sodium nitrate by using acoustic saturation of a pair of energy levels separated by $\Delta m = \pm 2$. The resonance enhancement was measured by a steady-state technique using a Robinson spectrometer. They also performed a pulsed NMR experiment in order to obtain an estimate of W_1. Sarnatskii and Shutilov found that

$$\left.\begin{aligned} W_2/W_1 &= 1.6 \pm 0.4 \\ W_1 &= 0.066 \text{ sec}^{-1} \\ W_3 &= 0.0023 \text{ sec}^{-1} \end{aligned}\right\} \qquad (7.5)$$

at the crystal orientation $\theta = 30°$ or $150°$. (The authors did not distinguish between these two values; neither did they quote the angle ϕ.) Sarnatskii and Shutilov estimated the paramagnetic impurity concentration in their sample to be $\sim$1 part in 10^5 on the basis of electron paramagnetic resonance measurements. By inspection of Fig. 6.5 it can be seen that tolerable agreement for W_2/W_1 is obtained if we assume that their data were obtained at $\theta = 150°$ and ϕ near zero. Similarly, their estimation of W_1 is in fair agreement with our value of $(8.032 \pm 0.084) \times 10^{-2}$ s^{-1}. Lastly, their estimate of W_3 is an order of magnitude larger than our value (see eq. (6.11)). However, this is reasonable since our paramagentic impurity concentration is believed to be less than 1 part in 10^6.

Reed (1970) measured the orientation dependence of W_2/W_1 of ^{23}Na in sodium nitrate at room temperature. It is of interest to compare these results with ours given in eq. (7.1), since both studies were made on the same sample. The ratios of the M-components given by Reed (1970) and Hughes and Reed (1971) are

$$\left.\begin{aligned} M_{1313}/M_{1111} &= 0.850 \pm 0.015 \\ M_{3333}/M_{1111} &= 0.822 \pm 0.016 \\ M_{1113}/M_{1111} &= -0.120 \pm 0.018 \\ M_{1123}/M_{1111} &= 0.142 \pm 0.017 \end{aligned}\right\} . \qquad (7.6)$$

We can see that the results are in poor agreement, especially for M_{1123}/M_{1111} which we found to be zero and which should be zero on grounds of crystal symmetry.

In order to explain the difference between the two sets of data, we refer first to the θ dependence of W_2/W_1 displayed in Fig. 6.5. In this figure the dotted line is the least squares fit to Reed's data. It is obvious that there is quite a large discrepancy especially near $\theta = 0°$ and 180°. Although Reed employed a different detection method as described in section 5.1, the results presented in section 6.3 indicate that the discrepancy cannot be attributed to this. In view of the considerable difficulty we experienced in eliminating systematic errors from our measurement system, we are led to consider the possibility of some undetected systematic errors in Reed's measurements. This suspicion is reinforced by the following evidence. Some W_2/W_1 values were obtained with our system before the elimination of the systematic errors caused by the interaction of the rf and modulation-related signals. Those obtained near $\theta = 0°$ were in fairly good agreement with those of Reed!

The discrepancy in the W_2/W_1 measurements is displayed in a slightly different form in Fig. 7.7.

Figure 7.7

Discrepancy between Reed's W_2/W_1 data and the present data, as a function of the difference between the observing and saturation frequencies used by Reed.

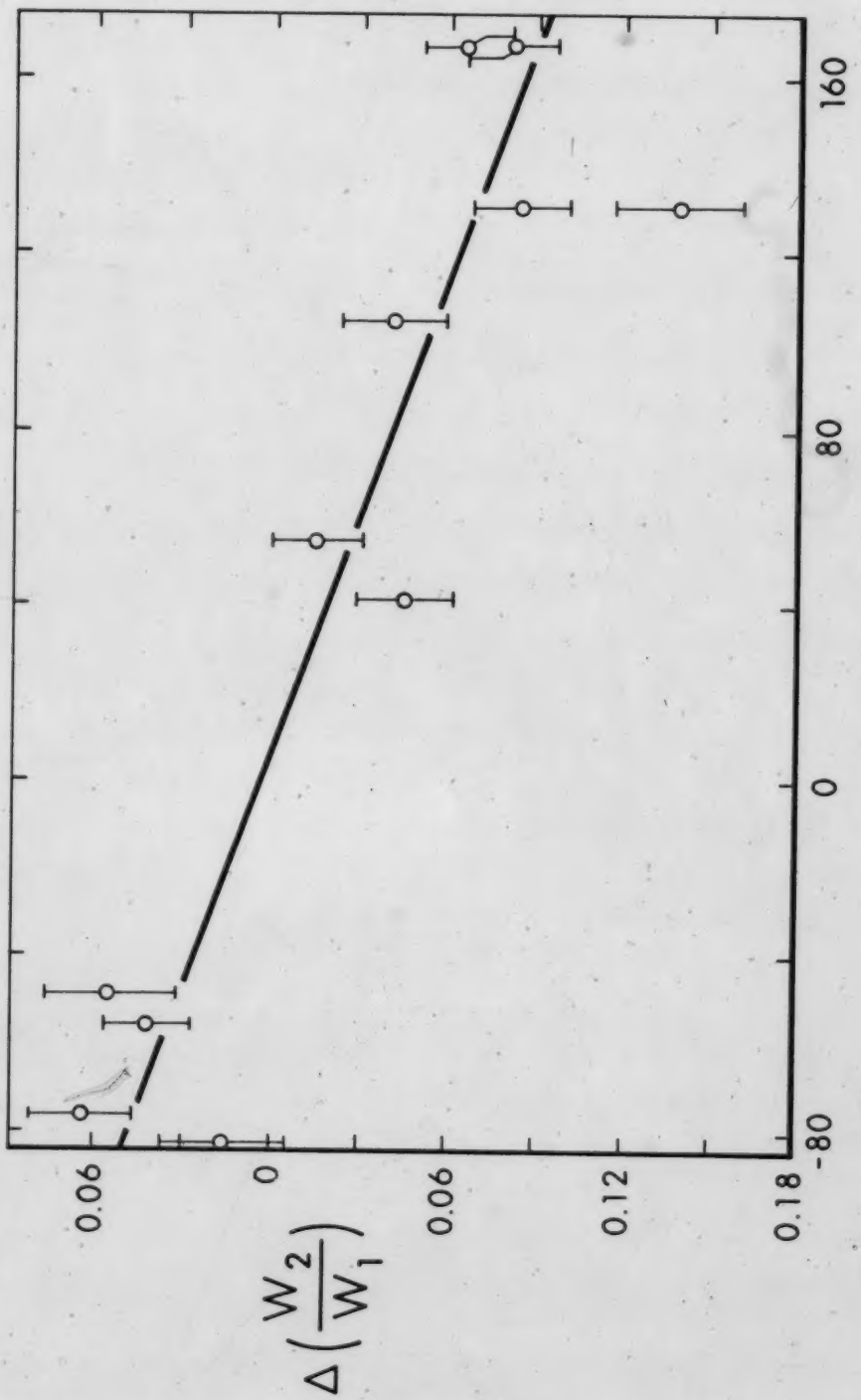
0.06
0
0.06
0.12
0.18
-80
0
80
160
$\Delta\left(\frac{W_2}{W_1}\right)$
$\Delta\nu$ (kHz)

The horizontal axis is the difference between the observing and saturation frequencies used by Reed. (The negative frequencies in Fig. 7.7 are because measurements were made on the $m_{-3/2 \leftrightarrow -1/2}$ satellite rather than on the "high frequency" satellite. From eq. (3.1), it can be seen that near $\theta = 90°$ this resonance has a frequency lower than that of the center line.) In Fig. 7.7 the data points are those of Reed, and the solid line is a linear fit to the data. From this figure it seems that the discrepancy is proportional to the frequency difference.

We shall now describe two possible explanations for the discrepancy in the θ dependence. The first explanation presupposes a systematic shift in the baseline. We assume that in Reed's spectrometer there was a modulation pickup or a radiation problem of the type discussed in section 5.4.3. This would cause a baseline offset at the output of the lock-in detector. We further assume that this baseline was of the form shown in Fig. 7.8, where the effect has been exaggerated for demonstration purposes. If account was not taken of such a baseline offset, then the measured resonance amplitudes near $\theta = 0°$ would be too large and the measured value of E would therefore be too small. Similarly, near $\theta = 90°$, the measured resonance amplitudes would be too small, leading to values of E

Figure 7.8

Explanation of the discrepancy in the W_2/W_1 data in terms of a baseline offset.

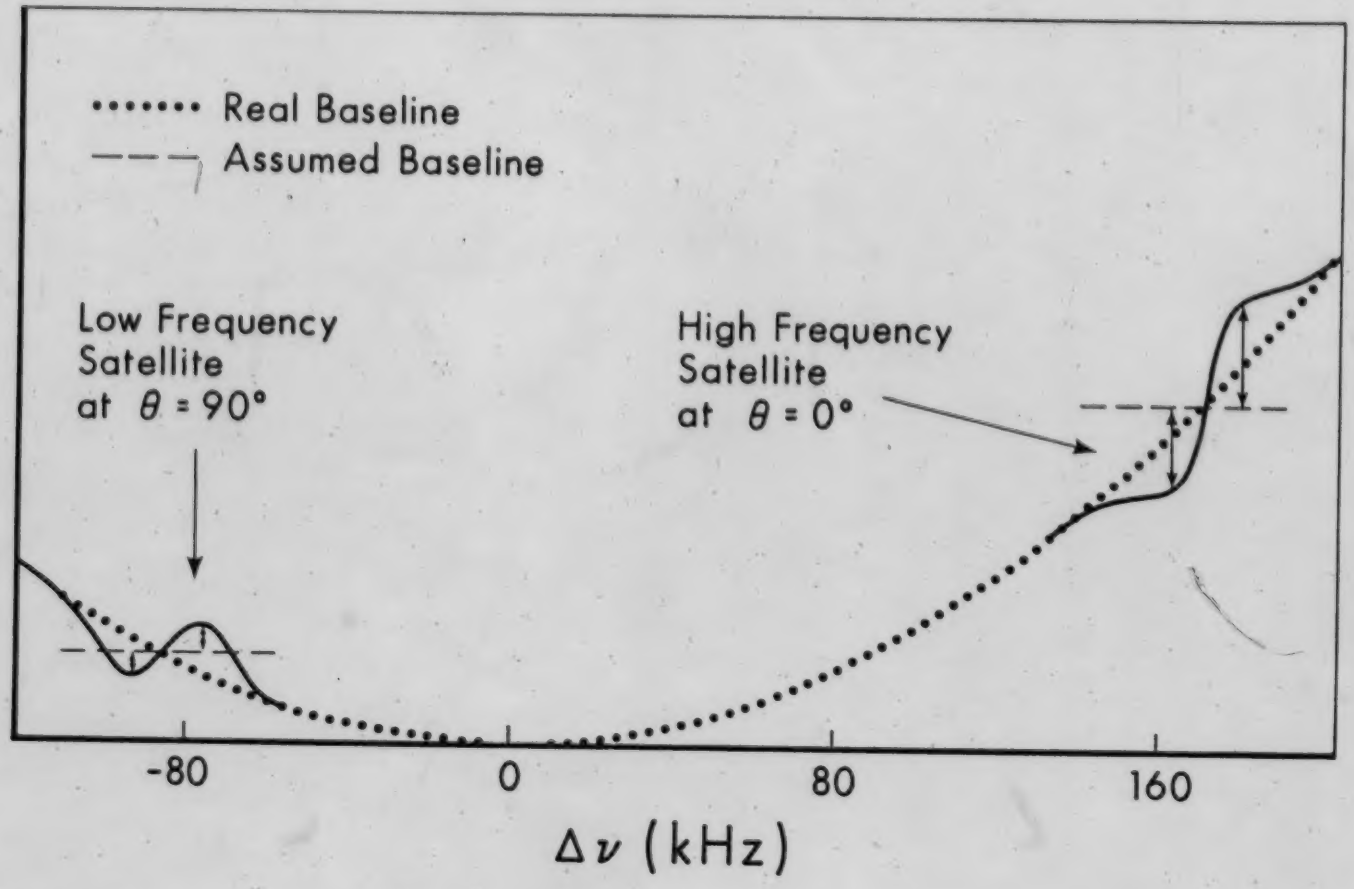
Real Baseline
Assumed Baseline
Low Frequency
Satellite
at θ = 90°
High Frequency
Satellite
at θ = 0°
-80
0
80
160
Δν (kHz)

which were too high. According to this interpretation, it is the difference in the baseline offset between one peak of the absorption derivative and the other peak which causes the error. To explain the linear behaviour shown in Fig. 7.7, we need a baseline offset of the form

$$B = B_o + B_2(\Delta\nu)^2 \qquad (7.7)$$

where B_o is arbitrary and $\Delta\nu$ is the difference between the observing and saturation frequencies. To explain the magnitude of the discrepancy in W_2/W_1 the difference in the baseline on either side of the resonance corresponding to $\Delta\nu$ = 160 kHz, would have been little more than the peak-to-peak noise amplitude in an individual run. Thus, such a problem could easily have been overlooked.

We shall now consider the second explanation for the discrepancy. As mentioned in sections 5.4.3 and 7.1, there was a small frequency dependent systematic error in our system, which we believe to be caused by the frequency dependence of the rejection of the balance network. As can be seen in Fig. 5.4, the orthogonal mode of the balance network contains a delay line. Thus, since a delay line produces a constant time delay, the phase angle of the "orthogonal mode" will vary linearly with frequency. Thus, if the balance network is adjusted to reject the saturation

frequency, it will not be perfectly balanced at other frequencies. Indeed, the magnitude of the net coupling will be proportional to the difference between the saturation frequency and the frequency under consideration. Thus, if the rf power source receives any radiation from the spectrometer, at the observing frequency in particular, it will be coupled back to the spectrometer sample coil via the mechanism just described. Since the magnitude of the effect will be proportional to $\Delta\nu$, this mechanism can account for the linear dependence of the discrepancy displayed in Fig. 7.7. The magnitude of this problem is likely to be more serious in Reed's apparatus than in ours since his spectrometer and rf power source were not effectively shielded.

Although there undoubtedly was a modulation pickup problem in Reed's spectrometer, we feel that the second explanation is more appropriate. One reason is that the second mechanism will result in a direct modulation of the spectrometer observing power, and hence produce a systematic error which is independent of whether ω_m or $2\omega_m$ detection methods are used. Thus, it can explain the agreement between our preliminary results and those of Reed. Secondly, the discrepancy will automatically be zero when $\Delta\nu$ is zero, whereas in the first explanation one has to make a

separate assumption to obtain this feature.

The discrepancy in the θ dependence, just discussed, is responsible for the difference in the values of M_{1313}/M_{1111} and M_{3333}/M_{1111}. However, the gross discrepancy in the value of M_{1123}/M_{1111} stems from the measurements made by Reed near $\phi = 90°$. His data are shown in Fig. 7.9 together with θ dependence obtained from our M'-values. It can be seen that the θ dependence of W_2/W_1 should be almost symmetrical about $\theta = 90°$, whereas Reed's data are very asymmetric. Moreover, the discrepancy between our values and those of Reed does not appear to be proportional to $\Delta\nu$, in contrast to the data shown in Fig. 7.7. Since no other data were taken by Reed after these very anomalous results, one cannot say whether or not a permanent change in the characteristics of the spectrometer had occurred after the θ dependence results. As was made clear in section 5.4.3, apparently insignificant changes in our apparatus did produce large systematic errors. We can only speculate that some change occurred in the equipment between the two sets of data.

7.4 Comparison with 77 K results

Goldburg (1959) performed a double resonance experiment similar to ours except that he measured the enhancement by a pulsed rather than a steady state

Figure 7.9

W_2/W_1 as a function of angle θ for $\phi = 86.5°$. The solid line represents the present study, and the dotted line is a least squares fit of Reed's data to the theoretical form.

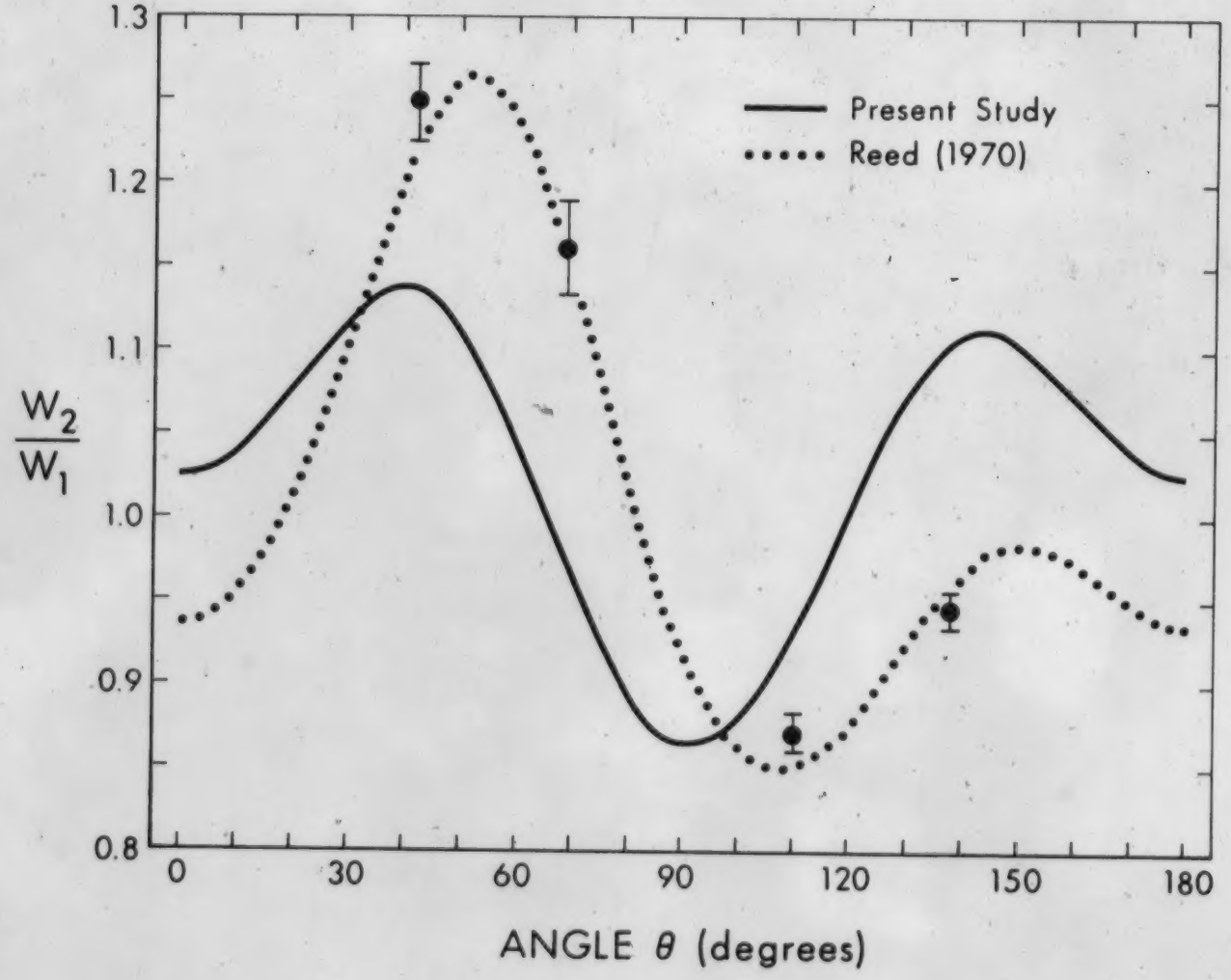
Present Study
Reed (1970)
$\frac{W_2}{W_1}$
1.3
1.2
1.1
1.0
0.9
0.8
0
30
60
90
120
150
180
ANGLE θ (degrees)

technique. He found $W_2/W_1 = 0.90 \pm 0.05$ at $\theta = 0°$ for sodium nitrate at 77 K.

Niemelä (1967) studied the orientation dependence of the ^{23}Na relaxation in sodium nitrate at 77 K by means of the pulsed NMR analog of our transient experiment. He fitted the transient decays to a sum of exponentials from which he was able to extract values of W_1, W_2 and W_3 at various crystal orientations. At $\theta = 0°$, Niemela's value of W_2/W_1 is approximately 1.06, in only fair agreement with Goldburg's result. The following results were derived by Hughes et al (1970) from Niemelä's data:

$$\left.\begin{aligned} M_{1313}/M_{1111} &= 0.78 \pm 0.02 \\ M_{3333}/M_{1111} &= 0.66 \pm 0.04 \\ M_{1113}/M_{1111} &= 0.26 \pm 0.02 \end{aligned}\right\} \qquad (7.8)$$

and

$$e^2Q^2M_{1313} = (1.84 \pm 0.05) \times 10^{-2}\ s^{-1} . \qquad (7.9)$$

It is known that thermal expansion in sodium nitrate occurs mainly along the triad axis (Austin and Pierce, 1933). If we assume that the thermal expansion coefficients obtained from X-ray measurements by Cherin et al (1967) apply down to 77 K, then the angle θ in the point charge model will increase by

approximately 0.5° on cooling from 295 to 77 K. Thus, from Figs. 7.1 and 7.2 we see that M_{1313}/M_{1111} and M_{3333}/M_{1111} should both decrease by approximately 0.03. This agrees well with the observed decrease of 0.02 ± 0.02 and 0.05 ± 0.04 respectively between 295 and 77 K. However, we see that M_{1113}/M_{1111} is more than a factor of two larger at 77 K than at 295 K. (The sign of Niemelä's value of M_{1113}/M_{1111} is not known, since he did not distinguish between ϕ and $\phi + 60°$. We assume, for lack of evidence to the contrary, that M_{1113}/M_{1111} is negative at 77 K.) By comparison of Figs. 7.3 and 7.6 it is clear that the 77 K value of M_{1113}/M_{1111} is in much better agreement with the "linear" model than with the "quadratic" model. This would suggest that the dominant relaxation mechanism is the anharmonic Raman process at this temperature. In section 7.2, we saw that our room temperature results are consistent with the harmonic Raman process. However, according to the theoretical predictions of Van Kranendonk and Walker (1967), both processes should have the same $\sim T^2$ temperature dependence. It thus seems unlikely that the dominant relaxation mechanism would be different at 295 and 77 K. One is thus led to question the validity of the point charge model. It seems reasonable to expect this model to be more appropriate at high rather than low temperatures,

since, at lower temperatures the characteristic wavelength of lattice vibrations is longer. Thus, one would expect more distant neighbours to contribute to the quadrupole relaxation at the lower temperature. On this basis, one is led to conclude that the harmonic Raman process may be the dominant one at both temperatures for ^{23}Na in sodium nitrate. However, this is very tentative and more work is required to confirm this point.

From eqs. (7.9) and (6.12) we find that $e^2Q^2M_{1313}$ has increased by a factor of 26.2 ± 0.8 between 77 and 295 K. According to eq. (2.40), this quantity should have a T^2 dependence and hence change by a factor of 14.7. However, since 77 K is probably less than half the Debye temperature for sodium nitrate, the more rapid variation of $e^2Q^2M_{1313}$ may not be too surprising.

Niemelä (1967) found that the magnetic relaxation probability is given by

$$W_3 = (2.0 \pm 0.6) \times 10^{-4} \ s^{-1} \qquad (7.10)$$

at 77 K in his sample. Our value of the magnetic relaxation is given by (from section 6.4)

$$W_3 = (2.7 \pm 0.9) \times 10^{-4} \ s^{-1} \ . \qquad (7.11)$$

Since magnetic relaxation is caused by paramagnetic impurities is expected to be temperature independent, at

least to first order, it would appear from eqs. (7.10) and (7.11) that our small crystal is of comparable purity to Niemelä's crystal. Since the paramagnetic impurity concentration of both crystals has been estimated to be no more than 1 part in 10^6, the agreement between the W_3 values is reassuring.

The excellent agreement between the values of M_{1313}/M_{1111} and M_{3333}/M_{1111} obtained by us and by Niemelä is also very encouraging, since the experimental methods and temperature were very different in the two cases. Thus, we feel that the large change in M_{1113}/M_{1111} is real and merits further investigation.

CHAPTER VIII

CONCLUSION

From the results and discussions presented in Chapters VI and VII, it is clear that we have developed instrumentation capable of obtaining precise and accurate measurements of NMR amplitude. This has enabled reliable relaxation data to be obtained on the quadrupole split spectrum in sodium nitrate. Since the system is under the control of a real-time minicomputer, very complex control algorithms can be executed. Thus, experiments which would otherwise be impractical can be conceived and performed.

Our steady state method suffers from the disadvantage that it does not give the magnitude of W_1 or W_2. However, much information on quadrupole relaxation can be obtained from the ratio W_2/W_1. We have shown that this quantity can be measured using our experiment and technique to an accuracy of about ±1%.

The transient method has the advantage that it measures the relaxation rates directly and is much less demanding on the instrumentation than the steady state one. It would appear from our preliminary work that it is capable of giving values of relaxation rates which are accurate to about ±1% for the case where there are several closely spaced resonances.

(In this case, the pulse method suffers from the drawback that more than one resonance is excited simultaneously thereby complicating the interpretation of the data.)

We have definitely established that the ^{23}Na spin-lattice quadrupolar relaxation occurs via a multiphonon interaction in sodium nitrate at room temperature. By comparing the results with a point-charge model, it would appear that the spin-lattice relaxation occurs via the harmonic Raman process at room temperature. The evidence at 77 K is that the harmonic Raman process is not dominant. However, this conclusion may be due to the limitations of the model. The theoretical and experimental orientation dependence of W_2/W_1 are in excellent agreement, and no sign of the anomalous behaviour reported by Reed (1970) is found. Furthermore, we conclude that the anomaly was the result of systematic errors of instrumental origin.

We now present some suggestions for further investigation on sodium nitrate. It would be interesting to investigate the temperature dependence of M_{1113}/M_{1111} in view of the large change in this quantity far from any known phase transition. Measurements of W_2/W_1 in the vicinity of the phase transition at 276°C should be useful in studying the detailed mechanism of

the transition. In particular, since "soft vibrational modes" would produce a direct relaxation mechanism, we would expect them to have an effect on the value of W_2/W_1. A double resonance study of ^{14}N in sodium nitrate would be useful in providing further evidence on the relaxation mechanisms occurring in this crystal. Measurements of W_2/W_1 by ultrasonic saturation, in many cases, gives rather unreliable results. Since we have a detailed knowledge of this quantity in sodium nitrate, it would be interesting to perform such an experiment, using our experimental arrangement to try and determine if there are any fundamental differences in the two techniques. It would be useful to extend the W_1 measurements to other crystal orientations to see whether the data can be fitted to the theoretical form. This would check whether there are any unsuspected systematic errors in the W_1 determination. Also, the transient measurement may possibly be extended to the measurement of W_2 by monitoring the transient behaviour of the center line and fitting the decay to a multiexponential time dependence (cf. Niemelä, 1967).

Other sodium salts which would be suitable for a double resonance study are sodium nitrite, sodium chlorate and sodium bromate, for example. Sodium nitrite is particularly appealing since it has several phase transitions. Furthermore, since the sodium sites

in this crystal do not possess inversion symmetry, this material should provide a test of time reversal symmetry (Hughes, 1973).

The work described in this thesis was carried out on single crystals. However, there are many sodium salts which are difficult, if not impossible, to obtain as a large single crystal. However, if the asymmetry parameter is zero and the quadrupole coupling constant is sufficiently small (probably $\lesssim$500 kHz), a peak in the NMR powder pattern may be visible, corresponding to the satellites for which θ is near 90° (Cohen and Reif, 1957). While this peak will be weak, it may be possible to extract meaningful values of W_2/W_1 and W_1 separately for $\theta = 90°$ by the steady-state method and the transient method described in this thesis. An obvious sample with which to test the method is sodium nitrate, since the quadrupole relaxation probabilities are already known.

REFERENCES

Abragam, A., 1961, The Principles of Nuclear Magnetism (Oxford: Clarendon Press).

Abragam, A. and Proctor, W.G., 1958, Phys. Rev., 109,1441.

Andrew, E.R., Eades, R.G., Hennel, J.W. and Hughes, D.G., 1962, Proc. Phys. Soc., 79, 954.

Andrew, E.R. and Swanson, K.M., 1960, Proc. Phys. Soc., 75, 582.

Austin, J.B. and Pierce, R.H.H., 1933, J. Amer. Chem. Soc., 55, 661.

Bersohn, R., 1952, J. Chem. Phys., 20, 1505.

Betsuyaku, H., 1969, J. Phys. Soc. Japan, 27, 1485.

Bevington, P.R., 1969, Data Reduction and Error Analysis for the Physical Sciences (McGraw-Hill: New York) p. 116.

Bloch, F., 1958, Phys. Rev., 111, 841.

Bloch, F., Hansen, W.W. and Packard, M.E., 1946, Phys. Rev., 70, 474.

Bloembergen, N., 1949, Physica, 15, 386.

Bloembergen, N., Purcell, E.M. and Pound, R.V., 1948, Phys. Rev., 73, 679.

Bloembergen, N., Shapiro, S., Pershan, P.S. and Artman, J.O., 1959, Phys. Rev., 114, 445.

Boyd, W.R., 1975, Internal Report, University of Alberta.

Buerger, M.J., 1963, Elementary Crystallography (New York: Wiley) p. 189.

Carlson, A.B., Communication Systems (New York: McGraw-Hill, Inc.) p. 296.

Cherin, P., Hamilton, W.C. and Post, B., 1967, Acta Crystallogr., 23, 455.

Cohen, M.H. and Rief, F., 1957, Solid State Physics, Vol. 5, eds. F. Seitz and D. Turnbull (New York: Academic Press) p. 321.

Cohn, C.E., 1964, Rev. Sci. Instrum., 35, 701.

D'Alessio, G.J. and Scott, T.A., 1971, J. Mag. Res., 5, 416.

Das, T.P. and Hahn, E.L., 1958, Solid State Physics, Suppl. 1, eds. F. Seitz and D. Turnbull (New York: Academic Press).

Goldberger, M.L. and Watson, K.M., 1964, Collision Theory, (New York: Wiley) p. 51.

Goldburg, W.I., 1959, Bull. Amer. Phys. Soc., [II], 4, 251.

Goldburg, W.I., 1959, Phys. Rev., 115, 48.

Goldburg, W.I., 1960, Phys. Rev., 122, 831.

Hahn, E.L., 1950, Phys. Rev., 80, 580.

Haworth, O. and Richards, R.E., 1966, Progress in NMR Spectroscopy, 1, 1.

Howling, D.H., 1966, Rev. Sci. Instrum., 37, 891.

Hughes, D.G., 1966, Proc. Phys. Soc., 87, 953.

Hughes, D.G., 1973, J. Phys. C, 6, 3797.

Hughes, D.G. and Reed, K., 1970, Rev. Sci. Instrum., 41, 293.

Hughes, D.G. and Reed, K., 1971, J. Phys. C, 4, 2945.

Hughes, D.G., Reed, K. and Snyder, R.E., Can. J. Phys., 48, 2212.

Hughes, D.G. and Smith, M.R., 1971, J. Phys. E, 4, 13.

Hughes, D.G., Smith, M.R. and Spencer, P.A., 1973, J. Phys. E, 6, 147.

Hughes, D.G., Smith, M.R. and Spencer, P.A., 1973, Proc. IEEE, 61, 239.

Jeener, J., 1968, Advances in Magnetic Resonance, Vol.3, ed. J.S. Waugh (New York: Academic Press) p. 206.

Kambe, K. and Ollom, J.F., 1956, J. Phys. Soc. Japan, 11, 50.

Kornfel'd, M.I. and Lemanov, V.V., 1960, J. eksp. teor. Fiz., 39, 53 (1961, Sov. Phys.-JETP, 12, 38).

Mariani, E., Eckstein, J. and Rubínová, E., 1967, Czech. J. Phys., B 17, 552.

Niemelä, L., 1967, Ann. Acad. Sci. Fennicae, A VI, No. 236.

Nye, J.F., 1957, Physical Properties of Crystals (London: Oxford U.P.) p. 9.

Paul, G.L. and Pryor, A.W., 1971, Acta Cryst., B 27, 2700.

Pietilä, A., 1968, Ann. Acad. Sci. Fennicae, A VI, No. 271.

Pietilä, A., 1974, J. Phys. C, 7, 211.

Pound, R.V., 1950, Phys. Rev., 79, 685.

Proyotorov, B.N., 1961, J. eksp. teor. Fiz., 41, 1582 (1961, Sov. Phys.-JETP, 14, 1126).

Redfield, A.G., 1955, Phys. Rev., 98, 1787.

Reed, K., 1970, Ph. D. Thesis, University of Alberta.

Robinson, F.N.H., 1959, J. Sci. Instr., 36, 481.

Rollin, B.V., 1946, Nature, Lond. 158, 669.

Sarnatskii, V.M. and Shutilov, V.A., 1972, Fizika Tverdogo Tela, 14, 771 (1972, Sov. Phys.- Sólid State , 14, 649).

Sarles, L.R. and Cotts, R.M., 1958, Phys. Rev., 111, 853.

Satoh, M., 1965, J. Phys. Soc. Japan, 20, 1008.

Slichter, C.P., 1963, Principles of Magnetic Resonance, (New York: Harper and Row).

Smith, M.R. and Cohn-Sfetcu, S., 1974, Nucl. Instr. Meth., 114, 171.

Smith, M.R. and Hughes, D.G., 1971, J. Phys. E, 4, 725.

Snyder, R.E. and Hughes, D.G., 1971, J. Phys. C, 4, 227.

Sternheimer, R., 1950, Phys. Rev., 80, 102.

Van Kranendonk, J., 1954, Physica, 20, 781.

Van Kranendonk, J. and Walker, M., 1967, Phys. Rev. Lett., 18, 701.

Van Kranendonk, J. and Walker, M., 1968, Can. J. Phys., 46, 2241.

Van Vleck, J.H., 1948, Phys. Rev., 74, 1168.

Volkoff, G.M., 1953, Can. J. Phys., 31, 820.

Watkins, G.D. and Pound, R.V., 1951, Phys. Rev., 82, 343.

Wilson, G.V.H., 1963, J. Appl. Phys., 34, 3276.

Yosida, K. and Moriya, T., 1956, J. Phys. Soc. Japan, 11, 33.

Appendix I

General orientation dependence of W_1 and W_2

We give the general orientation dependence of the quadrupole relaxation probabilities W_1 and W_2, for the case of a real quadrupole relaxation tensor (Snyder and Hughes, 1971).

$$
\begin{aligned}
W_1 = (e^2Q^2/64I)\,[&4M_{1111}+4M_{1133}+M_{3333}+4M_{2323}+4M_{3131}+4M_{1212} \\
&+6(3M_{3333}-2M_{2323}-2M_{3131})\cos^2\theta \\
&-(4M_{1111}+4M_{1133}+19M_{3333}-16M_{2323}-16M_{3131}+4M_{1212})\cos^4\theta \\
&+24(M_{3331}\cos\phi+M_{3323}\sin\phi)\sin\theta\cos\theta(1-2\cos^2\theta) \\
&+8\{(2M_{1131}+M_{3331}+2M_{2312})\cos\phi-(2M_{1123}+M_{3323}-2M_{3112}) \\
&\times \sin\phi\}\sin\theta\cos^3\theta \\
&-12\{(2M_{1133}+M_{3333})\cos 2\phi+2M_{3312}\sin 2\phi\}\sin^2\theta\cos^2\theta \\
&-4\{(M_{2323}-M_{3131})\cos 2\phi-2M_{2331}\sin 2\phi\}\sin^2\theta(1-4\cos^2\theta) \\
&-8\{(2M_{1131}+M_{3331}-2M_{2312})\cos 3\phi+(2M_{1123}+M_{3323}+2M_{3112}) \\
&\times \sin 3\phi\}\sin^3\theta\cos\theta \\
&-\{(4M_{1111}+4M_{1133}+M_{3333}-4M_{1212})\cos 4\phi+4(2M_{1112}+M_{3312}) \\
&\times \sin 4\phi\}\sin^4\theta]
\end{aligned}
\qquad \text{(A1.1)}
$$

$$W_2 = (e^2Q^2/256I)[4M_{1111}+4M_{1133}+19M_{3333}+16M_{2323}+16M_{3131}$$

$$+4M_{1212}+6(4M_{1111}+4M_{1133}-5M_{3333}+4M_{1212})\cos^2\theta$$

$$+(4M_{1111}+4M_{1133}+19M_{3333}-16M_{2323}-16M_{3131}+4M_{1212})$$

$$\times \cos^4\theta-48(M_{3331}\cos\phi+ M_{3323}\sin\phi)\sin^3\theta\ \cos\theta$$

$$-8\{(2M_{1131}+M_{3331}+2M_{2312})\cos\phi-(2M_{1123}+M_{3323}-2M_{3112})$$

$$\times \sin\phi\}\sin\theta\cos\theta(3+\cos^2\theta)$$

$$+12\{(2M_{1133}+M_{3333})\cos 2\phi+ 2M_{3312}\sin 2\phi\}\sin^2\theta(1+\cos^2\theta)$$

$$+16\{(M_{2323}-M_{3131})\cos 2\phi- 2M_{2331}\sin 2\phi\}\sin^4\theta$$

$$+8\{(2M_{1131}+M_{3331}-2M_{2312})\cos 3\phi+ (2M_{1123}+M_{3323}+2M_{3112})$$

$$\times \sin 3\phi\}\sin^3\theta\cos\theta$$

$$+\{(4M_{1111}+4M_{1133}+M_{3333}-4M_{1212})\cos 4\phi$$

$$+4(2M_{1112}+M_{3312})\sin 4\phi\}\sin 4\theta] \quad . \qquad \text{(A1.2)}$$

Appendix II

Calculation of $M_{\alpha\beta\alpha'\beta'}$ for sodium nitrate using a point charge model.

We shall describe a simple nearest-neighbour point-charge model used by Hughes and Reed (1971) to calculate the M-tensor components in sodium nitrate. The sodium nuclei are assumed to vibrate in the electrostatic field of the nearest neighbour oxygen atoms, which are treated as stationary point charges. The configuration of these six charges is shown in Fig. A2.1.

The change in the electric field gradient $V_{\alpha\beta}$ at the nuclear site caused by a displacement $d\underline{r}$ can be expressed by the following power series

$$V_{\alpha\beta} = \sum_j \frac{\partial V_{\alpha\beta}}{\partial x_j} dx_j + \frac{1}{2} \sum_{j,k} \frac{\partial^2 V_{\alpha\beta}}{\partial x_j \partial x_k} dx_j dx_k \ \ldots \qquad \text{(A2.1)}$$

The linear term in eq. (A2.1) will give rise to spin-lattice relaxation via the direct process and the anharmonic Raman process (Van Kranendonk and Walker, 1967, 1968), whereas the quadratic term will give rise to the harmonic Raman process (Van Kranendonk, 1954).

The M-tensor components $M_{\alpha\beta\alpha'\beta'}$ are governed by the product of the fluctuations in $V_{\alpha\beta}$ and $V_{\alpha'\beta'}$. Thus, for a "linear" process. we obtain

Figure A2.1

Schematic representation of the charge configuration used in the point charge model for the calculation of $M_{\alpha\beta\alpha'\beta'}$.

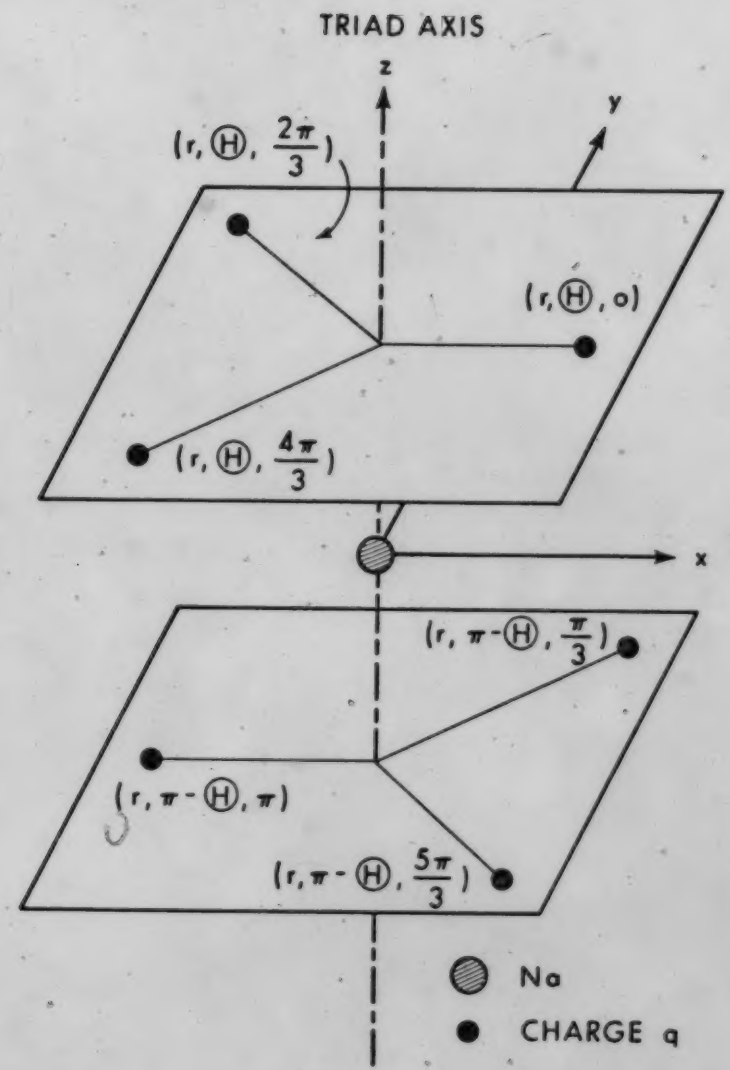
TRIAD AXIS
z
y
x
$(r, \Theta, \frac{2\pi}{3})$
(r, Θ, o)
$(r, \Theta, \frac{4\pi}{3})$
$(r, \pi-\Theta, \frac{\pi}{3})$
$(r, \pi-\Theta, \pi)$
$(r, \pi-\Theta, \frac{5\pi}{3})$
Na
CHARGE q

$$(M_{\alpha\beta\alpha'\beta'})_{lin} \propto \overline{\left(\sum_j \frac{\partial V_{\alpha\beta}}{\partial x_j}\, dx_j\right)\left(\sum_j \frac{\partial V_{\alpha'\beta'}}{\partial x_j}\, dx_j\right)}$$

$$= \overline{\sum_{j,k} \frac{\partial V_{\alpha\beta}}{\partial x_j} \frac{\partial V_{\alpha'\beta'}}{\partial x_k}\, dx_j dx_k} \qquad \text{(A2.2)}$$

where the bar signifies an average over the nuclear vibration. If we assume that there is no preferred direction for the nuclear motion, then

$$\overline{dx_j dx_k} = \delta_{ik}\, (dr)^2/3 \ . \qquad \text{(A2.3)}$$

Substituting into eq. (A2.2) we thus obtain

$$(M_{\alpha\beta\alpha'\beta'})_{lin} \propto \frac{(dr)^2}{3} \sum_j \frac{\partial V_{\alpha\beta}}{\partial x_j} \frac{\partial V_{\alpha'\beta'}}{\partial x_j} \ . \qquad \text{(A2.4)}$$

The model can be generalized to take into account anisotropy in the nuclear motion. Let k be the amplitude of the vibration along the z axis divided by the amplitude in the x-y plane. We further assume that the vibration in the x-y plane is isotropic and of amplitude dr. Then eq. (A2.3) will become

$$\overline{dx_j dx_k} = \delta_{jk}\{(k^2-1)\delta_{j3} + 1\}\frac{(dr)^2}{3} \ . \qquad \text{(A2.5)}$$

For a "quadratic" process, we obtain from eq. (A2.1)

$$(M_{\alpha\beta\alpha'\beta'})_{quad} \propto \frac{1}{4}\Bigg\{\sum_j \frac{\partial^2 V_{\alpha\beta}}{\partial x_j^2}\frac{\partial^2 V_{\alpha'\beta'}}{\partial x_j^2}\overline{(dx_j)^4}$$

$$+ \sum_{\substack{j,k \\ j\neq k}}\left(\frac{\partial^2 V_{\alpha\beta}}{\partial x_j^2}\frac{\partial^2 V_{\alpha'\beta'}}{\partial x_k^2} + 2\,\frac{\partial^2 V_{\alpha\beta}}{\partial x_j \partial x_k}\frac{\partial^2 V_{\alpha'\beta'}}{\partial x_j \partial x_k}\right)\cdot$$

$$\cdot\overline{(dx_j)^2(dx_k)^2}\Bigg\} \qquad (A2.6)$$

for the case of the nuclear site possessing inversion symmetry. For the anisotropic nuclear motion we obtain

$$\overline{(dx_j)^4} = \{(k^4-1)\delta_{j3}+1\}\frac{(dr)^4}{5} \qquad (A2.7)$$

and

$$\overline{(dx_j)^2(dx_k)^2} = \{(k^2-1)\delta_{j3}\delta_{k3}+1\}\frac{(dr)^4}{15}\ ;\ j\neq k\ . \qquad (A2.8)$$

After a lengthy calculation, which takes into account the configuration of the six charges shown in Fig. A2.1, it can be shown (Reed, 1970) that for the "linear" process:

$$M_{1111} = 6q^2u^2r^{-8}\big(\sin^2\theta[(3-5\sin^2\theta)^2+(1/2)(3-5\sin^2\theta/4)^2$$
$$+(3/2)(-1+5\sin^2\theta/4)]+k^2\cos^2\theta[(5\sin^2\theta-1)^2$$
$$+2(-1+5\sin^2\theta/4)^2]\big) \qquad (A2.9)$$

$$M_{1313} = 6q^2u^2r^{-8}\left(\cos^2\theta[(1-5\sin^2\theta)^2 + (75/8)\sin^4\theta]\right.$$
$$\left. + (3/2)+k^2\sin^2\theta(1-5\cos^2\theta)^2\right) \qquad \text{(A2.10)}$$

$$M_{3333} = 18q^2u^2r^{-8}\left((5\cos^2\theta-1)^2(1-\cos^2\theta)\right.$$
$$\left. + k^2(3-5)\cos^2\theta)^2\cos^2\theta\right) \qquad \text{(A2.11)}$$

$$M_{1113} = 6q^2u^2r^{-8}\sin\theta\cos\theta\cos3\phi_o\left((3-5\sin^2\theta)(1-5\sin^2\theta)\right.$$
$$+ (15/4)\sin^2\theta(1-5\sin^2\theta/4)-(3-5\sin^2\theta/4)$$
$$\left.\times (1-5\sin^2\theta/4)-(15k^2/4)(1-5\cos^2\theta)\sin^2\theta\right). \qquad \text{(A2.12)}$$

Similarly, one finds for the "quadratic" process;

$$M_{1111} = (3q^2u^4r^{-10}/10)\left[3(3-30\sin^2\theta+35\sin^4\theta)^2\right.$$
$$+ 3(1-5\sin^2\theta)^2+2(3-30\sin^2\theta+35\sin^4\theta)(1-5\sin^2\theta)$$
$$+ 6[3-(30/4)\sin^2\theta+(35/16)\sin^4\theta]^2+6[1-5\sin^2\theta$$
$$+ (105/15)\sin^4\theta]^2+(300/8)\sin^4\theta(3-7\sin^2\theta/4)^2$$
$$+ 4[3-(30/4)\sin^2\theta+(35/16)\sin^4\theta][1-5\sin^2\theta$$
$$+(105/16)\sin^4\theta]+k^2[100\cos^2\theta\sin^2\theta(7\sin^2\theta/3)^2]$$
$$- 2(4-35\sin^2\theta\cos^2\theta)^2+50\sin^2\theta\cos^2\theta[(3-7\sin^2\theta/4)^2$$
$$+ 3(1-7\sin^2\theta/4)^2]+k^4[(4-35\sin^2\theta\cos^2\theta)^2]$$
$$\left.+ 2[(15/4)\sin^2\theta-4+ (35/4)\sin^2\theta\cos^2\theta]^2\right] \quad , \qquad \text{(A2.13)}$$

$$M_{1313} = (3q^2u^4r^{-10}/10)\Big[(\sin^2\theta\cos^2\theta[75(7\sin^2\theta-3)^2$$

$$- 50(7\sin^2\theta-3)+75(75/2)(3-7\sin^2\theta/4)$$

$$+ (75/2)(1-21\sin^2\theta/4)+150(1-7\sin^2\theta/4)^2$$

$$+ (50/2)(3-7\sin^2\theta/4)(1-21\sin^2\theta/4)]$$

$$+ k^2[4(35\sin^2\theta\cos^2\theta-4)^2-50\sin^2\theta\cos^2\theta(3-7\cos^2\theta)^2$$

$$+ 2(35\sin^2\theta\cos^2\theta+15\sin^2\theta-16)^2+(75/2)\sin^4\theta$$

$$(7\cos^2\theta-1)^2-(50/2)\sin^2\theta\cos^2\theta(3-7\cos^2\theta)^2]$$

$$+ k^4(225/2)\sin^2\theta\cos^2\theta(7\cos^2\theta-3)^2)\Big] \qquad \text{(A2.14)}$$

$$M_{3333} = (9q^2u^4r^{-10}/10)\big[[8(1-5\cos^2\theta)^2+40(1-5\cos^2\theta)$$

$$\times (7\cos^2\theta-1)\sin^2\theta+75(7\cos^2\theta-1)^2\sin^4\theta]$$

$$+ k^2[(2)(3-30\cos^2\theta+35\cos^4\theta)][2(1-5\cos^2\theta)$$

$$+ 5\sin^2\theta(7\cos^2\theta-1)]+100\cos^2\theta\sin^2\theta(7\cos^2\theta-3)^2$$

$$+ k^4[3-30\cos^2\theta+35\cos^4\theta]^2\big) \; . \qquad \text{(A2.15)}$$

$$M_{1113} = (3q^2u^4\sin\theta\cos\theta\cos3\phi_o r^{-10}/2)\Big[3(7\sin^2\theta-3)$$

$$\times (3-30\sin^2\theta+35\sin^4\theta)-3(5\cos^2\theta-4)$$

$$- (3-30\sin^2\theta+35\sin^4\theta)+(7\sin^2\theta-3)(5\cos^2\theta-4)$$

$$- 3(3-7\sin^2\theta/4)[3-(30/4)\sin^2\theta+(35/16)\sin^4\theta]$$

$$- 3(-1+21\sin^2\theta/4)[5\cos^2\theta-4+(105/16)\sin^4\theta]$$

$$+ k^2[(35\sin^2\theta\cos^2\theta-4)(42\sin^2\theta-20)-16(7\sin^2\theta-12)$$

$$\times (15\sin^2\theta-16+35\sin^2\theta\cos^2\theta)-60\sin^2\theta(7\cos^2\theta-1)$$

$$\times (7\sin^2\theta-1)(7\sin^2\theta-4)-8(3-7\cos^2\theta)$$

$$\times (15\sin^2\theta-16+35\sin^2\theta\cos^2\theta)]$$

$$+ k^4[12(7\cos^2\theta-3)(105\sin^2\theta\cos^2\theta-15\sin^2\theta)]\Big). \quad \text{(A2.16)}$$

In the coordinate system and for this model M_{1123} is zero.

Since the $M_{\alpha\beta\alpha'\beta'}$ are proportional to r^{-8} for the "linear" process and to r^{-10} for the "quadratic" process, the nearest-neighbour approximation is likely to be reasonable for the case of ^{23}Na in sodium nitrate. Also, although the details of the phonon spectrum have been ignored, the model should be a reasonable approximation at temperatures greater than the Debye temperature. The point-charge model is a gross simplification of the actual situation in a real crystal. Moreover, factors such as antishielding (Sternheimer, 1950) and covalency in the crystal bonding (Yosida and Moriya, 1956) have been ignored. This will result in the magnitude of an individual M component being completely unreliable. However, the ratio of two M

components should be fairly accurate, since it is expected that several factors which have been ignored will affect all the M's equally.

Appendix III

Selection of P_{obs} values and the optimum utilization of time in the measurement of NMR enhancement

In our experiment, the NMR enhancement E is measured at various observing powers P_{obs}, and the value of W_2/W_1 is determined from the intercept on the E axis of the straight line which is the best fit to the E-P_{obs} data. The enhancement values are subject to random error because of the noise generated in the spectrometer. However, for a Robinson spectrometer, this noise is independent of rf level (Howling, 1966; Smith and Hughes, 1971). At the low spectrometer powers used in our work, the NMR saturation is negligible and the signal amplitudes are therefore proportional to the rf level $\sqrt{P_{obs}}$. Since E is only a weak function of $\sqrt{P_{obs}}$ (it only varies by 5% over the complete range of P_{obs} used), it follows that the random error in the i'th data point E_i, is inversely proportional to $\sqrt{(P_{obs})_i}$. Also, the error in E_i is inversely proportional to $\sqrt{t_i}$, where t_i is the time spent on the i'th data point. On this basis, we wish to find the values of $(P_{obs})_i$ and t_i which minimize the random error in the intercept subject to the constraint

$$\sum_{i=1}^{n} t_i = T \qquad \text{(A3.1)}$$

where T is the total time available. Since many hours are required to obtain a precision of 0.1% in an enhancement measurement at even a large value of P_{obs}, it is important to acquire data as efficiently as possible.

If we now call $(P_{obs})_i$ and E_i, x_i and y_i respectively, then the data are fitted to

$$y = a + bx \tag{A3.2}$$

where x is necessarily positive. The square of the standard error in the intercept a is given by (Bevington, 1969)

$$\sigma_a^2 = \sum x_i^2/\sigma_i^2 / \{ (\sum 1/\sigma_i^2)(\sum x_i^2/\sigma_i^2) - (\sum x_i/\sigma_i^2)^2 \} \tag{A3.3}$$

where σ_i is the standard error in y_i and the summations extend over all n data points. It follows from the discussion in the previous paragraph that

$$1/\sigma_i^2 = cx_i t_i \tag{A3.4}$$

where c is a constant. If we regard the x_i as arbitrary, then the optimum t_i must satisfy the relation

$$d(\sigma_a^2) = \sum (\partial\sigma_a^2/\partial t_i) dt_i = 0 \tag{A3.5}$$

subject to the constraint

$$\sum dt_i = 0 \ . \tag{A3.6}$$

A solution to eqs. (A3.5) and (A3.6) is

$$\partial\sigma_a^2/\partial t_j = \text{a constant independent of } j \ . \qquad \text{(A3.7)}$$

Substituting eq. (A3.4) into eq. (A3.3) we find

$$\frac{\partial\sigma_a^2}{\partial t_j} = - \frac{x_j(\sum x_i^3 t_i - x_j \sum x_i^2 t_i)^2}{c\left(\sum x_i t_i \sum x_i^3 t_i - (\sum x_i^2 t_i)^2\right)^2} \ . \qquad \text{(A3.8)}$$

Since the denominator in eq. (A3.8) is independent of j, it follows from eq. (A3.7) that

$$x_j(\sum x_i^3 t_i - x_j \sum x_i^2 t_i)^2 = \text{a constant independent of } j. \qquad \text{(A3.9)}$$

Since eq. (A3.9) is a cubic equation in x_j, there are at most three independent x values which satisfy eq. (A3.9). Expanding eq. (A3.9) for n = 3, we find that one of these equations is a linear combination of the other two. We therefore conclude that the optimum number of data points is two.

We now consider the specific case where the two data points are at

$$\left.\begin{aligned} x_1 &= x \\ x_2 &= \alpha x \qquad \text{with } 0 < \alpha < 1 \end{aligned}\right\} \qquad \text{(A3.10)}$$

and the corresponding measurement times are

$$\left.\begin{aligned} t_1 &= \beta T \\ t_2 &= (1-\beta)T \quad \text{with } 0 < \beta < 1 \end{aligned}\right\} \qquad \text{(A3.11)}$$

Substituting into eq. (A3.9) we find that

$$\beta = (1 + \alpha^{-3/2})^{-1} \quad . \tag{A3.12}$$

This gives the optimum allocation of measurement time for an arbitrary value of α. To find the optimum value of α we substitute eqs. (A3.10), (A3.11) and (A3.12) into (A3.3) to obtain

$$\sigma_a^2 = \frac{1}{xcT} \frac{(1 + \alpha^{3/2})^2}{\alpha(1-\alpha)^2} \quad . \tag{A3.13}$$

By differentiating eq. (A3.13) we find that the optimum value of α which minimizes σ_a^2 is 1/4. From eq. (A3.12) one finds that the corresponding value of β is 1/9.

Thus, we conclude that the optimum method of data acquisition consists of taking just <u>two</u> data points differing by a factor of four in P_{obs}, and spending eight ninths of the time at the lower data point.